A Virtual Testing Strategy to Determine Macroscopic Properties of Elasto-Plastic Heterogeneous Composite Materials

Mahshid Ranjbar

Swansea University
Prifysgol Abertawe

College of Engineering

Swansea University

2020

Submitted to Swansea University in fulfilment of the requirements for the Degree of Doctor of Engineering.

Declarations

1. This work has not previously been accepted in substance for any degree and is not being concurrently submitted in candidature for any degree.

   Signed . . . . . [redacted] . . . . . .(candidate)

   Date .....31/01/2020.....

2. This work is the result of my own work and investigation, except where otherwise stated. Other sources have been acknowledged by giving explicit references. A bibliography is appended.

   Signed . . . . . [redacted] . . . . . .(candidate)

   Date .....31/01/2020.....

3. I hereby give consent for my thesis, if accepted, to be available for photo-copying and for inter-library loan, and for the title and summary to be made available to outside organisations.

   Signed . . . . . [redacted] . . . . . .(candidate)

   Date .....31/01/2020.....

Acknowledgements

I would like to express my gratitude to both of my supervisors, Prof. D. Perić, and Prof. W. Dettmer for the help and guidance I received throughout this project. Without the valuable discussions this work would not have been possible.

I would like to express my deepest gratitude for the constant support, understanding and love that I received from my parents during the past years. I am deeply and forever indebted to them for their encouragement throughout my entire life.

This work is lovingly dedicated to my mother Mahtab and my grandmother Pari Dehghanshoar.

Summary

The objective of this work is to determine an effective yield criteria for porous pressure sensitive solids and investigate the anisotropic yield behavior by employing a virtual testing strategy. The work is concerned with the pressure sensitivity typically displayed by geometarials, such as sandstone and composite materials consisting of a series of parallel layers, such as sedimentary rock and underground salt.

Virtual testing strategy is based on computational homogenization approach for the definition of the elasto-plastic transition. Representative volume elements (RVEs) containing single-centered and distributed ellipsoidal voids are analyzed using three-dimensional finite element models under both small and finite strains. Yield curves are obtained following a unified variational formulation, which provides bounds on the effective material properties for a given choice of the Representative Volume Element (RVE).

In order to estimate the effective properties of porous solid, the constitutive behavior of the continuum matrix is assumed to follow the standard Drucker-Prager elasto-plastic model. The computationally generated effective yield criteria are compared against the recently proposed analytical estimates for Drucker-Prager type solids and the SR4 constitutive model for soft rocks. The developed computational approach is applied to estimate the effective properties of a realistic rock sample. To illustrate a wide range of potential engineering applications, the computationally effective yield surface are also obtained under the explicit finite element method.

Finally, based on the simulated yield stress point of composite materials, the parameters for proposed analytical models are acquired with ellipse fit by Taubin's method.

Table of Contents

List of Figures

List of Algorithms

Chapter 1

Introduction

Nowadays many materials have heterogeneous structures and they, are composed of an underlying structure that can be observed at some scale. However, they might have different constitutive behavior which can be ignored due to the size scale of the heterogeneity being insignificant. Materials such as composites, woods, polycrystals, bone or teeth consist of two or more distinct constituents that can have significantly different chemical or physical material properties. The physics and the mechanics of the micro-mechanical properties have a significant impact on the behavior of the macroscopic material. For instance, the overall response of the macroscopic continuum depends strongly on the size, shape, spatial distribution and properties of the microstructural constituents and the interaction between them. The macroscopic response of the heterogeneous material based on both the geometry and properties is predicted by volume averaging of the microstructure behavior. This is known as *homogenization*. Multi-scale modeling is used to predict the behavior of multi-axial properties, such as unidirectional composites. Such behavior is difficult to model experimentally. According to a great number of experimental investigations, the heterogeneous material have complex mechanical behaviors (such as fiber and volume fractions, micro-crack-related damage, plastic deformation and fiber arrangements) which makes them expensive to determine experimentally. Therefore, using micro-scale model allows virtual testing performance to simulate these models, once all the constituents properties are known. This advantage of micromechanics reduces the cost of an experimental work dramatically. There are several methods to evaluate the constituents properties of the

heterogeneous materials, by using experimental campaign which can be expensive and difficult, by using back engineering the properties through a reduced experimental work. In order to validate the results from the latter option, the comparison between the experimental data is necessary due to the uncertainties on the real microstructure. In micromechanics due to their mechanical complexity, *localization* is crucial, as it is evaluating the local stress and strain fields in the phases for a given macroscopic strain. The constituents in heterogeneous materials are statistically distributed. Therefore, the micromechanics methods are based on the *repesentetive volume element* (RVE) with sufficient size to cover all geometrical information and to predict the suitable homogenized behavior (refer to Figure 1.1).

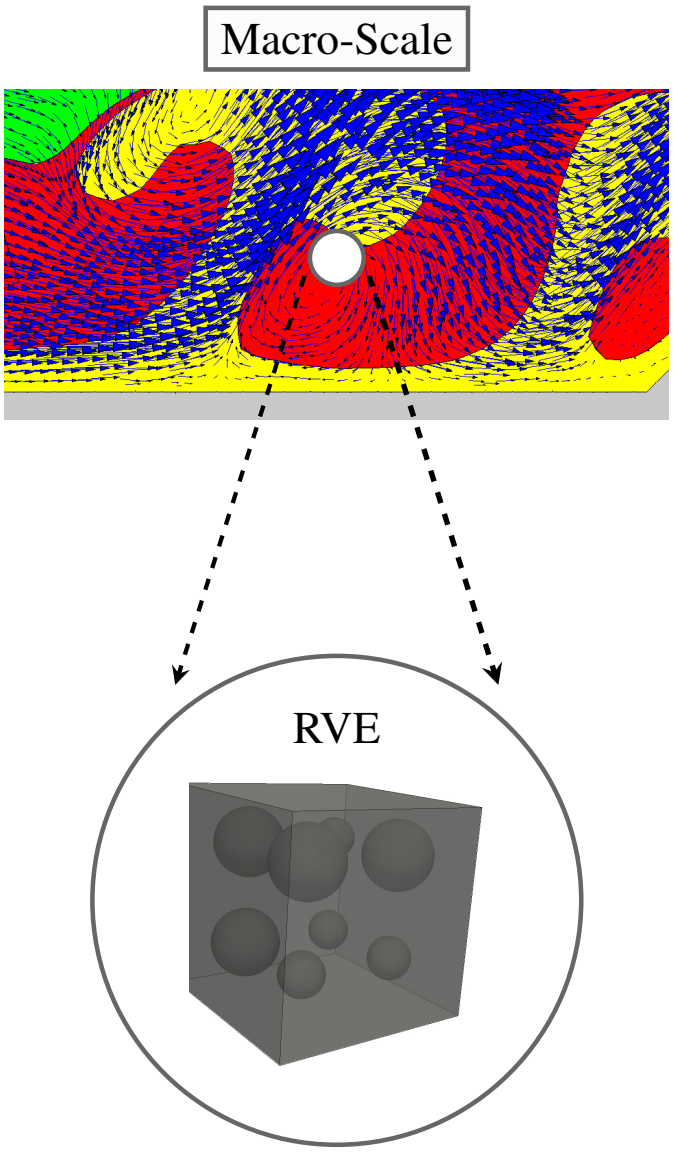

Figure 1.1: Multi scale.

Over the past decade, the use of analytical, numerical and experimental tools for the prediction of the heterogeneous materials properties has been the subject of increasing interest in academia, as indicated by the volume of literature.

Analytical approaches All analytical techniques rely on different assumptions which are approximation of the realistic physical conditions at the micro-scale. The Analytical determination of the properties of composite materials begins with names, J. C. Maxwell [1] and Lord Rayleigh [2] estimating the effective conductivity of composites with certain distributions of spherical particles embedded in a matrix see Figure 1.2. The effective medium approximation is another approach that estimates the overall behavior of heterogeneous materials. This method has been proposed by a number of authors, e.g. [3–5]. The estimation of the material properties are derived from the analytical form of a boundary value problem for a spherical or ellipsoidal inclusion of one material bounded in an infinite matrix. The self-consistent method leans to the previous method. This is another approach of homogenization scheme which first was proposed by [6], this theory, consider the polycrystalline structure as ellipsoidal inclusion placed in homogeneous matrix. This method extended to the elastoplastic, viscoplastic and allow each grain has different deformation behavior. However, these types of models do not fulfill the inhomogeneity between the materials.

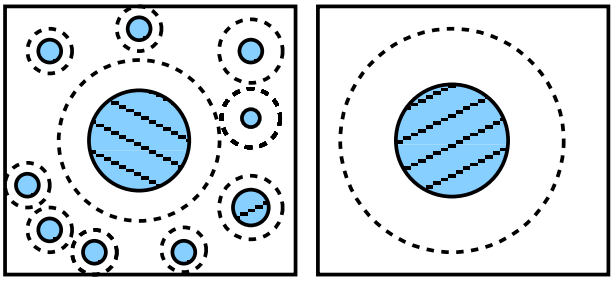

Figure 1.2: RVEs for analytical approaches.

The approach to estimate the overall properties of heterogeneous materials is the asymptotic homogenization theory [7]. This method is suitable for separation of scales due to the microstructure existence and is approximated by the term *natural length parameter*, which relates the macro coordinates to micro coordinates by the

size ratio (see [8–11] for more details). However, this method is limited to the problems with simple microscopic geometries, material models and is performed in small strains.

The estimation of porous ductile materials properties has been extensively encountered in various engineering applications. The prediction of the failure behavior of different materials which depends on the coupling between void nucleation, growth and plastic deformation. The most common approach for the modeling of such a mechanical behavior is continuum micromechanical frameworks, which derived the geometry of porous media at the microstructural level. A now well-established approach is based on homogenization methods, focused on taking into account more general considerations, such as void shape effects [12; 13] or plastic anisotropy [14]. Most general plastic models, such as ceramic, rocks and ice behave in anisotropic manner due to their complex texture. But, the anisotropy that is caused by plastic strain during forming operations is small and can be neglected for most applications [15]. Phenomenological models can predict the anisotropic stress–strain response in metals with complex texture under large plastic strains [16]. However, it is computationally expensive to simulate such constitutive equations for the large scale engineering applications. Therefore, analytical yield functions of Phenomenological models based on a macroscopic criterion derived for a class of porous materials containing spherical or cylindrical voids.

A prototype anisotropic yield function was proposed by von-Mises [17]. Based on this work, a number of extensions yield functions have been established to describe the behavior of different material models and satisfy numerical predictions or to generate data close to the existing experimental results. For instance, the quadratic anisotropic yield function proposed by [18], this method showed the best fit for body centered cubic (bcc) materials and steels [19]. However, due to the different classes of materials, further improved formulations introduced by [20–26] to cover more complicated material behavior. In order to produce the advanced yield functions to predict the mechanical behavior of various material classes, more parameters are required to make the model more flexible and accurate. Also, experimental results to validate these parameters are more time consuming, expensive and difficult to carry out. Micromechanical models play an important role in evaluating yield surface

models; such approaches first proposed by [27] based on iso-stress approach and [28] developed a model based on iso-strain. Later, the Taylor method modified by [29] which is known as the Taylor-Bishop-Hill (TBH) method. This model has been used by many researchers [20; 23; 30] to approve yield functions and generate the analytical expressions for yield and flow surfaces of anisotropic polycrystalline materials [31–34].

Computational strategy Several numerical results provide detailed information on the geometries and constitutive nonlinearities of the representative micro-structure. Computational strategy of micro-structures based on discretization in terms of finite element method or fast and Fourier transforms have been proposed by [35–39] . The advantages of these methods for the simulation of RVEs include:

- considering both, stress equilibrium and strain compatibility at grain boundaries;
- description of a grain structure as long as the mesh is fine enough;
- taking into account both, the local grain interactions and intra-grain inhomogeneities associated with plastic deformation.

Also several methods have been proposed by [40–42] to improve the efficiency.
The basic ideas of computational homogenization theory have been provided in [9; 36; 43; 44], followed by more generalized form of this method in more recent works [37; 45–50]. These methods provide the stress and strain relationship at each point of the macro-continuum based on the behavior of a locally attached micro-level attribution which corresponds to the point in the macro-continuum to which it is attached.
The advantages of these methods are described in the following items:

- It is not necessary to apply constitutive model at macroscopic scale.
- They can be applied to any material models.
- They describe the macroscopic behavior through the microscopic-level.
- The volume averaging technique is independent from the finite element method [44; 47; 50] or any type of phenomenological plasticity [45; 46].

- The finite deformations can be applied to both micro and macro levels.

Multi-level simulations include simulations at both scales micro and macro, which can be performed concurrently (running simulations in parallel in microscopic and macroscopic) multi-scale analysis is not feasible for most practical applications. Therefor widely used approaches are to employ homogenization as a support to design constitutive models that can be used in macroscopic scale such a strategy is now a days commonly known as virtual laboratories. This method is using the analysis of a microscopic representative volume element (RVE) to evaluate the parameter of macroscopic strength criterion.

1.1 Aim of the Thesis

The aim of this work is to determine effective yield criteria for porous pressure sensitive solids and composite materials by employing a virtual testing strategy. One of the focus is on the pressure sensitivity typically displayed by geometarials, such as sandstone. Another focus is on the anisotropic behavior that arises from composite materials consisting of a series of parallel layers, such as rock-salt.
Virtual testing strategy is based on a kinematical variational basis of the family of homogenization based on small and large strain multi-scale constitutive theories. The formulation follows a unified variational formulation, which provides bounds on the effective material properties for a given choice of the Representative Volume Element (RVE).
To obtain the effective properties of pressure sensitive porous solid, the constitutive behavior of continuum matrix is assumed to follow the standard Drucker-Prager elasto-plastic model. The computationally generated effective yield criteria for porous solids are obtained for various RVE choices under different boundary conditions and compared against the recently proposed analytical estimates for Drucker-Prager type solids and the SR4 constitutive model for soft rocks. The developed computational approach is applied to estimate the effective properties of a realistic rock sample, thus illustrating a wide range of potential applications, which incurs a dramatic decrease in overall computational costs.
Another aspect is to investigate the anisotropic yield behavior of composite material

based on determining the response of RVE model under various loading conditions. The constitutive behavior of continuum matrix is following the von-Mises elasto-plastic model. The numerical generated effective yield surfaces for composite layered are obtained for a RVE with different boundary conditions such as, uniform tractions and periodic displacements. The predicted computational yield criteria are used to identify the parameters of the proposed analytical yield functions by Hill [18] and Hoffman [51].

1.2 Layout of the Thesis

Chapter 2: covers the basic aspects of continuum mechanics: kinematics of finite deformation, the deformation gradient tensor in addition to some measures of strain. This is followed by a description of the equation of motion in addition to the concept of stress from which the principle of virtual work is introduced. This also involves an alternative definition of several stress tensors. The boundary value problem is introduced in this chapter.

Chapter 3: provides the concept of general finite strain elasto-plasticity, followed by the derivation of general return mapping algorithm. To illustrate such concepts the derivation of the pressure sensitive Drucker-Prager model is discussed in detail, providing the general spatial tangent modulus, which is the crucial part of the implicit finite element method. Finally, introducing the SR4 model by [52] which is implemented in the explicit finite element method.

Chapter 4: introducing the summary of the implicit and explicit Finite Element method (FE) to non-linear solid mechanics. The implicit FE numerical solution will be used to solve the RVE problems later in this work. The FE approximation (discretization) of the non-linear boundary value problem (BVP) which is solved by Newton-Raphson (N-R) iterative algorithm is provided. Next, we introduce the explicit solver followed by the stress integration. Finally, the element methodology that is used in this work is introduced.

Chapter 5: describes well known classes of multi-scale theories for large strain in solid mechanics. By describing the equilibrium equations of the macro-continuum and the micro-structure at the reference configuration within the variational framework above, then introducing the coupling of scales (homogenization). This develops the homogenization of the strain (deformation gradient in large strain) and the stress, an essential aspect in the formulation of the multi-scale theory which is the Hill-Mandel Principle of Macro-homogeneity and the additive split of the microscopic displacement. A family of the kinematical constraints that can be imposed on the RVE will then be introduced next. Finally, presenting the numerical examples to illustrate the scope and benefits of the multi-scale computational strategy, such as the effect of boundary conditions, topology and distribution of heterogeneities.

Chapter 6: provides a brief summary of constitutive models considered in this work. Main steps of the virtual testing strategy are given and providing numerical examples and includes comparative analysis against the results available in literature. Finally the main conclusions and recommendations for future work are discussed.

Chapter 7: presents the computational yield surfaces of the composite layered in deviatoric-pressure stress diagram in 3-D model and principal stresses diagram under plane stress assumption. The effective yield surfaces are obtained under both periodic and uniform traction boundary conditions. The details of the set-up of the virtual laboratory are also introduced with some numerical examples. Finally, based on the predicted yield stress point of composite materials under plane stress assumption, the parameters for proposed analytical models by Hill [18] and Hoffman [51] are acquired with ellipse fit by Taubin's method [53].

Chapter 8: provides achievements from the presented work and suggestions for future work

Chapter 2

Elements of Continuum Mechanics

A continuum is a body made of an infinite number of particles with properties being those of the bulk material. The *continuum mechanics* is used to describe the mechanical behavior of such bodies. To consider these bodies as a continuous medium is essentially an approximation due to heterogeneities of all matter. And, this approximation depends on the order of the discontinuities with respect to the body under consideration. For example, the assumption is not accurate on the molecular level, as they are separated by empty space. However, in this study, heterogeneous materials are treated in a continuum manner, by describing the behavior of micro-constituents composing of the heterogeneous body on the continuum theory.
This chapter is concerned with the basic concepts of continuum mechanics. Starting with describing the *kinematics of finite deformation*, which is study of motion without reference to the cause. The concept is providing the deformation gradient tensor in addition to some measures of strain. This is then followed by a description of the equation of motion in addition to the concept of *stress* from which the *principle of virtual work* is introduced. This also involves an alternative definition of several stress tensors. Also, the *boundary value problem* is introduced in this chapter, providing the concept of the finite element approximation later in this work. The material introduced in the chapter is available in more details in a number of references. For the current work, it is referred to the book by [54] and [55].

2.1 Kinematics

Consider the motion of the body Ω from $t = t_0$ to $t = t_1$ in Figure 2.1. Let the

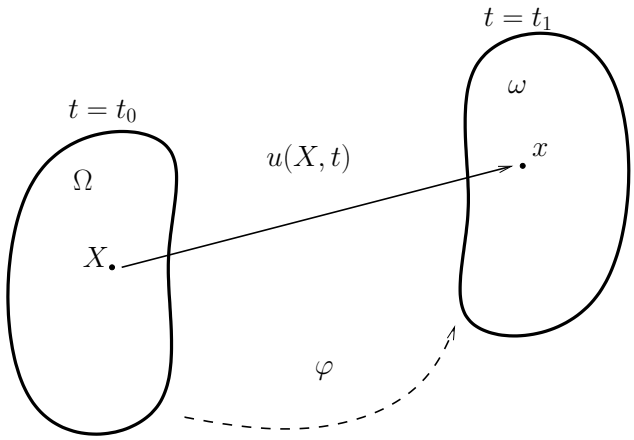

Figure 2.1: Generic motion of a deformable body from its reference configuration Ω to a current (deformed) configuration.

coordinates of the *initial configuration* be denoted by $\boldsymbol{X}$ at $t = t_0$ and the *current configuration* described by $\boldsymbol{x}$ at $t = t_1$. A material particle at position $\boldsymbol{X}$ is moved to a deformed position $\boldsymbol{x}$ located on the current body ω by a displacement vector $\boldsymbol{u}(\boldsymbol{X}, t)$ written with respect to the initial (undeformed) configuration. This motion can be described mathematically by the mapping φ between initial and the current particle positions as,

$$\boldsymbol{x} = \varphi(\boldsymbol{X}, t) = \boldsymbol{X} + \boldsymbol{u}(\boldsymbol{X}, t)\,. \tag{2.1}$$

2.1.1 Deformation Gradient

The deformation gradient $\boldsymbol{F}$ is the relation between infinitesimal vectors between two points in the reference to the corresponding vector in the deformed configuration. That is , $\boldsymbol{F}$ is a two-point tensor and is defined as,

$$\boldsymbol{F} = \frac{\partial \boldsymbol{x}}{\partial \boldsymbol{X}} = \frac{\partial(\boldsymbol{X} + \boldsymbol{u}(\boldsymbol{X}, t))}{\partial \boldsymbol{X}}\,, \tag{2.2}$$

or can be written in the form,

$$\boldsymbol{F} = \boldsymbol{I} + \nabla \boldsymbol{u}\,, \tag{2.3}$$

where, $\boldsymbol{I}$ is the second-order identity tensor and $\nabla \boldsymbol{u}$ is the gradient operator with respect to the initial coordinate,

$$\nabla \boldsymbol{u} = \frac{\partial \boldsymbol{u}(\boldsymbol{X})}{\partial \boldsymbol{X}} , \tag{2.4}$$

It is important to mention that small strain is an approximation of the non-linear terms for infinitesimal displacements and rotations. Therefore, there is only one configuration to work on. However, in non-linear behavior, is essential to make a distinction between bodies, expressed with respect to its reference and current configurations. The first is known as a material (Lagrangian) description whereas the latter refers to a spatial (Eulerian) description. Tensors are defined similarly into material (Lagrangian) and spatial (Eulerian) tensors implying the description they refer to.

2.1.2 Polar Decomposition

Polar decomposition of the deformation gradient is decomposing the total deformation $\boldsymbol{F}$ into the rotation and the stretch tensors. The mathematical description of the polar decomposition in both material and spatial configuration, are as

$$\boldsymbol{F} = \boldsymbol{R}\boldsymbol{U} = \boldsymbol{R}\boldsymbol{V} , \tag{2.5}$$

where $\boldsymbol{R}$ is the orthogonal rotation tensor, i.e. $\boldsymbol{R}\boldsymbol{R}^T = \boldsymbol{I}$. While $\boldsymbol{U}$ and $\boldsymbol{V}$ are symmetric stretch tensors, i.e. $\boldsymbol{U} = \boldsymbol{U}^T$, known as material (right) and spatial (left) stretch tensors respectively. The right and left stretch tensors can be related by rotation tensor. The great details of the polar decomposition concept is provided in [54].

2.1.3 Volume Change and Isochoric / Volumetric Split

The volume of the element is expressed as,

$$\begin{aligned} \mathrm{d}v &= \mathrm{d}\boldsymbol{x}_1 \cdot (\mathrm{d}\boldsymbol{x}_2 \times \mathrm{d}\boldsymbol{x}_3) \\ &= \boldsymbol{F}\mathrm{d}\boldsymbol{X}_1 \cdot (\boldsymbol{F}\mathrm{d}\boldsymbol{X}_2 \times \boldsymbol{F}\mathrm{d}\boldsymbol{X}_3) \\ &= \det[\boldsymbol{F}]\,\mathrm{d}V \\ &= J\mathrm{d}V\,, \end{aligned} \tag{2.6}$$

where, $\mathrm{d}\boldsymbol{x}_1$, $\mathrm{d}\boldsymbol{x}_2$ and $\mathrm{d}\boldsymbol{x}_3$ are side of a volume element in the deformed configuration and J is the Jacobian.

Any deformation can be split into an *isochoric* or *distortional* and purely *volumetric* component. Therefore, the multiplicative split of the deformation gradient can be expressed as,

$$\boldsymbol{F} = \boldsymbol{F}_{\mathrm{iso}}\boldsymbol{F}_{\mathrm{vol}}\,, \tag{2.7}$$

where,

$$\boldsymbol{F}_{\mathrm{iso}} = J^{\frac{-1}{3}}\boldsymbol{F} \quad ; \quad \boldsymbol{F}_{\mathrm{vol}} = J^{\frac{1}{3}}\boldsymbol{I}\,,$$

The aim of splitting the components into the isochoric and volumetric is, to remove the contribution of the distortional component of the deformation to any volume changes. Mostly in case of compressible and nearly incompressible materials. The mathematical expression of distortional contribution is as,

$$\det[\boldsymbol{F}_{\mathrm{iso}}] = (J^{\frac{-1}{3}})^3\det[\boldsymbol{F}] = J^{-1}J = 1\,.$$

2.1.4 Velocity and Velocity Gradient

According to the velocity definition and the equation (2.1), the velocity of a particle in spatial quantity is as,

$$\boldsymbol{v}(\boldsymbol{x}, t) = \frac{\partial\varphi(\boldsymbol{x}, t)}{\partial t}\,, \tag{2.8}$$

And, the *velocity gradient*, $\boldsymbol{l}$ is the derivation of the expression above with respect to the spatial coordinates as,

$$\boldsymbol{l} = \frac{\partial\boldsymbol{v}}{\partial\boldsymbol{x}} = \nabla\boldsymbol{v} = \dot{\boldsymbol{F}}\boldsymbol{F}^{-1}\,. \tag{2.9}$$

where, $\dot{\boldsymbol{F}}$, is the time derivative of the deformation gradient.

2.1.5 Strain

With deformation gradient tensor, several strain tensors can be introduced. Strain tensors are computed in both material or spatial configurations. Some of the strain tensors in each category will be described in the following. Starting by taking the scalar product of $\mathrm{d}\boldsymbol{x} \cdot \mathrm{d}\boldsymbol{x}$

$$\mathrm{d}\boldsymbol{x} \cdot \mathrm{d}\boldsymbol{x} = \boldsymbol{F}\mathrm{d}\boldsymbol{X} \cdot \boldsymbol{F}\mathrm{d}\boldsymbol{X} = \mathrm{d}\boldsymbol{X} \cdot \boldsymbol{F}^T\boldsymbol{F}\mathrm{d}\boldsymbol{X} = \mathrm{d}\boldsymbol{X} \cdot \boldsymbol{C}\mathrm{d}\boldsymbol{X}\,, \tag{2.10}$$

where $\boldsymbol{C} = \boldsymbol{F}^T\boldsymbol{F}$ is the *right Cauchy-Green tensor* which is in initial configuration. The scalar product of the initial configuration in the similar manner gives the *left Cauchy-Green strain tensor* $\boldsymbol{b} = \boldsymbol{F}\boldsymbol{F}^T$ as,

$$\mathrm{d}\boldsymbol{X} \cdot \mathrm{d}\boldsymbol{X} = \mathrm{d}\boldsymbol{x} \cdot \boldsymbol{b}^{-1}\mathrm{d}\boldsymbol{x}\,, \tag{2.11}$$

The change in the scalar product is the *Lagrangian* or *Green* strain tensor and operates in the initial configuration as,

$$\boldsymbol{E} = \frac{1}{2}(\boldsymbol{C} - \boldsymbol{I})\,. \tag{2.12}$$

Alternatively, the scalar product can be expressed as strain in the current configuration, *Eulerian* or *Almansi*, $\boldsymbol{e}$, strain tensor as,

$$\boldsymbol{e} = \frac{1}{2}(\boldsymbol{I} - \boldsymbol{b}^{-1})\,. \tag{2.13}$$

Note that, the vectors and tensors between material and spatial configurations can be related by the concepts of *push forward* and *pull back*. Therefore, $\boldsymbol{E}$ and $\boldsymbol{e}$ can be related as,

$$\begin{aligned} \boldsymbol{e} &= \boldsymbol{F}^{-T}\boldsymbol{E}\boldsymbol{F}^{-1}\,. \\ \boldsymbol{E} &= \boldsymbol{F}^T\boldsymbol{e}\boldsymbol{F}\,. \end{aligned} \tag{2.14}$$

By writing the right Cauchy-Green tensor, $\boldsymbol{C}$ according to the equation (2.3), the *Green* strain tensor can be written as,

$$\begin{aligned}\boldsymbol{E} &= \frac{1}{2}((\boldsymbol{I} + \nabla \boldsymbol{u})^T(\boldsymbol{I} + \nabla \boldsymbol{u}) - \boldsymbol{I}) \\ &= \boldsymbol{\varepsilon} + \frac{1}{2}(\boldsymbol{\varepsilon}\boldsymbol{\varepsilon} - \boldsymbol{\varepsilon}\boldsymbol{w} + \boldsymbol{w}\boldsymbol{\varepsilon} + \boldsymbol{w}\boldsymbol{w})\,.\end{aligned} \tag{2.15}$$

If $||\boldsymbol{\varepsilon}||$ and $||\boldsymbol{w}|| \ll 1$, then $\boldsymbol{\varepsilon}$ is and approximation of $\boldsymbol{E}$ and known as the *infinitesimal strain tensor* and $\boldsymbol{w}$ is *infinitesimal rotation tensor*. The approximation can be true if the both deformation and rotation are infinitesimal.

2.2 Stress and Equilibrium

In solid mechanics, the aim is to determine the reaction of a body under different loadings, these reactions are the consequence of the equilibrium equations describing the equation of motion which is known as the *strong form* of the problem. In order to start the finite element analysis, the integral form of the strong form (the *weak form*) is required, this is also known as the *principle of virtual work* (PVW). Stress is force per unit area simply. However, in finite strain analysis, there are two configurations, as the change in area is noticeable. Therefore, change in kinematic quantities can not be ignored. The stress can be defined in either initial or deformed configuration.

In this section, the equation of the motions will be introduced. Then the spatial virtual work equation will be provided. This also involves the definition of alternative stress measures, such as, the Kirchoff, first Piola-Kirchoff and second Piola-Kirchoff stress tensor.

2.2.1 Equations of Motion

Consider a body with region Ω and a boundary, $\partial\Omega$. The body is subjected to body forces acting on Ω and boundary forces which act on $\partial\Omega$ will be on motion. The linear and angular momentum balance equations that express the motion on a body

are:

$$\begin{aligned} \int_{\Omega} \rho\, \boldsymbol{b}\, \mathrm{d}v + \int_{\partial\Omega} \boldsymbol{t}\,(\boldsymbol{n})\mathrm{d}a &= \int_{\Omega} \rho\, \ddot{\boldsymbol{x}}\, \mathrm{d}v \\ \int_{\Omega} \rho\, \boldsymbol{x} \times \boldsymbol{b}\, \mathrm{d}v + \int_{\partial\Omega} \boldsymbol{x} \times \boldsymbol{t}\,(n)\, \mathrm{d}a &= \int_{\Omega} \rho\, \boldsymbol{x} \times \ddot{\boldsymbol{x}}\, \mathrm{d}v\,. \end{aligned} \tag{2.16}$$

where, $\boldsymbol{t}\,(n)$ is *surface traction*.

2.2.2 Stress

Consider an infinitesimal area $\Delta\, a$ of a particle position $\boldsymbol{x}$ as shown in Figure 2.2 at its current configuration ω. The corresponding traction force of the resultant force acting on this area, is in the form

$$\boldsymbol{t}_d\,(\boldsymbol{n}) \equiv \lim_{\Delta a \to 0} \frac{\Delta \boldsymbol{f}_d}{\Delta\, a}\,, \tag{2.17}$$

where, $\boldsymbol{n}$ and $\Delta \boldsymbol{f}_d$ are the outward normal and the resulatnt force to $\Delta\, a$ respectively. The traction force is following the Newton's third law, as,

$$\boldsymbol{t}_d\,(-\boldsymbol{n}) = -\boldsymbol{t}_d\,(\boldsymbol{n})\,. \tag{2.18}$$

The *Cauchy stress* tensor $\boldsymbol{\sigma}$ relates this traction force to the normal vector as,

$$\boldsymbol{t}_d\,(\boldsymbol{n}) \equiv \boldsymbol{\sigma}\boldsymbol{n}\,. \tag{2.19}$$

By taking the Gauss theorem of the integral form of (2.19) and, substituting it back to (2.16), defining $\boldsymbol{f}$ as the body force and zero acceleration, the global equilibrium equations in deformed configuration become,

$$\int_{\omega} \boldsymbol{f}\, \mathrm{d}v + \int_{\partial\omega} \mathrm{div}\,[\boldsymbol{\sigma}]\, \mathrm{d}v = \int_{\omega} (\mathrm{div}\,[\boldsymbol{\sigma}] + \boldsymbol{f})\, \mathrm{d}v = \boldsymbol{0}\,, \tag{2.20}$$

The above equation can be applied to any region of integration. Hence, it can be written as,

$$\mathrm{div}\,[\boldsymbol{\sigma}] + \boldsymbol{f} = \boldsymbol{0}\,. \tag{2.21}$$

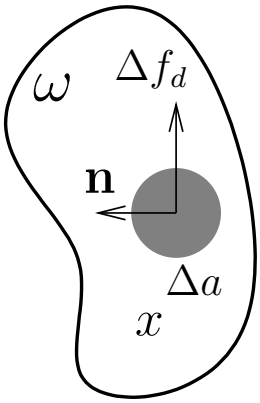

Figure 2.2: Deformed configuration of a generic deformable body illustrating the resultant force on an infinitesimal area.

2.2.3 Virtual Work

The weak form of the equilibrium equation (2.21) is the start point of the *Finite Element* (FE) formulation, essential for the solution of the engineering problems and is employed in the present work. This explains the use of the *Principle of Virtual Work* (PVW). The virtual work, δW is obtained by applying an arbitrary virtual displacement, $\boldsymbol{\eta}$ in the current configuration to equation (2.21) as shown below,

$$\delta W = \underbrace{\int_{\omega} \boldsymbol{\sigma} : \nabla\boldsymbol{\eta}\, \mathrm{d}v}_{\delta W_{int}} - \overbrace{\int_{\partial\omega} \boldsymbol{t}\cdot\boldsymbol{\eta}\, \mathrm{d}a - \int_{\omega} \boldsymbol{f}\cdot\boldsymbol{\eta}\, \mathrm{d}v}^{\delta W_{ext}} = \mathbf{0}\,. \tag{2.22}$$

2.2.4 Stress Definitions

In view of equation (2.22), the terms $\boldsymbol{\sigma}$ and $\nabla\boldsymbol{\eta}$ are called internal virtual work in the current deformed volume. This can be used to constructed alternative stresses definitions in the following:

Kirchoff Stress Tensor

By using equation (2.6), the current volume can be written as, $\mathrm{d}v = J\mathrm{d}V$. Therefore the internal work term can be expressed as,

$$\delta W_{int} = \int_{\Omega} J\boldsymbol{\sigma} : \nabla\boldsymbol{\eta}\, \mathrm{d}V\,. \tag{2.23}$$

The term $\boldsymbol{\tau} = J\boldsymbol{\sigma}$ is the *Kirchoff stress tensor* with respect to the initial configuration.

First Piola-Kirchoff Stress Tensor

The *first Piola-Kirchhoff stress tensor*, similar to $\boldsymbol{F}$, is a two-point tensor that can be related to the Cauchy stress via the following relation,

$$\boldsymbol{P} = J\boldsymbol{\sigma}\boldsymbol{F}^{-T} . \tag{2.24}$$

It is also useful to express the weak form of the equilibrium equation in terms of the first Piola-Kirchhoff stress in the reference configuration. This gives

$$\delta W = \underbrace{\int_{\Omega} \boldsymbol{P} : \nabla\boldsymbol{\eta}\, \mathrm{d}V}_{\delta W_{int}} - \overbrace{\int_{\partial\Omega} \boldsymbol{t}\cdot\boldsymbol{\eta}\, \mathrm{d}A - \int_{\Omega} \boldsymbol{f}\cdot\boldsymbol{\eta}\, \mathrm{d}V}^{\delta W_{ext}} = \boldsymbol{0} . \tag{2.25}$$

Second Piola-Kirchoff Stress Tensor

As the first Piola-Kirchhoff is a two-point tensor and not completely defined in terms of quantities in the initial configuration, the *second Piola-Kirchhoff stress tensor*, a material stress tensor, is defined. This tensor is expressed in terms of the Cauchy stress and the first Piola-Kirchhoff stress as

$$\boldsymbol{S} = J\boldsymbol{F}^{-1}\boldsymbol{\sigma}\boldsymbol{F}^{-T} = \boldsymbol{F}^{-1}\boldsymbol{P} . \tag{2.26}$$

2.3 Boundary Value Problem

To solve the equilibrium equations (2.22) and (2.25), the *Boundary Value Problem* (BVP) is required to be set. Given the body force and surface traction fields on the body, find a kinematically admissible deformation $\varphi \in \mathscr{K}$ such

$$\int_{\omega} \hat{\boldsymbol{\sigma}} : \nabla\boldsymbol{\eta}\, \mathrm{d}v - \int_{\partial\omega} \boldsymbol{t}\cdot\boldsymbol{\eta}\, \mathrm{d}a - \int_{\omega} \boldsymbol{f}\cdot\boldsymbol{\eta}\, \mathrm{d}v = \boldsymbol{0} \quad \forall\boldsymbol{\eta} \in \mathscr{V} , \tag{2.27}$$

where, $\hat{\boldsymbol{\sigma}}$ is constitutive functional and is used for elastic/plastic bodies where the stress is the function of strain, $\hat{\boldsymbol{\sigma}}(\boldsymbol{F})$ or $\hat{\boldsymbol{\sigma}}(\varepsilon)$ and, $\mathscr{K}$ and $\mathscr{V}$ are the space of kinematically admissible displacements and the space of virtual kinematically admissible displacements of the body respectively.

2.3.1 Incremental Boundary Value Problem

First we need to introduce the incremental constitutive law briefly. In general, pseudo-time discretization is adopted to integrate constitutive equations, considering the time increment $[t^n, t^{n+1}]$ and given the set of internal variables at initial time, the strain at time t^{n+1}, determine the stress at time t^{n+1} through the integration algorithm in question as,

$$\boldsymbol{\sigma}^{n+1} = \hat{\boldsymbol{\sigma}}(\boldsymbol{F}^{n+1}, \boldsymbol{\alpha}^n) \quad \text{or} \quad \boldsymbol{\sigma}^{n+1} = \hat{\boldsymbol{\sigma}}(\varepsilon^{n+1}, \boldsymbol{\alpha}^n) \tag{2.28}$$

where, $\boldsymbol{\alpha}$ is a set of internal variables. The constitutive models that are used in this work is explained in more details in Chapter 3.

So that the incremental form of the boundary value problem can be stated as follows:

$$\int_\omega \boldsymbol{\sigma}^{n+1} : \nabla\boldsymbol{\eta}\, \mathrm{d}v - \int_{\partial\omega} \boldsymbol{t}^{n+1} \cdot \boldsymbol{\eta}\, \mathrm{d}a - \int_\omega \boldsymbol{f}^{n+1} \cdot \boldsymbol{\eta}\, \mathrm{d}v = \mathbf{0} \quad \forall\boldsymbol{\eta} \in \mathscr{V}\,. \tag{2.29}$$

Chapter 3

Constitutive Models: Formulation and Numerical Integration

Constitutive models are defined as the relationship between load-deformation or stress-strain. In this work, the mechanical behavior of engineering materials show in terms of stress-strain as, the equilibrium equations in chapter 2 is written in terms of measure of stress. The constitutive models have been given significant attention due to their potential application in many areas of practical engineering interest. They hold the continuum concepts of elasticity, plasticity, viscosity and can consider all the thermal effects.

In this chapter, the concept of general finite strain elasto-plasticity will be introduced. Followed by the derivation of general return mapping algorithm. To illustrate such concepts, the derivation of pressure sensitive Drucker-Prager model is discussed in details, providing the general spatial tangent modulus which is the crucial part of the implicit finite element method. Finally, introducing the SR4 model by [52] which is implemented in the explicit finite element method.

The more details of this chapter can be found in [54; 56–58], .

3.1 Large Strain Elasto-Plasticity Model

In this section, the general form of the finite strain plasticity is introduced in detail. The theory described here forms the basis of the isotropic large strain plasticity framework and the finite element implementation (incorporated in program HY-

PLAS) is addressed in the following section. Some of the crucial features of the model is selected in the following.

3.1.1 Multiplicative Elasto-Plasticity Kinematics

The *multiplicative decomposition* of the deformation gradient, $\boldsymbol{F}$ has been an intense subject in constitutive assumption since its introduction by [59] and [60]. It decomposes the deformation gradient as the product of elastic $\boldsymbol{F}^e$ and plastic $\boldsymbol{F}^p$ deformation gradient.

$$\boldsymbol{F} = \boldsymbol{F}^e \boldsymbol{F}^p. \tag{3.1}$$

As the concept shown in Figure 3.1, $\boldsymbol{F}^p$ maps the particle to the stress-free intermediate configuration from the initial configuration and $\boldsymbol{F}^e$ maps the particle from intermediate to the current configuration. However in small strain, the intermediate configuration is defined by $\varepsilon - \varepsilon^e$.

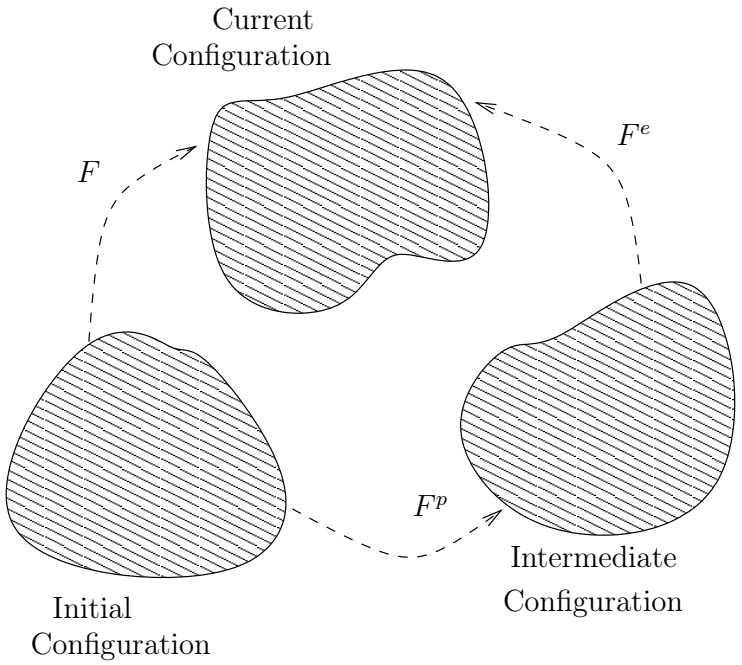

Figure 3.1: The deformation gradient multitive decomposition.

Elastic and Plastic Stretch and Rotation Tensors

According to the above multiplicative decomposition, the polar decomposition in equation (2.5) in section 2.1.2 can be written as,

$$\boldsymbol{F}^e = \boldsymbol{R}^e \boldsymbol{U}^e = \boldsymbol{V}^e \boldsymbol{R}^e \tag{3.2}$$

And similarly for the plastic part of the deformation gradient,

$$\boldsymbol{F}^p = \boldsymbol{R}^p \boldsymbol{U}^p = \boldsymbol{V}^p \boldsymbol{R}^p . \tag{3.3}$$

where, $\boldsymbol{U}$ is the right stretch tensor, $\boldsymbol{V}$ is the left stretch tensor and $\boldsymbol{R}$ is the rotation tensor which are split into elastic (e) and plastic (p).

The Velocity Gradient

With introducing the multiplicative split into the equation (2.9), gives the additive decomposition of the velocity gradient as,

$$\boldsymbol{l} = \boldsymbol{l}^e + \boldsymbol{F}^e \boldsymbol{l}^p (\boldsymbol{F}^e)^{-1} . \tag{3.4}$$

As mentioned in section 2.1.4, $\boldsymbol{l}$ is in the spatial configuration. Whereas, the plastic velocity gradient, $\boldsymbol{l}^p$ is in intermediate configuration. Therefore, to keep it consistent, we pre- and post-multiplied the plastic deformation gradient by $\boldsymbol{F}^e$ and its inverse, this provides the above plastic contribution to $\boldsymbol{l}$ a spatial quantity.

The Plastic Stretching and Spin Tensors

The plastic stretching, $\boldsymbol{D}^p = \text{sym}[\boldsymbol{l}^p]$ and spin tensors, $\boldsymbol{W}^p = \text{skew}[\boldsymbol{l}^p]$ are analogous to the decomposition of the velocity gradient.
The plastic stretch tensor $\boldsymbol{D}^p$ follows the similar interpretation as the stretch tensor, $\boldsymbol{D}$ but, as the plastic strech tensor is associated with the $\boldsymbol{F}^p$ which is in intermediate configuration and not the spatial configuration. Therefore, we rotate the $\boldsymbol{D}^p$ as,

$$\tilde{\boldsymbol{D}}^p \equiv \boldsymbol{R}^e \boldsymbol{D}^p \boldsymbol{R}^{eT} \tag{3.5}$$

where, $\tilde{\boldsymbol{D}}^p$ is called the *spatially rotated* plastic stretching. It can also be represented by the eigenvectors, $\boldsymbol{e}_i$ and the the eigenvalue, d_i^p as,

$$\tilde{\boldsymbol{D}}^p = \sum_{i=1}^{3} d_i^p \tilde{\boldsymbol{e}}_i \otimes \tilde{\boldsymbol{e}}_i \,, \tag{3.6}$$

where, $\tilde{\boldsymbol{e}}_i = \boldsymbol{R}^e \boldsymbol{e}_i$.

3.1.2 Logarithmic Elastic Strain

In the present general model of finite strain elasto-plasticity, the logarithmic strain will be adopted to measure elastic deformations. It is convenient to use the logarithmic (or natural) strain measure to describe the elastic behavior. In addition is suitable approximations to the plastic flow rule, results in substantial simplifications in the stress integration algorithm. And, it allows a natural extension to the finite strain range, of the elastic predictor/return-mapping algorithms of infinitesimal elasto-plasticity. The Eulerian logarithmic elastic strain is defined by

$$\boldsymbol{\varepsilon}^e = \frac{1}{2} \ln \boldsymbol{b}^e, \tag{3.7}$$

where, $\boldsymbol{b}^e = \boldsymbol{F}^e (\boldsymbol{F}^e)^T$

Deviatoric and Volumetric Logarithmic Strains

The split form of the elastic logarithmic strain into deviatoric/volumetric, we obtain

$$\boldsymbol{\varepsilon}^e = \boldsymbol{\varepsilon}_{\mathrm{d}}^e + \varepsilon_{\mathrm{v}}^e \boldsymbol{I}, \tag{3.8}$$

The volumetric logarithmic strain is as,

$$\varepsilon_{\mathrm{v}}^e \equiv \mathrm{tr}[\boldsymbol{\varepsilon}^e] = \ln J^e, \quad J^e = \det \boldsymbol{F}^e. \tag{3.9}$$

3.1.3 General Finite Strain Plasticity Model

In order to define the generalized form of isotropic hyperelastic/plastic finite strain constitutive models, the essential equations are presented in the following.

The Free-Energy Potential

The general form of the free-energy potential in this work is from the basic energy and thermodynamic statement discussed in more details in [54] and [61], is expressed as,

$$\psi(\boldsymbol{\varepsilon}^e, \boldsymbol{\alpha}) \tag{3.10}$$

where, $\boldsymbol{\alpha}$ is generic set of internal variables associated with dissipative mechanisms. The *Kirchhoff* stress tenor is derived from the potential free-energy as,

$$\boldsymbol{\tau} = \bar{\rho}\, \frac{\partial \psi}{\partial \boldsymbol{\varepsilon}^e}\,. \tag{3.11}$$

Note that, the thermal effect is ignored in this work.

The Yield Criterion

The general yield function, $\Phi(\boldsymbol{\tau}, \boldsymbol{A})$, given in the spatial configuration in terms of the *Kirchhoff* stress and set $\boldsymbol{A}$ of conjugate thermodynamical forces.
The *set of admissible kirchhof stresses* is defined as

$$\bar{\mathscr{E}} = \{\boldsymbol{\tau} \mid \Phi(\boldsymbol{\tau}, \boldsymbol{A}) \leq 0\}. \tag{3.12}$$

Plastic yielding may take place if $\boldsymbol{\tau}$ lies on the yield surface (boundary of the elastic domain).

Finite Strain Plastic Flow Rule

The *plastic flow potential*, $\Psi(\boldsymbol{\tau}, \boldsymbol{A})$, expressed as kirchhoff stress and the thermodynamical force, $\boldsymbol{A}$ as well. The rotated plastic stretching is used here as the plastic flow is in spatial configuration. It is defined as,

$$\tilde{\boldsymbol{D}}^p = \dot{\gamma} \frac{\partial \Psi}{\partial \boldsymbol{\tau}}\,, \tag{3.13}$$

And zero plastic spin, $\boldsymbol{W}^p = 0$.
Also the plastic deformation gradient can be evaluated from the plastic flow rule

above and the equation (3.5) as,

$$\boldsymbol{l}^p \equiv \dot{\boldsymbol{F}}^p(\boldsymbol{F}^p)^{-1} = \dot{\gamma}\,\boldsymbol{D}^p \tag{3.14}$$

Internal Variables

A general equation for the internal variables is

$$\dot{\boldsymbol{\alpha}} = \dot{\gamma}\boldsymbol{H}(\boldsymbol{\tau}, \boldsymbol{A}) = -\dot{\gamma}\frac{\partial \Psi}{\partial \boldsymbol{A}}, \tag{3.15}$$

where the plastic multiplier, $\dot{\gamma}$, is required to satisfy the standard complementarity relation

$$\Phi \leq 0\,, \quad \dot{\gamma} \geq 0\,, \quad \dot{\gamma}\Phi = 0. \tag{3.16}$$

3.1.4 The Dissipation Inequality

By taking the time derivative of the free-energy equation and using equation (3.7),

$$\begin{aligned} \dot{\psi} &= \frac{1}{2}\frac{\partial \psi}{\partial \boldsymbol{\varepsilon}^e} : \frac{\partial \ln \boldsymbol{b}^e}{\partial \boldsymbol{b}^e} : \dot{\boldsymbol{b}}^e + \frac{1}{\bar{\rho}}\,\boldsymbol{A} * \dot{\boldsymbol{\alpha}} \\ &= \frac{1}{2}\left[\frac{\partial \psi}{\partial \boldsymbol{\varepsilon}^e} : \frac{\partial \ln \boldsymbol{b}^e}{\partial \boldsymbol{b}^e}\right]\boldsymbol{b}^e : \dot{\boldsymbol{b}}^e\,\boldsymbol{b}^{e-1} + \frac{1}{\bar{\rho}}\,\boldsymbol{A} * \dot{\boldsymbol{\alpha}}. \end{aligned} \tag{3.17}$$

The equation above can be written as,

$$\dot{\psi} = \frac{1}{2}\frac{\partial \psi}{\partial \boldsymbol{\varepsilon}^e} : \dot{\boldsymbol{b}}^e\,\boldsymbol{b}^{e-1} + \frac{1}{\bar{\rho}}\,\boldsymbol{A} * \dot{\boldsymbol{\alpha}}. \tag{3.18}$$

By using multiplicative elastoplastic decomposition, the $\boldsymbol{b}^e$ can be expanded to, $\boldsymbol{b}^e = \boldsymbol{F}(\boldsymbol{F}^p)^{-1}(\boldsymbol{F}^p)^{-T}\boldsymbol{F}^T$. Therefore, the above expression can rewrite as,

$$\begin{aligned} \dot{\psi} = \frac{\partial \psi}{\partial \boldsymbol{\varepsilon}^e} : \Big\{ \boldsymbol{D} + \frac{1}{2}[\boldsymbol{F}^e\boldsymbol{F}^p(\boldsymbol{F}^{p-1})\boldsymbol{F}^{eT} + \boldsymbol{F}^e(\boldsymbol{F}^{p-T})\boldsymbol{F}^{pT}\boldsymbol{F}^{e-1}] \Big\} \\ + \frac{1}{\bar{\rho}}\boldsymbol{A} * \dot{\boldsymbol{\alpha}}, \end{aligned} \tag{3.19}$$

Finally, with the introduction of definition (3.13) of the spatially rotated plastic stretching tensor, $\tilde{\boldsymbol{D}}^p$, and by taking into account the elastic isotropy, the rate of

change of free energy can be expressed as

$$\dot{\psi} = \frac{\partial \psi}{\partial \boldsymbol{\varepsilon}^e} : (\boldsymbol{D} - \tilde{\boldsymbol{D}}^p) + \frac{1}{\bar{\rho}} \boldsymbol{A} * \dot{\boldsymbol{\alpha}}. \tag{3.20}$$

3.1.5 Finite Strain to Infinitesimal Theories

The finite strain model equations above can be treated as small strain plasticity in the present approach. Some of the important properties of this approach are, volumetric plastic deformation and the volumetric plastic flow.

According to the volumetric logarithmic strain in equation (3.9), the volumetric plastic strain can also be written as,

$$\varepsilon_{\mathrm{v}}^p \equiv \ln J^p \tag{3.21}$$

With $J^p = \det \boldsymbol{F}^p$ and using principle plastic stretches, λ, the equation above can be written as,

$$\varepsilon_{\mathrm{v}}^p = \ln[\lambda_1^p \, \lambda_2^p \, \lambda_3^p] = \mathrm{tr}[\ln \boldsymbol{e}^p] \tag{3.22}$$

Note that, the plastic deformation is volume-preserving if and only if the above defined volumetric plastic strain vanishes, $\varepsilon_{\mathrm{v}}^p = 0$.

By taking the derivative of $\varepsilon_{\mathrm{v}}^p$, we obtain,

$$\dot{\varepsilon}_{\mathrm{v}}^p = \ln[\det \boldsymbol{F}^p] = \mathrm{tr}[\dot{\boldsymbol{F}}^p (\boldsymbol{F}^p)^{-1}] \tag{3.23}$$

Hence, the rate of the volumetric plastic strain can also reduce to small strain formulation as,

$$\dot{\varepsilon}_{\mathrm{v}}^p = \dot{\gamma} \, \mathrm{tr}\left[\frac{\partial \Psi}{\partial \boldsymbol{\tau}}\right] \tag{3.24}$$

In order to have isochoric plastic flow condition, the $\dot{\varepsilon}_{\mathrm{v}}^p = 0$ as, the volumetric of the plastic deformation gradient, J^p is constant. Therefore, it can be seen that from the equation above, the flow vector is traceless. The details are provided thoroughly in chapter 14 in [54].

3.1.6 General Return Mapping Algorithm

In this section, we described the integration algorithm based on finite strain analogous to the concepts above. Showing the relation between the infinitesimal plasticity models and the finite strain that is coded in HYPLAS and RVE-PLAS codes.

Initial Value Problem

First given the initial values of plastic deformation gradient at initial time, t_0 (could also use elastic deformation gradient.) and the hardening variables with the history of the deformation gradient. To find the following functions,

$$\begin{aligned} \dot{\boldsymbol{F}}^p(t)[\boldsymbol{F}^p(t)]^{-1} &= \dot{\gamma}(t)\boldsymbol{R}^e(t)^T \left.\frac{\partial \Psi}{\partial \boldsymbol{\tau}}\right|_t \boldsymbol{R}^e(t) \\ \dot{\boldsymbol{\alpha}}(t) &= \dot{\gamma}(t)\boldsymbol{H}(\boldsymbol{\tau}(t)\,,\boldsymbol{A}(t)) \end{aligned} \tag{3.25}$$

That satisfy,

$$\dot{\gamma}(t) \geq 0, \quad \Phi(\boldsymbol{\tau}(t)\,,\boldsymbol{A}(t)) \leq 0, \quad \dot{\gamma}(t)\Phi(\boldsymbol{\tau}(t)\,,\boldsymbol{A}(t)) = 0 \tag{3.26}$$

for each time instant $t \in [t_0, T]$

$$\boldsymbol{\tau}(t) = \bar{\rho}\left.\frac{\partial \psi}{\partial \boldsymbol{\varepsilon}^e}\right|_t, \quad \boldsymbol{A}(t) = \left.\frac{\partial \psi}{\partial \boldsymbol{\alpha}}\right|_t \tag{3.27}$$

By using the kinematic relations, we can relate $\boldsymbol{\varepsilon}^e$ to the elastic and plastic deformation gradient.

$$\begin{aligned} \boldsymbol{\varepsilon}^e(t) &= \ln([\boldsymbol{F}^e(t)\boldsymbol{F}^e(t)^T]^{\frac{1}{2}}) \\ \boldsymbol{F}^e(t) &= \boldsymbol{F}(t)[\boldsymbol{F}^p(t)]^{-1} \end{aligned} \tag{3.28}$$

Euler Discretization

By applying a backward Euler scheme to the equation (3.25), the incremental form of the hardening internal variables is as,

$$\boldsymbol{\alpha}_{n+1} = \boldsymbol{\alpha}_n + \Delta\gamma \boldsymbol{H}_{n+1}. \tag{3.29}$$

within generic pseudo time interval $[t_n, t_{n+1}]$.

The difference between the large strain and small strain is in discretization of the plastic flow equation. The *backward exponential map integrators* is used to discretized the plastic flow, leads to updated formula for the plastic deformation gradient

$$\boldsymbol{F}^p_{n+1} = exp\left[\Delta\gamma \boldsymbol{R}^{eT}_{n+1} \frac{\partial \Psi}{\partial \boldsymbol{\tau}}\bigg|_{n+1} \boldsymbol{R}^e_{n+1}\right] \boldsymbol{F}^p_n\Big], \tag{3.30}$$

By using basic property of the exponential map, the discretized form of the plastic flow equation follows a standard backward Euler difference scheme as,

$$\boldsymbol{F}^p_{n+1} = \left(\boldsymbol{I} - \Delta\gamma \boldsymbol{R}^{eT}_{n+1} \frac{\partial \Psi}{\partial \boldsymbol{\tau}}\bigg|_{n+1} \boldsymbol{R}^e_{n+1}\right] \boldsymbol{F}^p_n\Big)^{-1}. \tag{3.31}$$

By simple inspection, we can easily establish that the above update formula for $\boldsymbol{F}^p$ is not volume-preserving in general; that is, given $\boldsymbol{F}^p_n$ such that $\det[\boldsymbol{F}^p_n] \neq 1$ and a traceless $\dfrac{\partial \Psi}{\partial \boldsymbol{\tau}}$, the resulting $\boldsymbol{F}^p_{n+1}$ is such that, in general, $\det[\boldsymbol{F}^p_{n+1}]$. This approach would result in substantial accuracy loss in the numerical integration of elasto-plastic constitutive equations of plastically incompressible models. By applying the kinematic relations into the equation above and using exponential properties, we can have the discretized form of elastic deformation gradient in the form of,

$$\boldsymbol{F}^e_{n+1} = \underbrace{\boldsymbol{F}_{n+1}(\boldsymbol{F}^e_n)^{-1}}_{\boldsymbol{F}_\triangle} \boldsymbol{F}^e_n \boldsymbol{R}^{eT}_{n+1} \exp\left[\Delta\gamma \frac{\partial \Psi}{\partial \boldsymbol{\tau}}\bigg|_{n+1}\right] \boldsymbol{R}^e_{n+1}. \tag{3.32}$$

where, $\boldsymbol{F}_\triangle$ is *incremental* deformation gradient.

In order to be consistent with the infinitesimal counterpart, using the elastic deformation gradient as the unknown initial value. Therefore, using equation (3.32) instead of using (3.28). And, the update plastic strain can be calculated simply from the multiplicative elasto-plastic split as,

$$\boldsymbol{F}^p_{n+1} = (\boldsymbol{F}^e_{n+1})^{-1} \boldsymbol{F}_{n+1} \tag{3.33}$$

The Return Mapping Scheme

First is to solve the elastic trial step, by setting $\Delta\gamma = 0$ in equations (3.32) and (3.29),

$$\begin{aligned} \boldsymbol{F}^{e\,\text{trial}}_{n+1} &= \boldsymbol{F}_{\triangle}\boldsymbol{F}^{e}_{n} \\ \boldsymbol{\alpha}^{\text{trial}}_{n+1} &= \boldsymbol{\alpha}_{n} \end{aligned} \tag{3.34}$$

If the constitutive relations are at the elastic state, $\Phi(\boldsymbol{\tau}^{\text{trial}}_{n+1}, \boldsymbol{A}^{\text{trial}}_{n+1}) \leq 0$, then solving for the elastic trial at the next time step, t_{n+1}

$$\begin{aligned} \boldsymbol{F}^{e}_{n+1} &= \boldsymbol{F}^{e\,\text{trial}}_{n+1}\boldsymbol{R}^{eT}_{n+1}\exp\left[-\Delta\gamma\left.\frac{\partial\Psi}{\partial\boldsymbol{\tau}}\right|_{n+1}\right]\boldsymbol{R}^{e}_{n+1}. \\ \boldsymbol{\alpha}^{\text{trial}}_{n+1} &= \boldsymbol{\alpha}_{n} + \Delta\gamma\boldsymbol{H}_{n+1} \\ \Phi(\boldsymbol{\tau}^{\text{trial}}_{n+1}, \boldsymbol{A}^{\text{trial}}_{n+1}) &= 0 \end{aligned} \tag{3.35}$$

Logarithmic Strain and Infinitesimal Format of Return Mapping

For the computational use, it is better to simplify the equation $(3.35)_1$ and rewrite it in terms of the *logarithmic elastic strain*. This is showing in the following: by using left elastic stretch tensor, $\boldsymbol{V}^{e} = \boldsymbol{F}\boldsymbol{R}^{T}$ instead of elastic deformation gradient in the equation above and using exponential properties,

$$\boldsymbol{V}^{e}_{n+1}\exp\left[\Delta\gamma\left.\frac{\partial\Psi}{\partial\boldsymbol{\tau}}\right|_{n+1}\right] = \boldsymbol{F}^{e\,\text{trial}}_{n+1}\boldsymbol{R}^{e\,T}_{n+1} \tag{3.36}$$

Times both side by its transpose, gives,

$$\boldsymbol{V}^{e}_{n+1}\exp\left[2\Delta\gamma\left.\frac{\partial\Psi}{\partial\boldsymbol{\tau}}\right|_{n+1}\right]\boldsymbol{V}^{e}_{n+1} = (\boldsymbol{V}^{e\,\text{trial}}_{n+1})^{2}. \tag{3.37}$$

Because of the assumed elastic and plastic isotropy, $\boldsymbol{V}^{e}$ and $\dfrac{\partial\Psi}{\partial\boldsymbol{\tau}}$ commute. Then, by rearranging the terms and taking the square root of both sides of equation (3.37), we obtain

$$\boldsymbol{V}^{e}_{n+1} = \boldsymbol{V}^{e\,\text{trial}}_{n+1}\exp\left[2\Delta\gamma\left.\frac{\partial\Psi}{\partial\boldsymbol{\tau}}\right|_{n+1}\right]. \tag{3.38}$$

Now, we can simply rewrite the equation above in the form of logarithmic Eulerian strain tensors by taking tensor logarithm of both sides

$$\boldsymbol{\varepsilon}^{e}_{n+1} = \boldsymbol{\varepsilon}^{e\,\mathrm{trial}}_{n+1} - \Delta\gamma \left.\frac{\partial \Psi}{\partial \boldsymbol{\tau}}\right|_{n+1}. \tag{3.39}$$

Remarkably, the above expression has the same format as the elastic strain update formula of the backward return-mapping algorithms of the infinitesimal theory.

Computational Implementation of The General Algorithm

As the elastic law is defined here in terms of the spatial elastic logarithmic strain, in the actual computational implementation of the above elastic predictor/return-mapping procedure we shall take $\boldsymbol{\varepsilon}^{e}$ as the kinematic variable to be stored in the computer memory. Accordingly, the computational procedure follows the steps:

- By using elastic logarithmic strain, calculating the left Cauchy-Green tensor

$$\boldsymbol{b}^{e}_{n} = \exp[2\boldsymbol{\varepsilon}^{e}_{n}]; \tag{3.40}$$

- After having the initial left Cauchy-Green tensor, compute its elastic trial term

$$\boldsymbol{b}^{e\,\mathrm{trial}}_{n+1} = \boldsymbol{F}^{e\,\mathrm{trial}}_{n+1}(\boldsymbol{F}^{e\,\mathrm{trial}}_{n+1})^{T} = \boldsymbol{F}_{\triangle}\boldsymbol{b}^{e}_{n}(\boldsymbol{F}_{\triangle})^{T}; \tag{3.41}$$

- Now can relate the large strain to the small strain and, pass the elastic trial logarithmic strain tensor to the rest of the algorithm,

$$\boldsymbol{\varepsilon}^{e\,\mathrm{trial}} = \frac{1}{2}\ln \boldsymbol{b}^{e\,\mathrm{trial}}_{n+1}. \tag{3.42}$$

In the following section, The Drucker-Prager and SR4 pressure sensitive constitutive models by applying the general algorithm above are described.

3.2 The Constitutive Models

In this section, the complete computational implementation of the two models which are used in this work is described in detail. Namely, the models discussed here are

- the Drucker-Prager model,
- the SR4 (soft rock) model.

3.2.1 The Drucker-Prager Model

The Drucker–Prager yield criterion is a pressure-sensitive model to determine whether a material has failed or undergoes plastic yielding like other elasto-plastic material model. Due to its pressure-dependency the criterion is used to deal with the plastic deformation of materials, such as, soils, rock, concrete, polymers, foams, and other pressure-sensitive materials.

The Drucker-Prager yield surface and flow potential are formulated in the following equations respectively as,

$$\begin{aligned} \Phi(\boldsymbol{\sigma}, c) &= \sqrt{J_2(\boldsymbol{s}(\boldsymbol{\sigma}))} + \frac{\tan\phi}{\sqrt{3}} p(\boldsymbol{\sigma}) - c \\ \Psi(\boldsymbol{\sigma}, c) &= \sqrt{\boldsymbol{J}_2(\boldsymbol{s})} + \frac{\tan\psi}{\sqrt{3}} p(\boldsymbol{\sigma}) \end{aligned} \tag{3.43}$$

where, $J_2 = \frac{1}{2}\boldsymbol{s} : \boldsymbol{s};$, $\boldsymbol{s} = \boldsymbol{\sigma} - p(\boldsymbol{\sigma})\boldsymbol{I}$, $p = \frac{1}{3}\text{tr}[\boldsymbol{\sigma}]$ is the hydrostatic pressure, c is the cohesion and ψ is dilatancy angle. Note that, the non-associative flow rule is adopted here.

From the flow rule,

$$\dot{\boldsymbol{\varepsilon}}^p = \dot{\gamma}\boldsymbol{N} \tag{3.44}$$

By separating stress into sum of deviatoric and pressure, the flow vector, $\boldsymbol{N}$, can be written as,

$$\boldsymbol{N} = \frac{1}{2\sqrt{J_2(\boldsymbol{s})}}\boldsymbol{s} + \frac{\tan\psi}{3\sqrt{3}} I = \boldsymbol{N}_\text{d} + \boldsymbol{N}_\text{v} \tag{3.45}$$

This is used for the derivation of the return mapping algorithm for the Drucker-Prager model.

Drucker-Prager Model Integration Algorithm

In this model, there is only one singularity yield surface to consider at the apex and the flow vector field is symmetric about the hydrostatic axis, that makes the integration algorithm relatively simple for Drucker-Prager.

In order to solve for the $\Delta\gamma$, need to solve the sets of non-linear equations. The

general return mapping updated stress tensor for linear elastic material:

$$\boldsymbol{\sigma}_{n+1} = \boldsymbol{\sigma}_{n+1}^{\text{trial}} - \underbrace{\Delta\gamma \boldsymbol{D}^e : \boldsymbol{N}_{n+1}}_{\text{return vector}}, \tag{3.46}$$

Since the definition of the flow vector $\boldsymbol{N}_{n+1}$ in the smooth portion of the cone differs from that at the apex singularity, two possible explicit forms exist for the return-mapping algorithm. These are treated separately below

- Smooth portion of the cone:

  The incremental form of plastic strain in the equation (3.44) corresponding to the smooth portion of the cone is,

  $$\Delta\boldsymbol{\varepsilon}^p = \Delta\gamma\left(\frac{1}{2\sqrt{J_2(\boldsymbol{s})}}\boldsymbol{s}_{n+1} + \frac{\tan\psi}{3\sqrt{3}}I\right) \tag{3.47}$$

  Hence, the updated stress by using the equation above is in the form,

  $$\boldsymbol{\sigma}_{n+1} = \boldsymbol{\sigma}_{n+1}^{\text{trial}} - \Delta\gamma\left(\frac{G}{2\sqrt{J_2(\boldsymbol{s})}}\boldsymbol{s}_{n+1} + \frac{K\tan\psi}{3\sqrt{3}}I\right) \tag{3.48}$$

  The above equation can be rewrite in terms of trial by using the definition of J_2. It holds,

  $$\frac{\boldsymbol{s}_{n+1}}{J_2(\boldsymbol{s}_{n+1})} = \frac{\boldsymbol{s}_{n+1}^{\text{trial}}}{J_2(\boldsymbol{s}_{n+1}^{\text{trial}})} \tag{3.49}$$

  And, the updated stress can be written as,

  $$\boldsymbol{\sigma}_{n+1} = \boldsymbol{\sigma}_{n+1}^{\text{trial}} - \Delta\gamma\left(\frac{G}{2\sqrt{J_2(\boldsymbol{s}^{\text{trial}})}}\boldsymbol{s}_{n+1}^{\text{trial}} + \frac{K\tan\psi}{3\sqrt{3}}I\right) \tag{3.50}$$

  The updated stress can be split to deviatoric and pressure components as,

  $$\begin{aligned} \boldsymbol{s}_{n+1} &= 1 - \frac{G\Delta\gamma}{2\sqrt{J_2(\boldsymbol{s}_{n+1}^{\text{trial}})}}\boldsymbol{s}_{n+1}^{\text{trial}} \\ p_{n+1} &= p_{n+1}^{\text{trial}} - K\frac{\tan\psi}{\sqrt{3}}\Delta\gamma \end{aligned} \tag{3.51}$$

  By substituting the above equations into the discretized form of the yield

surface, the general non-linear equation for $\Delta\gamma$ is form of,

$$\tilde{\Phi} = \sqrt{J_2(\boldsymbol{s}_{n+1}^{\text{trial}})} - G\Delta\gamma + \frac{\tan\phi}{\sqrt{3}}(P_{n+1}^{\text{trial}} - K\frac{\tan\psi}{\sqrt{3}}\Delta\gamma) - \xi c(\bar{\varepsilon}_n^p + \xi\Delta\gamma) \quad (3.52)$$

where, $\xi = 1$ in this work.

After solving the above non-linear equation, the stresses will be updated inside the algorithm.

- Apex

  The consistency condition for the Apex is when the smooth return algorithm does not converge, or converge with $\sqrt{J_2(\boldsymbol{s}_{n+1}^{\text{trial}})} \leq 0$. Also, the stress correction procedure is on the axis of effective mean stress p, which relates only to the volumetric plastic strain $\Delta\varepsilon_{\text{v}}^p$. Hence the consistency equation for Apex reduces to,

$$-P_{n+1}^{\text{trial}} + K\Delta\varepsilon_{\text{v}}^p - \frac{\sqrt{3}}{\tan\psi}c(\bar{\varepsilon}_n^p + \Delta\bar{\varepsilon}^p) = 0, \quad (3.53)$$

  By using the volumetric plastic strain, $\Delta\varepsilon_{\text{v}}^p = \Delta\gamma\frac{\sqrt{3}}{\tan\psi}$ and the hardening law, $\Delta\bar{\varepsilon}^p = \Delta\gamma$, The term $\Delta\bar{\varepsilon}^p$ in the equation above can be rewrite in terms of incremental volumetric plastic strain. Therefore, we obtain the final return mapping equation for the Drucker-Prager apex from equation above as,

$$r = \Delta\varepsilon_{\text{v}}^p = K\Delta\varepsilon_{\text{v}}^p - P_{n+1}^{\text{trial}} + c(\bar{\varepsilon}_n^p + \frac{\sqrt{3}}{\tan\phi}\Delta\varepsilon_{\text{v}}^p)\frac{\sqrt{3}}{\tan\psi} = 0. \quad (3.54)$$

  After solving the above equation, we can update

$$\begin{aligned} \varepsilon_{n+1}^p &= \varepsilon_n^p + \frac{\sqrt{3}}{\tan\phi}\Delta\varepsilon_{\text{v}}^p \\ \boldsymbol{\sigma}_{n+1} &= \left(P_{n+1}^{\text{trial}} - K\varepsilon_n^p\right)\boldsymbol{I}. \end{aligned} \quad (3.55)$$

Note that, for the perfectly plastic materials, c is constant and for linearly hardening models, the hardening function reads $c(\bar{\varepsilon}^p = c_0 + \boldsymbol{H}\bar{\varepsilon}^p)$, where $\boldsymbol{H}$ denotes the hardening modulus.

The Overall Integration Algorithm

The corresponding code is summarized below that is implemented in the program HYPLAS, RVEPLUS (HYPLAS with multi-scale modeling) and ParaGeo (Explicit code) is explained in detail below.

First it is important to mention that, in this subroutine, we are passing the total trial strain, STRAT ($\varepsilon^{e\,\text{trial}}_{n+1}$) to the algorithm. In case of small strain,

$$\text{STRAT} = \text{RSTAVA} + \text{infinitesimal strain}$$

where infinitesimal strain is coming from given strain/displacement multiply by the shape function matrix and RSTAVA is the elastic engineering strain derived from Drucker-prager algorithm.
However, in case of large strain, the given trial strain, STRAT is the elastic trial eulerian logarithmic strain in equation (3.42). We can also work with total trial stress in this algorithm.
The Drucker-Prager algorithm is summarized through the following Algorithms. Recall that the purpose of the selection procedure is to ensure that the approved return mapping in this case, either the return to the smooth wall or the apex.

Algorithm 3.1: Implicit algorithm for Drucker-Prager model.

(i) Evaluate the *elastic trial state* at the initial time step;

$$\varepsilon^{e\,\text{trial}}_{n+1} := \varepsilon^{e}_{n} + \Delta\varepsilon \qquad \bar{\varepsilon}^{p\,\text{trial}}_{n+1} := \bar{\varepsilon}^{p}_{n}$$
$$\boldsymbol{s}^{e\,\text{trial}}_{n+1} := 2G\varepsilon^{e\,\text{trial}}_{n+1} \qquad p^{\text{trial}}_{n+1} := K\varepsilon^{e\,\text{trial}}_{\text{v}\,n+1}$$

(ii) Check plastic admissibility

IF $\sqrt{J_2(\boldsymbol{s}^{\text{trial}}_{n+1})} + \frac{\tan\phi}{\sqrt{3}} p^{\text{trial}}_{n+1} - c(\bar{\varepsilon}^{p\,\text{trial}}_{n+1}) \leq 0$

THEN stay in elastic state and EXIT

(iii) Check the smooth portion, GOTO Algorithm 3.2

(iv) See if smooth part is valid

$$\text{IF}\sqrt{J_2(\boldsymbol{s}^{\text{trial}}_{n+1})} - G\Delta\gamma \geq 0$$

THEN, Update the strain from (vi)

(v) IFNOT, return to apex - GOTO Algorithm 3.3

(vi) Update elastic strain

$$\varepsilon^{e}_{n+1} := \frac{1}{2G}\boldsymbol{s}_{n+1} + \frac{p_{n+1}}{3K}\boldsymbol{I}$$

(vii) EXIT

Algorithm 3.2: Implicit algorithm to the smooth part.

(i) Solving for $\Delta\gamma$: Set initial guess

$$\Delta\gamma := 0, \quad \bar{\varepsilon}^p_{n+1} := \bar{\varepsilon}^p_n$$

(ii) Start Newton-Raphson iteration for $\Delta\gamma$

$$H := \left.\frac{\mathrm{d}c}{\mathrm{d}\bar{\varepsilon}^p}\right|_{\bar{\varepsilon}^p_{n+1}} \qquad \text{(hardening slope)}$$

$$d := \frac{\mathrm{d}\tilde{\Phi}}{\mathrm{d}\Delta\gamma} = -G - K\frac{\tan(\phi)}{\sqrt{3}}\frac{\tan(\psi)}{\sqrt{3}} - H \qquad \text{(derivtive form of residual)}$$

$$\Delta\gamma := \Delta\gamma - \frac{\tilde{\Phi}}{d} \qquad \text{(update value)}$$

(iii) Check if Newton-Raphson iteration convergence

$$\bar{\varepsilon}^p_{n+1} := \bar{\varepsilon}^p_n + \Delta\gamma$$

$$\tilde{\Phi} := \sqrt{J_2(\boldsymbol{s}^{\text{trial}}_{n+1})} - G\Delta\gamma + \frac{\tan\phi}{\sqrt{3}}(P^{\text{trial}} - K\frac{\tan\psi}{\sqrt{3}}\Delta\gamma) - c(\bar{\varepsilon}^p_{n+1})$$

IF $|\tilde{\Phi}| \leq \epsilon_{\text{tol}}$ THEN update

$$\boldsymbol{s}_{n+1} := 1 - \frac{G\Delta\gamma}{2\sqrt{J_2(\boldsymbol{s}^{\text{trial}})}}\,\boldsymbol{s}^{\text{trial}}_{n+1}$$

$$p_{n+} := p^{\text{trial}}_{n+} - K\frac{\tan\psi}{\sqrt{3}}\Delta\gamma$$

(iv) GOTO Algorithm 3.1 and start at (ii)

Algorithm 3.3: Implicit algorithm to apex.

(i) Solving for $\Delta\varepsilon_{\mathrm{v}}^{p}$: Set initial guess

$$\Delta\varepsilon_{\mathrm{v}}^{p} := 0, \quad \bar{\varepsilon}_{n+1}^{p} := \bar{\varepsilon}_{n}^{p}$$

(ii) Start Newton-Raphson iteration for $\Delta\varepsilon_{\mathrm{v}}^{p}$

$$H := \left.\frac{\mathrm{d}c}{\mathrm{d}\bar{\varepsilon}^{p}}\right|_{\bar{\varepsilon}_{n+1}^{p}} \qquad \text{(hardening slope)}$$

$$d := \frac{\mathrm{d}r}{\mathrm{d}\Delta\varepsilon_{\mathrm{v}}^{p}} = \frac{\sqrt{3}}{\tan(\phi)}\frac{\sqrt{3}}{\tan(\psi)}H + K \qquad \text{(derivtive form of residual)}$$

$$\Delta\varepsilon_{\mathrm{v}}^{p} := \Delta\varepsilon_{\mathrm{v}}^{p} - \frac{r}{d} \qquad \text{(update value } \Delta\varepsilon_{v}^{p}\text{)}$$

(iii) Check if Newton-Raphson iteration convergence

$$\bar{\varepsilon}_{n+1}^{p} := \bar{\varepsilon}_{n}^{p} + \Delta\varepsilon_{\mathrm{v}}^{p}$$

$$p_{n+1} := p_{n+1}^{\mathrm{trial}} - K\Delta\varepsilon_{\mathrm{v}}^{p}$$

$$r := \frac{\sqrt{3}}{\tan(\psi)}c\,(\bar{\varepsilon}_{n+1}^{p}) - p_{n+1}$$

IF $|r| \leq \epsilon_{\mathrm{tol}}$ THEN update

$$\boldsymbol{\sigma}_{n+1} := p_{n+1}\boldsymbol{I}$$

(iv) GOTO Algorithm 3.1 and start at (ii)

Consistent Tangent Modulus for Implicit Code

Consistent tangent is coming from the derivative of the updated stresses (either from the smooth portion or apex of the cone) through the above algorithm.

- Smooth part of the cone tangent: By differentiating the updated deviatoric stress with respect to the elastic deviatoric trial strain. It yields

$$\begin{aligned}\mathrm{d}\boldsymbol{s}_{n+1} = 2G\Bigg[&\left(1 - \frac{\Delta\gamma}{\sqrt{2}||\boldsymbol{\varepsilon}_{\mathrm{d}\,n+1}^{e\,\mathrm{trial}}||}\right)\mathrm{d}\boldsymbol{\varepsilon}_{\mathrm{d}\,n+1}^{e\,\mathrm{trial}} \\ &+ \frac{\Delta\gamma}{\sqrt{2}\boldsymbol{\varepsilon}_{\mathrm{d}\,n+1}^{e\,\mathrm{trial}}}\boldsymbol{D}\otimes\boldsymbol{D} : \mathrm{d}\boldsymbol{\varepsilon}_{\mathrm{d}\,n+1}^{e\,\mathrm{trial}} - \frac{1}{\sqrt{2}}\mathrm{d}\Delta\gamma\boldsymbol{D}\Bigg],\end{aligned} \tag{3.56}$$

where, the second order tensor, $\boldsymbol{D}$ is:

$$\boldsymbol{D} \equiv \frac{\boldsymbol{\varepsilon}_{\mathrm{d}\,n+1}^{e\,\mathrm{trial}}}{||\boldsymbol{\varepsilon}_{\mathrm{d}\,n+1}^{e\,\mathrm{trial}}||}. \tag{3.57}$$

And, for the hydrostatic pressure, taking the derivation of the updated pressure with respect to the elastic trial volumetric strain. It gives,

$$\mathrm{d}p_{n+1} = K\left(\mathrm{d}\varepsilon_{\mathrm{v}\,n+1}^{e\,\mathrm{trial}} - \frac{\sqrt{3}}{\tan(\psi)}\mathrm{d}\Delta\gamma\right). \tag{3.58}$$

By taking the derivative of equation (3.52) with respect to the trial strain, the expression relating, $\mathrm{d}\Delta\gamma$ can be obtained as,

$$\begin{aligned}\mathrm{d}\tilde{\Phi} = \sqrt{2}G\boldsymbol{D} : \mathrm{d}\varepsilon_{\mathrm{d}\,n+1}^{e\,\mathrm{trial}} + K\frac{\tan(\phi)}{\sqrt{3}}\mathrm{d}\varepsilon_{\mathrm{v}\,n+1}^{e\,\mathrm{trial}} \\ - \left(G + K\frac{\tan(\phi)}{\sqrt{3}}\frac{\tan(\psi)}{\sqrt{3}} + H\right)\mathrm{d}\Delta\gamma = 0,\end{aligned} \tag{3.59}$$

Hence, $\mathrm{d}\Delta\gamma$ can be written in the form,

$$\mathrm{d}\Delta\gamma = \frac{1}{G + K\frac{\tan(\phi)}{\sqrt{3}}\frac{\tan(\psi)}{\sqrt{3}} + H}(\sqrt{2}G\boldsymbol{D} : \mathrm{d}\varepsilon_{\mathrm{d}\,n+1}^{e\,\mathrm{trial}} + K\frac{\tan(\phi)}{\sqrt{3}}\mathrm{d}\varepsilon_{\mathrm{v}\,n+1}^{e\,\mathrm{trial}}) \tag{3.60}$$

Finally, using the expression $\mathrm{d}\Delta\gamma$ in both equations (3.56) and (3.58), and use of the identity

$$\boldsymbol{D}^{ep} \equiv \frac{\mathrm{d}\boldsymbol{\sigma}_{n+1}}{\mathrm{d}\varepsilon_{n+1}^{e\,\mathrm{trial}}} = \frac{\mathrm{d}\boldsymbol{s}_{n+1}}{\mathrm{d}\varepsilon_{n+1}^{e\,\mathrm{trial}}} + \boldsymbol{I} \otimes \frac{\mathrm{d}p_{n+1}}{\mathrm{d}\varepsilon_{n+1}^{e\,\mathrm{trial}}}, \tag{3.61}$$

The expression which is coded in the HYPLAS code for the elasto-plastic tangent modulus is obtained after some straightforward manipulations as

$$\begin{aligned}\boldsymbol{D}^{ep} = 2G\left(1 - \frac{\Delta\gamma}{\sqrt{2}||\varepsilon_{\mathrm{d}\,n+1}^{e\,\mathrm{trial}}||}\right)|_{\mathrm{d}} + 2G\left(1 - \frac{\Delta\gamma}{\sqrt{2}||\varepsilon_{\mathrm{d}\,n+1}^{e\,\mathrm{trial}}||}\right)\boldsymbol{D}\otimes\boldsymbol{D} - \sqrt{2}GAK \\ (\frac{\tan(\phi)}{\sqrt{3}})\boldsymbol{D}\otimes\boldsymbol{D} + \frac{\tan(\phi)}{\sqrt{3}}\boldsymbol{I}\otimes\boldsymbol{D}) + K(1 - K\frac{\tan(\phi)}{\sqrt{3}}\frac{\tan(\psi)}{\sqrt{3}}A)\boldsymbol{I}\otimes\boldsymbol{I}\end{aligned} \tag{3.62}$$

where $|_{\mathrm{d}}$ is the deviatoric projection tensor and term A is described as,

$$A = \frac{1}{G + (K\frac{\tan(\psi)}{\sqrt{3}}\frac{\tan(\phi)}{\sqrt{3}}) + H} \tag{3.63}$$

- Apex tangent: As at the apex there is only hydrostatic (pressure) stress. Therefore, the equation (3.62) for associated elasto-plastic tangent modulus

reduces to,

$$\boldsymbol{D}^{ep} \equiv \frac{\mathrm{d}\boldsymbol{\sigma}_{n+1}}{\mathrm{d}\boldsymbol{\varepsilon}^{e\,\mathrm{trial}}_{n+1}} = \boldsymbol{I} \otimes \frac{\mathrm{d}p_{n+1}}{\mathrm{d}\boldsymbol{\varepsilon}^{e\,\mathrm{trial}}_{n+1}}, \tag{3.64}$$

where, $\mathrm{d}p_{n+1} = K\boldsymbol{I} : \mathrm{d}\boldsymbol{\varepsilon}^{e\,\mathrm{trial}}_{n+1} - K\mathrm{d}\Delta\varepsilon^{p}_{\mathrm{v}}$.

rewriting the $\mathrm{d}\varepsilon^{p}_{\mathrm{v}}$ in terms of the elastic trial strain by taking the derivative of the residual equation (3.54) and substituting it in the equation (3.64). The derivative form of the tangent operator consistent with the apex return mapping is in the form,

$$\boldsymbol{D}^{ep} = \boldsymbol{I} \otimes \frac{K\boldsymbol{I} : \mathrm{d}\boldsymbol{\varepsilon}^{e\,\mathrm{trial}}_{n+1} - K\left[\left(\dfrac{K}{K + \frac{\sqrt{3}}{\tan(\psi)}\frac{\sqrt{3}}{\tan(\phi)}H}\right)\boldsymbol{I} : \mathrm{d}\boldsymbol{\varepsilon}^{e\,\mathrm{trial}}_{n+1}\right]}{\mathrm{d}\boldsymbol{\varepsilon}^{e\,\mathrm{trial}}_{n+1}}, \tag{3.65}$$

Hence, the tangent operator consistent with the apex return mapping is expressed as,

$$\boldsymbol{D}^{ep} = K\left(1 - \frac{K}{K + \frac{\sqrt{3}}{\tan(\psi)}\frac{\sqrt{3}}{\tan(\phi)})H}\right)\boldsymbol{I} \otimes \boldsymbol{I}. \tag{3.66}$$

3.2.2 The SR4 Model

The implementation of the soft rock, SR4 model, which is a new constitutive model and proposed by [52] is described. The model is combination of the SR3 and Cam Clay models. The SR3 surface is to describe the shear response and an elliptical cap to represent the compaction response. The flow surface can have a different shape in the $p - q$ plane to the yield surface. That is to say, the critical state line may take different slope than the peak strength line and they are independent. This important as

1 The true frictional resistance of the sand and the shape of the cap can be represented simultaneously. As, the shape of the yield surface and flow potentials are not restricted.

2 Taking the conditions that cause static liquefaction are considered within the model [62].

The detailed description of the soft rock constitutive models is provided in [63] The SR4 is a three-invariant rate-independent poro-elastic-plastic critical state constitutive model with non-associative plasticity but, in this work we use associative plasticity only.

The yield surface delimits the domain of stress states that produces elastic and elastic-plastic strains. Stress paths moving inside the elastic domain produce elastic deformation whereas, stress paths that reach the yield surface may produce elastic-plastic deformation. It is defined in the $p - q$ plane with two functions that intersect at the point of maximum deviatoric stress. The shear side is defined using the SR3 surface whereas the compression side is defined by the elliptical function of the standard Cam clay model as illustrated in Figure 3.2.

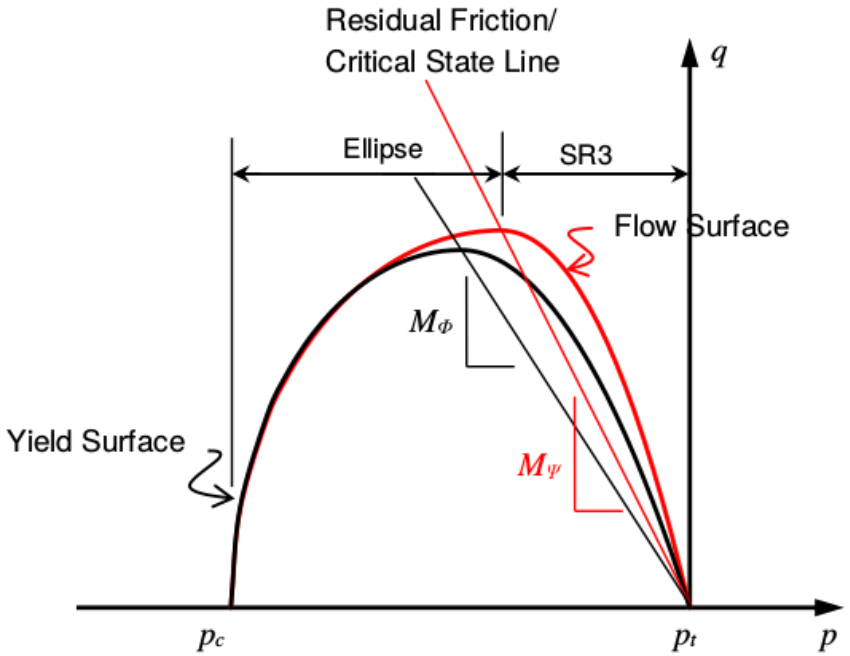

Figure 3.2: SR4 representation in p-q plane.

Shear Yield Surface

The shear yield function intersects the hydrostatic axis in tension and is defined as:

$$\Phi(\boldsymbol{\sigma}, \varepsilon_{\mathrm{v}}^{p}) = g(\theta, p)q + (p - p_t)\tan\beta\left(\frac{p - p_c}{p_t - p_c}\right)^{\frac{1}{n}} \tag{3.67}$$

where p_t is the tensile intercept of the yield surface with the hydrostatic axis, p_c is the pre-consolidation pressure or compressive intercept of the yield surface with the hydrostatic axis, $\varepsilon_{\mathrm{v}}^{p}$ is the plastic volumetric strain, β and n are material constants which define the shape of the yield surface in the $p - q$ plane, θ is the lode angle. $g(\theta, p)$ is a function that controls the shape of the yield surface in the deviatoric plane (plane normal to hydrostatic axis.) and $p_{\Phi\mathrm{crit}}$ is the effective mean stress at q_{crit} value that is given as,

$$p_{\Phi\mathrm{crit}} = \frac{1}{(n+1)}(p_t + np_c) \tag{3.68}$$

The deviatoric stress is implemented in explicit ParaGeo code as,

$$q = \sqrt{3\boldsymbol{J}} = \sqrt{\frac{3}{2}\boldsymbol{s} : \boldsymbol{s}} \tag{3.69}$$

Cap Yield Surface

The cap yield surface is defined as

$$\Phi_{\text{cap}} = (gq)^2 - M_\Phi^2 p_{\Phi\text{crit}}^2 \left[1 - \frac{(p_{\Phi\text{crit}} - p)^2}{((p_{\Phi\text{crit}} - p_c)^2}\right] = 0 \tag{3.70}$$

where,

$$\boldsymbol{M}_\Phi = \frac{q_{\Phi\text{crit}}}{p_{\Phi\text{crit}}} = -\frac{1}{g p_{\Phi\text{crit}}}(p_{\Phi\text{crit}} - p_t)\tan\beta\left(\frac{p_{\Phi\text{crit}} - p_c}{p_t - p_c}\right)^{1/n} \tag{3.71}$$

Yield Surface Shape in Deviatoric Plane

The expression for the deviatoric correction plane is used here is as,

$$g(\theta, p) = \left[\frac{1}{1 - \beta^\pi(p)}(1 + \beta^\pi(p)\sin(3\theta))\right]^{N^\pi} \tag{3.72}$$

where $N^\pi$is a deviatoric plane shape material constant and $\beta^\pi(p)$ is a function defined as

$$\beta^\pi(p) = \beta_0^\pi \exp\left(\beta_1^\pi p \frac{p_{co}}{p_c}\right) \tag{3.73}$$

where β_0^π and $\beta_1^\pi$are material constants and p_{co} is the initial pre-consolidation pressure (corresponding to uncompressed and undamaged material).

Flow Rule

The non-associative plastic strain rate for the plastic flow is defined as,

$$\dot{\varepsilon}^p = \dot{\gamma}\frac{\partial \Psi}{\partial \boldsymbol{\sigma}} = \dot{\gamma}\boldsymbol{N} \tag{3.74}$$

And the loading/unloading criterion like other material models is

$$\Phi \leq 0, \quad \dot{\gamma} \geq 0, \quad \dot{\gamma}\Phi = 0. \tag{3.75}$$

where, the flow vector, $\boldsymbol{N}$, can be written in terms of the shear and cap flow surfaces. The flow surfaces for the shear and cap surfaces are shown in the following,

- Shear flow surface:

$$\Psi_{\text{shear}} = g^{\text{trial}} q + (p - p_t)\tan\psi \left(\frac{p - p_c}{p_t - p_c} \right)^{1/m} \quad p^{\text{trial}} \geq p_{\Psi\text{crit}} \tag{3.76}$$

  where, m and ψ are material parameters that describes the shape of the plastic flow surface. Note that, ψ is not the dilation angle, as the dilation angle is dependent on the position of the stress state relative to the yield surface. This plastic potential therefore intercepts the hydrostatic axis at the same point as the yield surface but is generally specified with $\psi < \phi$ and

$$p_{\Psi\text{crit}} = \frac{1}{(m+1)}(p_t + m p_c) \tag{3.77}$$

  Hence, the shear flow vector, $\boldsymbol{N}_{\text{shr}}$ is defined as,

$$\boldsymbol{N}_{\text{shr}} = \frac{\partial \Psi_{\text{shr}}}{\partial q}\frac{\partial q}{\partial \boldsymbol{\sigma}} + \frac{1}{3}\boldsymbol{m}\frac{\partial \Psi_{\text{shr}}}{\partial p} \tag{3.78}$$

  where, $\boldsymbol{m} = [1\,1\,1\,0\,0\,0]^T$ and,

$$\begin{aligned} \frac{\partial q}{\partial \boldsymbol{\sigma}} &= \frac{3}{2q}[s_{xx}, s_{yy}, s_{zz}, 2s_{xy}, 2s_{yz}, 2s_{zx}]^T \\ \frac{\partial \Psi_{\text{shr}}}{\partial q} &= g \\ \frac{\partial \Psi_{\text{shr}}}{\partial p} &= \left[\frac{1}{(p - p_t)} + \frac{1}{n(p - p_c)} \right] \Psi_{\text{shr}} \end{aligned} \tag{3.79}$$

- Cap flow surface:

  The flow rule is given by,

$$\Psi_{\text{cap}} = (gq)^2 - M_\Psi^2 p_{\Psi\text{crit}}^2 \left[1 - \frac{(p_{\Psi\text{crit}} - p)^2}{((p_{\Psi\text{crit}} - p_c)^2} \right] = 0 \tag{3.80}$$

  Also, similar to the shear flow vector, the cap flow vector is as,

$$\boldsymbol{N}_{\text{cap}} = \frac{\partial \Psi_{\text{cap}}}{\partial q}\frac{\partial q}{\partial \boldsymbol{\sigma}} + \frac{1}{3}\boldsymbol{m}\frac{\partial \Psi_{\text{cap}}}{\partial p} \tag{3.81}$$

The derivatives are defined as,

$$\begin{aligned}\frac{\partial \Psi_{\text{cap}}}{\partial q} &= 2g^2 q \\ \frac{\partial \Psi_{\text{cap}}}{\partial p} &= -2M_\Psi^2 p_{\Psi\text{crit}}^2 \frac{(p_{\Psi\text{crit}} - p)}{(p_{\Psi\text{crit}} - p_c)^2}\end{aligned} \tag{3.82}$$

Stress Update

The stress update in $p - q$ space is

$$\begin{aligned}q_{n+1} &= \sqrt{\frac{3}{2}\boldsymbol{s}_{n+1} : \boldsymbol{s}_{n+1}} = \sqrt{\frac{3}{2}(\boldsymbol{s}^{\text{trial}} - 2G\Delta\boldsymbol{\varepsilon}_{\text{d}}^p) : (\boldsymbol{s}^{\text{trial}} - 2G\Delta\boldsymbol{\varepsilon}_{\text{d}}^p))} \\ &= \sqrt{\frac{3}{2}(\boldsymbol{s}^{\text{trial}}) : (\boldsymbol{s}^{\text{trial}})} - 2G\sqrt{\frac{3}{2}\Delta\boldsymbol{\varepsilon}_{\text{d}}^p : \boldsymbol{\varepsilon}_{\text{d}}^p} \\ &= q^{\text{trial}} - 3G\Delta\gamma\frac{\partial \Psi}{\partial q}\end{aligned} \tag{3.83}$$

Therefore, according to the specific flow potentials,

$$\begin{aligned}q_{n+1} &= q^{\text{trial}} - 3Gg\Delta\gamma \quad \text{Shear} \\ q_{n+1} &= q^{\text{trial}} - 6Gg^2 q\Delta\gamma \quad \text{Cap}\end{aligned} \tag{3.84}$$

and the pressure p is

$$p_{n+1} = p^{\text{trial}} - K\Delta\varepsilon_v^p \tag{3.85}$$

In order to update the stresses, there are four equations to solve for four unknowns i.e. two stress components (p_{n+1}, q_{n+1}), the volumetric plastic strain and plastic multiplier, ε_{v}^p and $\Delta\gamma$ respectively.

$$\begin{aligned}E_1 &= p_{n+1} - p^{\text{trial}} + K\Delta\varepsilon\text{v}^p \\ E_2 &= \Phi(p,\, q,\, \Delta\gamma,\, \Delta\varepsilon_{\text{v}}^p) \\ E_3 &= \Delta\varepsilon_{\text{v}}^p - 3G\Delta\gamma\Delta\gamma\frac{\partial \Psi}{\partial p} \\ E_4 &= q_{n+1} - q^{\text{trial}} + 3G\Delta\gamma\frac{\partial \Psi}{\partial q}\end{aligned} \tag{3.86}$$

The backward Euler integration is applied using Newton-Raphson iteration equation with equation above,

$$\begin{bmatrix} \frac{\partial E_1}{\partial p} & \frac{\partial E_1}{\partial \Delta\gamma} & \frac{\partial E_1}{\partial \Delta\varepsilon_{\mathrm{v}}^p} & \frac{\partial E_1}{\partial q} \\ \frac{\partial E_2}{\partial p} & \frac{\partial E_2}{\partial \Delta\gamma} & \frac{\partial E_2}{\partial \Delta\varepsilon_{\mathrm{v}}^p} & \frac{\partial E_2}{\partial q} \\ \frac{\partial E_3}{\partial p} & \frac{\partial E_3}{\partial \Delta\gamma} & \frac{\partial E_3}{\partial \Delta\varepsilon_{\mathrm{v}}^p} & \frac{\partial E_3}{\partial q} \\ \frac{\partial E_4}{\partial p} & \frac{\partial E_4}{\partial \Delta\gamma} & \frac{\partial E_4}{\partial \Delta\varepsilon_{\mathrm{v}}^p} & \frac{\partial E_4}{\partial q} \end{bmatrix} = \begin{bmatrix} 1 & 0 & K & 0 \\ \frac{\partial \Phi}{\partial p} & \frac{\partial \Phi}{\partial \Delta\gamma} & \frac{\partial \Phi}{\partial \Delta\varepsilon_{\mathrm{v}}^p} & \frac{\partial \Phi}{\partial q} \\ -\Delta\gamma \frac{\partial^2 \Psi}{\partial p^2} & -\frac{\partial \Psi}{\partial p} & 1 - \Delta\gamma \frac{\partial}{\partial \Delta\varepsilon_{\mathrm{v}}^p}\left[\frac{\partial \Psi}{\partial p}\right] & 0 \\ 0 & 3G\frac{\partial \Psi}{\partial q} & 0 & 1 + 3G\Delta\gamma \frac{\partial^2 \Psi}{\partial^2 q} \end{bmatrix}$$

The derivative of the equations in the above matrix are either for the shear or cap surface according to the appropriate one.

when $p^{\mathrm{trial}} \leq p_{\Psi_{\mathrm{crit}}}$ then the flow potential will always be the cap, while the yield surface may be either the shear surface or the cap. Further, during the stress update the stress point move between the shear and cap yield surfaces. when $p^{\mathrm{trial}} > p_{\Psi_{\mathrm{crit}}}$ the stress point will always lies on the shear yield surface and the shear flow potential will always be active.

Tension Apex Return

If $p_t = 0$, the tension apex return stress and pressure can be updated as

$$\begin{aligned} \boldsymbol{s}_{n+1} &= \boldsymbol{s}^{\mathrm{trial}} - 2G\Delta\gamma_{\mathrm{d}}\boldsymbol{s}^{\mathrm{trial}} \\ p_{n+1} &= p^{\mathrm{trial}} - K\Delta\varepsilon_{\mathrm{v}}^p \end{aligned} \tag{3.87}$$

And, the $\boldsymbol{s}_{n+1} = 0$ at apex so that $\Delta\gamma_{\mathrm{d}} = \frac{1}{2G}$. Therefore, the yielding function is define as,

$$\boldsymbol{F} = p^{\mathrm{trial}} - K\Delta\varepsilon_{\mathrm{v}}^p - p_t(\varepsilon_{\mathrm{v}}^p) = 0 \tag{3.88}$$

Applying Newton-Raphson iteration scheme

$$\frac{\partial \boldsymbol{F}}{\partial \Delta\varepsilon_{\mathrm{v}}^p}\mathrm{d}(\Delta\varepsilon_{\mathrm{v}}^p) = -\boldsymbol{F} \tag{3.89}$$

Hence,

$$\mathrm{d}(\Delta\varepsilon_{\mathrm{v}}^p) = \frac{\boldsymbol{F}}{H + K} \tag{3.90}$$

Chapter 4

Non-Linear Finite Element Solution

Finite element is a numerical approximation that is suitable to the solution of certain potential differential equations. It has been powerful method in engineering problems and been implemented in modern software to simulate their designs.
In this chapter, we are introducing the summary of the implicit and explicit Finite Element method (FE) to non-linear solid mechanics. The implicit finite Element (FE) numerical solution will be used to solve the RVE problems later in this work. The FE approximation (discretization) of the nonlinear BVP which is solved by Newton-Raphson (N-R) iterative algorithm is provided. Next, we introduce the explicit solver followed by the stress integration. Finally, the element methodology that is used in this work is described.

4.1 Large Strain Finite Element Approximation: Implicit solver

The summary of the non-linear explicit Finite Element method which is the solution to the static problems is explained in the following. This method relies on the discretization of the virtual work by means of finite element bases interpolation or shape functions whose parameters are the nodal displacements. Next, the solution of the linear discrete equations by the Newton-Raphson method is described. The formulations presented in this section are standard and can be found in [54; 55; 64; 65].

4.1.1 Finite Element Discretization

Finite Element method for the numerical solution explained in section 2.2.3, equations (2.25) and (2.28) is, by discretization the reference configuration Ω to Ω^h and for both spaces $\mathscr{K}$ and $\mathscr{V}$ to subsets $\mathscr{K}^h$ and $\mathscr{V}^h$.

Let us define the element, e with nodal coordinate $\boldsymbol{x}_i$ and the interpolation function, $\boldsymbol{N}_i^{(e)}$ associated with each node i. The finite element interpolation of the field y^h over the element domain Ω^e can be expressed as

$$y^h \equiv \sum_{i=1}^{n} \boldsymbol{N}_i^{(e)} y_i, \tag{4.1}$$

where, $y_i \equiv y(\boldsymbol{x}_i)$ and n is the number of nodes per element.

In order to discretize the virtual work, with the introduction of the above interpolation, the functional sets $\mathscr{K}$ and $\mathscr{V}$ are replaced by the following finite-dimensional subsets as,

$$\begin{aligned} \mathscr{K}^h &= \left\{ \boldsymbol{u}^h = \sum_{i=1}^{n} \boldsymbol{N}_i^{(e)} \boldsymbol{u}_i \right\} \\ \mathscr{V}^h &= \left\{ \boldsymbol{\eta}^h = \sum_{i=1}^{n} \boldsymbol{N}_i^{(e)} \boldsymbol{\eta}_i \right\} \end{aligned} \tag{4.2}$$

respectively. Also the displacement vector, virtual displacement $\boldsymbol{\eta}$ and its gradient are in the form,

$$\begin{aligned} \boldsymbol{u}^h &= \sum_{i=1}^{n} \boldsymbol{N}_i^{(e)} \boldsymbol{u}_i \\ \boldsymbol{\eta}^h &= \sum_{i=1}^{n} \boldsymbol{N}_i^{(e)} \boldsymbol{\eta}_i \text{ and } \nabla \boldsymbol{\eta}^h = \sum_{i=1}^{n} \boldsymbol{G}_i^{(e)} \boldsymbol{\eta}_i, \end{aligned} \tag{4.3}$$

With the above introduction in equation (2.25), the discretized virtual work expression gives,

$$\begin{aligned} \delta W^{e,h} = \Bigg\{ & \underbrace{\int_{\Omega^e} \boldsymbol{G}_i^{(e)T} \boldsymbol{P} \mathrm{d}V}_{\boldsymbol{f}_{\text{int}}^{eh}} - \\ & \overbrace{\int_{\partial\Omega^e} \boldsymbol{N}_i^{(e)T} \boldsymbol{t} \mathrm{d}A - \int_{\Omega^e} \boldsymbol{N}_i^{(e)T} \boldsymbol{f} \mathrm{d}V}^{\boldsymbol{f}_{ext}^{eh}} \Bigg\} \boldsymbol{\eta}_i = \boldsymbol{0} \quad \forall \boldsymbol{\eta} \in \mathscr{V}^h \end{aligned} \tag{4.4}$$

where, $\boldsymbol{G}_i^{(e)}$ is the associated local non-symmetric gradient matrix at node i and

$\boldsymbol{f}_{\text{int}}^{e\,h}$ and $\boldsymbol{f}_{\text{ext}}^{e\,h}$ are the internal and external nodal force vectors of the element respectively.

The Gaussian quadratures is used to evaluate the exact integral of the element force vector. By taking the integration domain as Γ, the Gaussian quadratures approximation reads,

$$\int_{\Gamma} f(\boldsymbol{\xi})\, d\boldsymbol{\xi} \approx \sum_{i}^{n_g} \omega_i\, f(\boldsymbol{\xi}_i) \tag{4.5}$$

where, n_g is the number of Gauss points and $\boldsymbol{\xi}$ is the coordinates of the Gauss points with corresponding weights, ω_i over the integration domain.

The Gauss quadrature expression for approximation of the integral of a function over domain Ω^e is in the form,

$$\int_{\Omega^e} g(\boldsymbol{x})\, d\boldsymbol{x} = \int_{\Gamma} g(\boldsymbol{x}(\boldsymbol{\xi}))\, j(\boldsymbol{\xi})\, \mathrm{d}\boldsymbol{\xi} \approx \sum_{i}^{n_g} \omega_i\, g_i\, j_i. \tag{4.6}$$

where, $j(\boldsymbol{\xi}) = \det\left[\dfrac{\partial \boldsymbol{x}}{\partial \boldsymbol{\xi}}\right]$ is the determinant of the derivative of the shape functions with respect to $\boldsymbol{\xi}$ for each Gauss point (determinant of Jacobian). Note that, exactly same procedure applies to the boundary, $\partial\Omega^e$, of an element. Therefore, by applying the Gaussian quadratures for integrals over an element, the element force arrays are obtained as,

$$\begin{aligned} \boldsymbol{f}_{\text{int}}^{e\,h} &= \sum_{i=1}^{n} \omega_i\, \boldsymbol{G}_i^{(e)T}\, \boldsymbol{P}\, j_i \\ \boldsymbol{f}_{\text{ext}}^{e\,h} &= \sum_{i=1}^{n} \omega_i\, \boldsymbol{N}_i^{(e)T} \boldsymbol{t}\, j_i + \sum_{i=1}^{n} \omega_i\, \boldsymbol{N}_i^{(e)T} \boldsymbol{f}\, j_i \end{aligned} \tag{4.7}$$

In order to get the global force vectors over the entire domain with a *mesh* of finite element, assembling the nodal forces for all the element is expressed as,

$$\boldsymbol{f}^{\text{int}} = \mathbf{A}_i^N(\boldsymbol{f}_{int\,,i}^{e\,h}) \tag{4.8}$$

where, $\mathbf{A}$ is the FE assembly operator, is obtained the sum of the element force vectors for all elements sharing the particular global node.

By applying the above expressions to the equations (2.28) and (2.29), the non-linear

incremental finite element equation is expressed over the entire domain as,

$$\int_{\Omega^h} \boldsymbol{G}^T \boldsymbol{P}^{n+1}(\boldsymbol{F}^{n+1}, \boldsymbol{\alpha}^n)\,\mathrm{d}V - \int_{\partial\Omega^h} \boldsymbol{N}^T \boldsymbol{t}^{n+1}\,\mathrm{d}A - \int_{\Omega^h} \boldsymbol{N}^T \boldsymbol{f}^{n+1}\,\mathrm{d}V = \boldsymbol{0} \quad \forall \boldsymbol{\eta} \in \mathscr{V}^h \tag{4.9}$$

4.1.2 The Newton–Raphson Scheme. Linearization

The solution of the non-linear expression above can be obtained by an iterative procedure. One of the iterative method is Newton-Raphson which is the most attractive solution. Due to its quadratic convergence. This method requires the linearized form of the equation (4.9). The following procedures describe the linearized form of the virtual work in the direction of $\delta\boldsymbol{u}$ briefly. The linearized problem consists in solving displacement for a generic function y such that

$$L(\delta\boldsymbol{u}, \boldsymbol{\eta}) \equiv y(\boldsymbol{u}^*, \boldsymbol{\eta}) + Dy(\boldsymbol{u}^*, \boldsymbol{\eta})[\delta\boldsymbol{u}] = 0\,, \tag{4.10}$$

where L is the linearized form of the function y and

$$Dy(\boldsymbol{u}^*, \boldsymbol{\eta})[\delta\boldsymbol{u}] = \left.\frac{\mathrm{d}}{\mathrm{d}\epsilon}\right|_{\epsilon_0} y(\boldsymbol{u}^* + \epsilon\delta\boldsymbol{u}, \boldsymbol{\eta}), \tag{4.11}$$

is the directional derivative of the function, y at arbitrary argument $\boldsymbol{u}^*$ in the direction of unknown displacement, $\delta\boldsymbol{u}$. Therefore, with the above at hand, and having $\boldsymbol{P}$ in the virtual work expressed in equation (2.25), in terms of a function of displacement field through deformation gradient, equation (2.3), we arrive at the expression for the linearized virtual work as,

$$\begin{aligned} D\delta W[\boldsymbol{u}^*, \boldsymbol{\eta}][\delta\boldsymbol{u}] &= \left.\frac{\mathrm{d}}{\mathrm{d}\epsilon}\right|_{\epsilon_0} \int_\Omega (\boldsymbol{P}(\boldsymbol{F}) : \nabla\boldsymbol{\eta})\,\mathrm{d}V - \int_\Omega \boldsymbol{t}.\boldsymbol{\eta}\,\mathrm{d}A - \int_\Omega \boldsymbol{f}.\boldsymbol{\eta}\,\mathrm{d}V, \\ &\quad \text{and} \quad \boldsymbol{F} = \boldsymbol{I} + \nabla(\boldsymbol{u}^* + \epsilon\delta\boldsymbol{u}) \\ &\Rightarrow D\delta W[\boldsymbol{u}^*, \boldsymbol{\eta}][\delta\boldsymbol{u}] = \left.\frac{\mathrm{d}}{\mathrm{d}\epsilon}\right|_{\epsilon_0} \int_\Omega (\boldsymbol{P}(\boldsymbol{F}) : \nabla\boldsymbol{\eta})\,\mathrm{d}V \\ &= \int_\Omega \frac{\partial \boldsymbol{P}}{\partial \boldsymbol{F}} : \nabla\delta\boldsymbol{u}\nabla\boldsymbol{\eta})\,\mathrm{d}V \end{aligned} \tag{4.12}$$

where, $\dfrac{\partial \boldsymbol{P}}{\partial \boldsymbol{F}} = \mathbf{A}$ is the material tangent modulus. Hence, the final expression of the linearized virtual work in large strain is in the form,

$$\int_{\Omega} \mathbf{A} : \nabla \delta \boldsymbol{u} : \nabla \boldsymbol{\eta} \, \mathrm{d}V = -\int_{\Omega} \boldsymbol{P} : \nabla \boldsymbol{\eta} \, \mathrm{d}V + \int_{\Omega} \boldsymbol{t}.\boldsymbol{\eta} \, \mathrm{d}A + \int_{\Omega} \boldsymbol{f} \boldsymbol{\eta} \, \mathrm{d}V \tag{4.13}$$

By applying the FE discretization to the equation above, the Newton-Raphson iterative method can be applied to solve for the unknown displacement.

Newton-Raphson Solution

The finite element discretization of the linearized virtual work above is in the form,

$$\begin{aligned} \left\{ \int_{\Omega^h} \boldsymbol{G}^T \mathbf{A} \boldsymbol{G} \, \mathrm{d}V \right\} \delta \boldsymbol{u} \cdot \boldsymbol{\eta} = \Bigg\{ & -\int_{\Omega^h} \boldsymbol{G}^T \boldsymbol{P} \, \mathrm{d}V + \\ & \int_{\partial \Omega^h} \boldsymbol{N}^T \boldsymbol{t} \, \mathrm{d}A + \int_{\Omega^h} \boldsymbol{N}^T \boldsymbol{f} \mathrm{d}V \Bigg\} \cdot \boldsymbol{\eta} \end{aligned} \tag{4.14}$$

The Newton-Raphson method consists of solving the linear system of equations at each iteration (k),

$$\boldsymbol{K} \delta \boldsymbol{u}^{(k)} = -\mathbf{R}^{(k-1)}, \tag{4.15}$$

where, $\mathbf{R}^{(k-1)} = \boldsymbol{f}^{\text{int}}(\boldsymbol{u}_{n+1}^{(k-1)}) - \boldsymbol{f}_{n+1}^{\text{ext}}$ is the residual vector and $\boldsymbol{K} = \left.\dfrac{\partial \mathbf{R}}{\partial \boldsymbol{u}_{n+1}}\right|_{\boldsymbol{u}_{n+1}^{k-1}}$ is the global tangent stiffness matrix.

Finally, we can update the global displacement vector $\boldsymbol{u}_{n+1}^{k}$ by having $\delta \boldsymbol{u}^{k}$ at hand as,

$$\boldsymbol{u}_{n+1}^{k} = \boldsymbol{u}_{n+1}^{k-1} + \delta \boldsymbol{u}^{k}. \tag{4.16}$$

4.2 Explicit Solver Strategies

In this section, the explicit dynamic analysis of large strain problems are well established. The stability is crucial for the explicit method and it is restricted by requirements of stability. The procedure is only conditionally stable if the time step is below the critical value Δt_{crit} which is governed by the Courant stability limit for detailed analysis see, [64; 66–68]. Note that, small time steps often below the critical time step or stability limit, are imposed by the requirements of the wave-

speed. The essential features for the explicit finite element method are summarized in the following sections.

4.2.1 The Discretized Dynamic Equations

It is important to mention that, we are working on the current configuration. Therefore, according to the equation of motion in equation (2.16), the weak form of the momentum balance for the explicit dynamic equation is expressed as,

$$\delta W = \int_{\Omega} \boldsymbol{P} : \nabla \boldsymbol{\eta} \, \mathrm{d}V - \int_{\partial\Omega} \boldsymbol{t}\boldsymbol{\eta} \, \mathrm{d}A - \int_{\Omega} \boldsymbol{f}\boldsymbol{\eta} \, \mathrm{d}V + \int_{\Omega} \rho \boldsymbol{a}\boldsymbol{\eta} \mathrm{d}V \quad \forall \boldsymbol{\eta} \in \mathscr{V} \tag{4.17}$$

It can be seen that the dynamic effecting represented by the acceleration field $\boldsymbol{a} = \ddot{\boldsymbol{u}}$. By applying the standard incremental finite element discretization, explained in section 4.1.1, the equation of motion is expressed as

$$\begin{aligned} \int_{\Omega^h} \boldsymbol{G}^T \boldsymbol{P}^{n+1}(\boldsymbol{F}^{n+1}, \boldsymbol{\alpha}^n) \, \mathrm{d}V - \int_{\partial\Omega^h} \boldsymbol{N}^T \boldsymbol{t}^{n+1} \, \mathrm{d}A - \int_{\Omega^h} \boldsymbol{N}^T \boldsymbol{f}^{n+1} \, \mathrm{d}V \\ + \underbrace{\int_{\Omega^h} \rho \boldsymbol{a}^{n+1} \boldsymbol{N}^T \boldsymbol{N} \, \mathrm{d}V}_{\mathrm{M}} = \boldsymbol{0} \end{aligned} \tag{4.18}$$

Or can be represented as,

$$\mathrm{M}\boldsymbol{u}^{n+1} + \boldsymbol{f}^{\mathrm{int}\, n} = \boldsymbol{f}^{\mathrm{ext}\, n} \tag{4.19}$$

where, M is the mass matrix and $\boldsymbol{u}$ represent the displacement vector.
The explicit integration of the non-linear equation above is solved by *the central difference method* which is the most popular approximation for the explicit methods in computational mechanics and physics. Since the stable time step changes as the wave speed are varying and the mesh deforms due to the change in the stress, the time step is obtained through an algorithm. For this purpose, the time increments define by,

$$\Delta \boldsymbol{t}^{n+1/2} = \boldsymbol{t}^{n+1} - \boldsymbol{t}^{n}, \quad \boldsymbol{t}^{n+1/2} = \frac{1}{2}(\boldsymbol{t}^{n+1} + \boldsymbol{t}^{n}), \quad \Delta \boldsymbol{t}^{n} = \boldsymbol{t}^{n+1/2} - \boldsymbol{t}^{n-1/2} \tag{4.20}$$

Hence, the expression for central difference velocity $\boldsymbol{v}$ can be obtained as,

$$\boldsymbol{v}^{n+1/2} = \frac{\boldsymbol{u}^{n+1/2} - \boldsymbol{u}^{n}}{\boldsymbol{t}^{n+1} - \boldsymbol{t}} = \frac{1}{\Delta \boldsymbol{t}^{n+1/2}}(\boldsymbol{u}^{n+1} - \boldsymbol{u}^{n}) \tag{4.21}$$

This difference expression above can be written to an integration formula as follows:

$$\boldsymbol{u}^{n+1} = \boldsymbol{u}^{n} + \Delta \boldsymbol{t}^{n+1/2} \boldsymbol{v}^{n+1/2} \tag{4.22}$$

Also, the central difference for acceleration and its integration is as,

$$\boldsymbol{a}^{n} = \left[\frac{\boldsymbol{v}^{n+1/2} - \boldsymbol{v}^{n-1/2}}{\boldsymbol{t}^{n+1/2} - \boldsymbol{t}^{n-1/2}} \right] \quad \text{Therefore} \quad \boldsymbol{v}^{n+1/2} = \boldsymbol{v}^{n-1/2} + \Delta \boldsymbol{t}^{n} \boldsymbol{a}^{n} \tag{4.23}$$

Note that, the equation (4.19) is discretized in space but not in time, it is often called as semidiscrete. By using expression (4.23), the velocity formula can be written in terms of mass matrix M as,

$$\boldsymbol{v}^{n+1/2} = \boldsymbol{v}^{n-1/2} + \Delta \boldsymbol{t}^{n} \mathrm{M}^{-1} \{ \boldsymbol{f}^{n,\mathrm{ext}} - \boldsymbol{f}^{n,\mathrm{int}} \} \tag{4.24}$$

The update of the nodal velocities and nodal displacements in equations (4.22) and (4.24) respectively are not required only if the mass matrix M is diagonal. This is the salient characteristic of an explicit method. That is, the time integration of the discrete momentum equations for the explicit method does not involve the solution of any equations on the use of a diagonal mass matrix. Therefore, the estimation of nodal displacement can then occurring only through the the internal forces. This makes explicit dynamic analysis useful approach for many industrially relevant problems.

Critical Time Step

The above time integration scheme is conditional. The stability relies on the permissible time step being governed by the Courant stability limit. This limit can be obtained in terms of the highest frequency in the system $\omega_{\max}$ as,

$$\Delta \boldsymbol{t}_{\mathrm{crit}} = \frac{2}{\omega_{\max}} \tag{4.25}$$

The expression above is logical when there is no damping in the system. Therefore, it requires modification for the problems with damping, which normally causes in reduction of the critical time. Solving the practical problems with $\Delta \boldsymbol{t}_{\text{crit}}$ can be computationally expensive. Because of that, the estimation of a lower-bound of the critical time step is employed

$$\Delta \boldsymbol{t} = \alpha \left(\frac{2}{\omega_{\max}} \leq \min \frac{2}{\omega^e} = \min \frac{l^e}{c^e} \right) = \alpha \Delta \boldsymbol{t}_{\text{crit}} \tag{4.26}$$

where $\omega_{\max}$ is the maximum frequency of the linearized system, l^e is a characteristic length of element e, c^e the current wavespeed in element e, and α is a Courant number or reduction factor, usually is taken as $0.8 \leq \alpha \leq 0.98$.
To pick the time step for the meshed model, first calculating the time step for each element and the minimum element time step is taken as the mesh time step.

4.2.2 Stress Integration

In explicit analysis the computational costs are from stress update procedures which is combined by the stability restriction on the time incrementation size. In explicit codes is computationally expensive for the use of industries to update the deformation gradient and the polar decomposition. Therefore, the use of hypoelastic constitutive equations is the solution to this. The hypoelastic constitutive law is commonly used in explicit dynamic codes. This law relates rate of stress $\overset{\circ}{\boldsymbol{\tau}}$ to the deformation rate $\boldsymbol{d}$ through the relation, which is almost exclusively assumed in a linear form given as

$$\overset{\circ}{\boldsymbol{\tau}} = \overline{\mathbf{h}} : \boldsymbol{d} \tag{4.27}$$

where $\overline{\mathbf{h}}$ is the elastic modulus and depends on the choice of the constitutive relation. This type must be written in terms of objective rates to maintain correct rotational transformation properties for more detailes see [69] and [66].
The stress integration procedures of hypoelastic constitutive law in equation (4.27) requires to follow the condition of *incremental objectivity* which is formalized by [70] and it has been used in computational framework to obtain the stress integration algorithms. This algorithm prevents the spurious stresses generation in rigid body. One of the most used hypoelastic constitutive laws is the *Jaumann rate of the*

Kirchhoff stress and it is expressed as,

$$\overset{\nabla}{\tau} = \dot{\boldsymbol{\tau}} + \boldsymbol{\tau}\boldsymbol{w} - \boldsymbol{w}\boldsymbol{\tau} \tag{4.28}$$

where, $\boldsymbol{w}$ is the spin tensor which represent the skew part of the velocity gradient, $\boldsymbol{w}$ = skew[$\boldsymbol{l}$]. The incrementation of the strain and the spin tensor at the midpoint of the time interval is assessed for the implementation of the stress integration algorithm in the explicit finite element as,

$$\begin{aligned} \boldsymbol{d}_{n+1/2} &= \frac{1}{2}\left(\nabla_{n+1/2}\boldsymbol{v}n + 1/2 + \nabla^{T}_{n+1/2}\boldsymbol{v}n + 1/2\right) \\ \boldsymbol{w}_{n+1/2} &= \frac{1}{2}\left(\nabla_{n+1/2}\boldsymbol{v}n + 1/2 - \nabla^{T}_{n+1/2}\boldsymbol{v}n + 1/2\right) \end{aligned} \tag{4.29}$$

With,

$$\begin{aligned} \nabla_{n+1/2}\boldsymbol{v}_{n+1/2} &= \frac{\partial \boldsymbol{v}_{n+1/2}}{\partial \boldsymbol{x}_{n+1/2}} \\ \boldsymbol{x}_{n+1/2} &= \boldsymbol{x}_n + \frac{\Delta \boldsymbol{t}^{n+1/2}}{2}\boldsymbol{v}_{n+1/2} \end{aligned} \tag{4.30}$$

The following procedure is used to update the stress,

$$\begin{aligned} \boldsymbol{\tau}^{*} &= \boldsymbol{\tau}_n + \frac{\Delta \boldsymbol{t}^{n+1/2}}{2}(\boldsymbol{\tau}_n\boldsymbol{w}_{n+1/2} - \boldsymbol{w}_{n+1/2}\boldsymbol{\tau}_n) \\ \boldsymbol{\tau}_{n+1/2} &= \hat{\boldsymbol{\tau}}(\boldsymbol{\tau}^{*}_n, \boldsymbol{e}_{n+1/2}, \boldsymbol{\alpha}^{*}_n) \\ \boldsymbol{\tau}_{n+1} &= \boldsymbol{\tau}_{n+1/2} + \frac{\Delta \boldsymbol{t}^{n+1/2}}{2}(\boldsymbol{\tau}_{n+1/2}\boldsymbol{w}_{n+1/2} - \boldsymbol{w}_{n+1}\boldsymbol{\tau}_{n+1/2}) \end{aligned} \tag{4.31}$$

where $\boldsymbol{e}_{n+1/2}$ is a tensor evaluated on a midpoint approximation of the incrementation of the strain, $\Delta t\boldsymbol{d}_{n+1/2}$ and $\boldsymbol{\alpha}^{*}$ represents the set of internal variables, it may need those three steps above if tensorial variables are included. The stress at the midpoint is coming through the chosen constitutive algorithm in the equation $(4.31)_2$ and it is normally in the small strain regime.

The above procedure, can be simplified more in order to reduce computational costs, by computing the $\hat{\boldsymbol{\tau}}$ at the end point of the time increment t_{n+1}. However, not considering the *incremental objectivity* is the main disadvantage of this scheme and also, time step is crucially restricted to the stability condition in (4.26).

Note that, there are other implementations or schemes in order to insure the in-

cremental objectivity in explicit dynamic codes to allow for anisotropic materials and reduce the difficulties in description of kinematic hardening of elaso-plastic materials. However, at the same time, the computational costs goes up in terms of memory and a number of operations.

4.3 Element Methodology

The poor performance of the low-order interpolation polynomials in the finite element under near incompressibility is a notable fact. One of the typical model is, elasto-plastic simulations under plastic deformations that we are facing in this work. In such a situation, the *volumetric locking* occurs which is increasing in stiffness and represent volume-preserving displacement fields. However, despite their disadvantage, they are preferred in engineering practical problems. Due to their simplicity and robustness, they reduce computational costs and make the finite element models faster. Several methods have been proposed by researchers (for detailed analysis see, [71–75] for both explicit and implicit finite element analysis, in order to tackle the problem. And, make the lower order elements usable for large-scale computational and nearly incompressible solids. In this section, we are looking at the F-bar method proposed by [76] in case of the implicit finite element method and *hourglass techniques* proposed by [77] for explicit transient dynamic analysis briefly.

4.3.1 The F-Bar Methodology

In large strain elastoplastic problems, the incompressibility effect dominate and caused the low order elements to fail under volumetric locking effect. One alternative technique that has been demonstrated to be applicable to this problem is, the use of the F-bar method. This method follows the standard finite element implementation by modifying the deformation gradient. In order to construct the F-bar deformation gradient $\boldsymbol{F}_{\text{f-bar}}$, the multiplicative split of the deformation gradient is applied at both, the Gauss point of the interest and at the *centroid* of the element, $\xi = \xi_0$ (Figure 4.1 illustrates the procedure for the four-noded quadrilateral element):

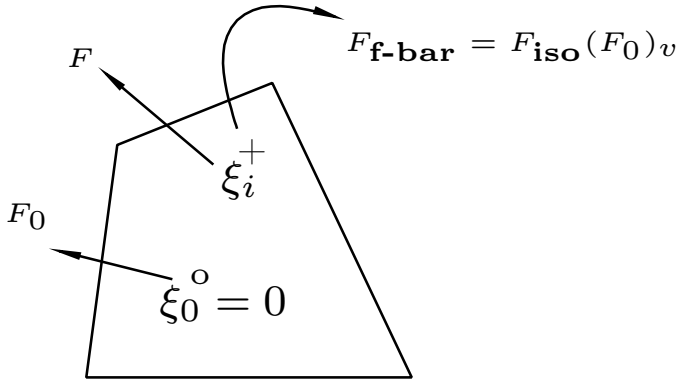

Figure 4.1: The *F-bar* four-node quadrilateral for large strain analysis model.

$$\boldsymbol{F} = \boldsymbol{F}_{\text{iso}}\boldsymbol{F}_v, \quad \boldsymbol{F}_0 = (\boldsymbol{F}_0)_{\text{iso}}(\boldsymbol{F}_0)_v \tag{4.32}$$

And by using the multiplicative split relation $\boldsymbol{F}_{\text{iso}} = (\det\boldsymbol{F})^{1/3}\boldsymbol{F}$, the F-bar deformation gradient can be defined as,

$$\boldsymbol{F}_{\mathbf{f\text{-}bar}} = \boldsymbol{F}_{\text{iso}}(\boldsymbol{F}_0)_v = \left(\frac{\det\boldsymbol{F}_0}{\det\boldsymbol{F}}\right)^{1/3}\boldsymbol{F}. \tag{4.33}$$

Now by having the $\boldsymbol{F}_{\mathbf{f\text{-}bar}}$, we can update stresses at the each Gauss point. Therefore, the first term of the boundary value problem of expression (2.27) can be rewrite as,

$$\int_{\omega} \hat{\boldsymbol{\sigma}}(\boldsymbol{F}_{\mathbf{f\text{-}bar}}) : \nabla\boldsymbol{\eta}\, \mathrm{d}v. \tag{4.34}$$

And the internal force vector can simply follow the standard finite element procedure, the only difference is that, in F-bar elements, the calculation of the stresses at $\boldsymbol{F}_{\mathbf{f\text{-}bar}}$ through the constitutive function. The procedure is simple as can be seen in (4.33), the modified deformation gradient is simply calculated by multiplying $\boldsymbol{F}$ by a scalar factor. Also, the first Piola-Kichhoff stress can simply be obtained as,

$$\boldsymbol{P} = \det[\boldsymbol{F}_{\mathbf{f\text{-}bar}}]\, \hat{\boldsymbol{\sigma}}(\boldsymbol{F}_{\mathbf{f\text{-}bar}})\, \boldsymbol{F}_{\mathbf{f\text{-}bar}}^{-T} \tag{4.35}$$

Note that, the c.p.u time required to compute the F-bar tangent stiffness is slightly longer than the standard elements. That is, due to the extra term at the element centroid. The tangent stiffness on the left hand side of the equation (4.14) for the

F-bar element is,

$$\boldsymbol{K} = \int_{\Omega^h} \boldsymbol{G}^T \mathbf{A} \Big|_{\boldsymbol{F}=\boldsymbol{F}_{\text{f-bar}}} \boldsymbol{G} \mathrm{d}V + \underbrace{\int_{\Omega^h} \boldsymbol{G}^T \boldsymbol{q} \, (\boldsymbol{G}_0 - \boldsymbol{G}) \, \mathrm{d}V}_{\text{additionl stiffness}} \tag{4.36}$$

where, $\boldsymbol{G}_0$ is the gradient operator at the element centroid and $\boldsymbol{q}$ is the forth order tensor which is computed at $\boldsymbol{F}_{\text{f-bar}}$. It is defined by

$$\boldsymbol{q} = \frac{1}{3} \boldsymbol{A} : (\boldsymbol{I} \otimes \boldsymbol{I}) - \frac{2}{3} (\boldsymbol{\sigma} \otimes \boldsymbol{I}). \tag{4.37}$$

The F-bar elements have been proved to be accurate under near-incompressibility and more advanced constitutive models. In Figure 4.2, the difference between the standard four-node and F-bar quadrilateral element under combined compression and shear loading with Drucker-Prager constitutive model is shown. The mesh

(a) (b)

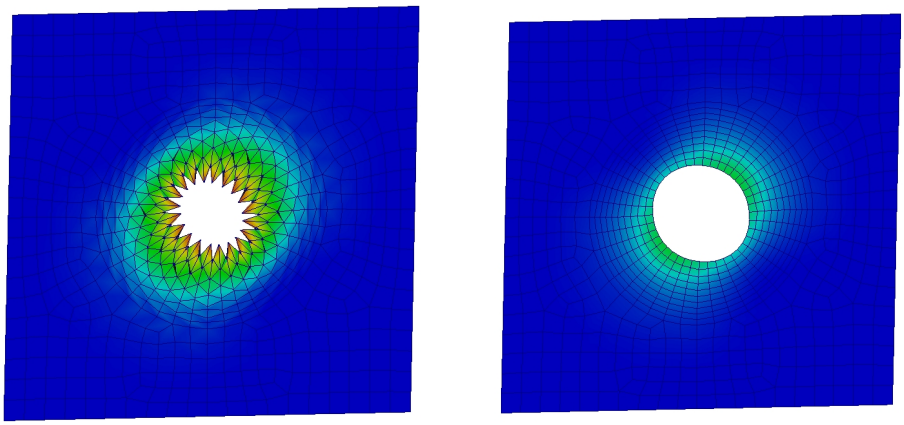

Figure 4.2: 2D models.(a) Standard element (b) F-bar element.

distortion can be seen when using the standard element which impact on the accuracy and stability of the model.

4.3.2 Hourglass Methodology

The industrial simulations are invariably large and therefore using under-integrated or one point quadrature element is essential as it makes the simulations three to four in 2-D and six to eight times faster in 3-D, reduces the computational costs and

it can prevent the elements locking near incompressibility. The major draw back of the reduced integration procedures is known as *hourglassing* or mesh instability which first recognized by [78]. They appear in finite elements as kinematic modes or spurious zero-energy modes; see for example [79–81]. They cause singularity of the assembled stiffness matrix in static solutions, pressure oscillations, and in addition influences displacement field instabilities. Various techniques have been developed to control the hourglass modes, one of the earliest of these is the technique developed by [78] who added artificial viscosity to prevent opposing rotations of the sides of the quadrilateral zone. And, the computational version of hourglass viscosity or viscous damping has been developed by [82] and [83–85]. The other method which is used in this work is, adding artificial stiffness without effecting the global modes. Both methods are capable of controlling the hourglassing at singular modes. However, it should be noted that the control techniques do not fully remove kinematic modes and, with coarse meshes or meshes under large nodal forces, the hourglassing are likely to happen. Figure 4.3 illustrates the hourglassing effect on a four-node quadrilateral element.

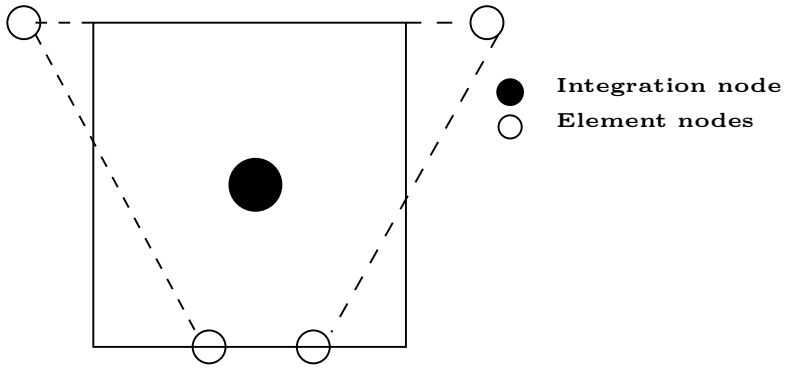

Figure 4.3: The *hourglassing* four-node quadrilateral element.

Chapter 5

Multi-Scale Homogenization

Industrial and engineering materials as well as natural materials are heterogeneous at a certain scale. Due to the highly heterogeneous medium, there are two different scales are considered. The *macroscopic scale*, where the response at each point of the macroscopic continuum is, the homogenization of the response of a *Representative Volume Element* (RVE) at that point (see Figure 5.1). The examples include polycrystalline materials, composites, porous, cracked media and many other materials. The interest in the multi-scale approaches is noticeable from number of published journal articles in this area [49; 86–91] and etc. Such a model has high popularity in computational mechanics community for their suitability in the finite element implementation based on computer simulation frameworks. The homogenization multi-scale constitutive theory is the assumption that, any material at any point in macroscopic continuum is associated to RVE with a length much smaller than the length of the macro-continuum. The homogenization-based multi-scale theory providing here based on the kinematical variational framework as proposed by [92], The formulation expressed in an axiomatic manner based on the following principles:

- RVE equilibrium,
- volume averaging of stress and strain tensors
- the additive split of the microscopic displacement defining the constraint on the kinematically admissible displacements of the RVE and,
- the *Hill-Mandel principle of macro-homogeneity.*

The physics and the mechanics of the RVE has a significant impact on the behavior of the macroscopic material. For instance, the overall response of the macroscopic continuum depends strongly on the size, shape, spatial distribution and properties of the micro-structural constituents and their respective interfaces.

In this chapter, we describe well known classes of multi-scale theories for large strain in solid mechanics. By describing the equilibrium equations of the macro-continuum and the micro-structure at the reference configuration within the variational framework above, then introducing the coupling of scales (homogenization). This develops the homogenization of the strain (deformation gradient in large strain) and the stress, an essential aspect in the formulation of the multi-scale theory which is the Hill-Mandel Principle of Macro-homogeneity and the additive split of the microscopic displacement. A family of the kinematical constraints that can be imposed on the RVE are introduced next. Finally, presenting the numerical examples to illustrate the scope and benefits of the multi-scale computational strategy such as, the effect of boundary conditions, topology and distribution of heterogeneities.

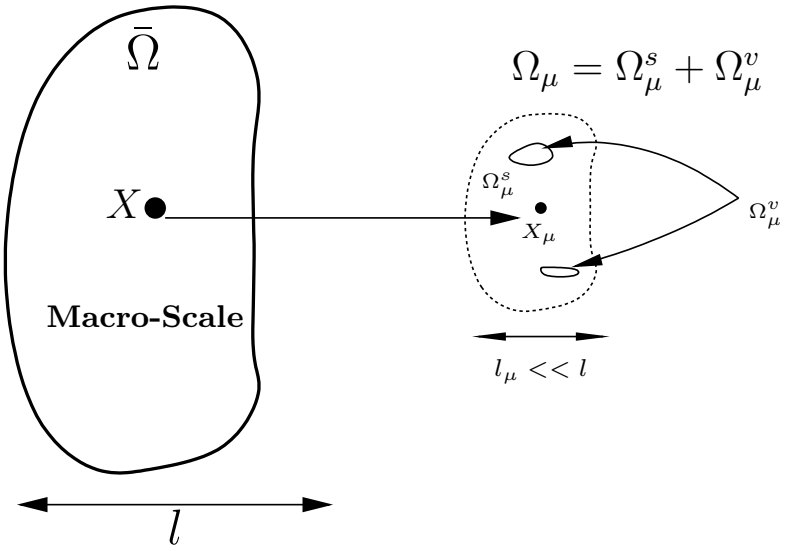

Figure 5.1: Macro-continuum with a locally attached micro-structure.

5.1 Macroscopic Boundary Value Problem

The macroscopic equilibrium problem is written in the reference configuration and the macroscopic stress is formulated as First Piola-Kirchoff stress $\bar{\boldsymbol{P}}$. To find the kinematically admissible displacement field $\bar{\boldsymbol{u}} \in \bar{\mathscr{K}}$, using the following formulas,

$$\int_{\bar{\Omega}} \bar{\boldsymbol{P}} : \nabla\bar{\boldsymbol{\eta}}\, \mathrm{d}V - \int_{\bar{\Omega}} \bar{\boldsymbol{b}}(\boldsymbol{X}, t) \cdot \bar{\boldsymbol{\eta}}\, \mathrm{d}V - \int_{\partial\bar{\Omega}} \bar{\boldsymbol{t}}(\boldsymbol{X}, t) \cdot \bar{\boldsymbol{\eta}}\, \mathrm{d}A = 0 \quad \forall\bar{\boldsymbol{\eta}} \in \bar{\mathscr{V}} \tag{5.1}$$

holds for any time t. The solution of the a kinematically admissible displacement field $\bar{\boldsymbol{u}}$ is the stress at each point, $\boldsymbol{X}$, at time t and is in the form,

$$\begin{aligned} \int_{\bar{\Omega}} \bar{\boldsymbol{P}} : \nabla\bar{\boldsymbol{\eta}}\, \mathrm{d}V &= \int_{\bar{\Omega}} \bar{\mathfrak{S}}(\bar{\boldsymbol{F}}^t(\boldsymbol{X})) : \nabla\bar{\eta}\, \mathrm{d}V \\ &= \int_{\bar{\Omega}} \bar{\mathfrak{S}}([I + \nabla\bar{\boldsymbol{u}}(\boldsymbol{X})]^t) : \nabla\bar{\eta}\, \mathrm{d}V. \quad \forall\bar{\boldsymbol{\eta}} \in \bar{\mathscr{V}} \end{aligned} \tag{5.2}$$

where, $\mathfrak{S}$ is a constitutive functional of the deformation gradient and $\bar{\eta}$ is the virtual kinematically admissible in the virtual space of $\bar{\mathscr{V}}$

The RVE Equilibrium

In order to find the kinimatically admissible micro-scale deformation gradient $\boldsymbol{F}_\mu$ of the RVE, in the reference configuration, the weak form of the BVP is in the form,

$$\begin{aligned} \int_{\Omega_\mu} \boldsymbol{P}_\mu : \nabla\boldsymbol{\eta}\, \mathrm{d}V &- \int_{\Omega_\mu} \boldsymbol{b}(\boldsymbol{X}_\mu, t) \cdot \boldsymbol{\eta}\, \mathrm{d}V \\ &- \int_{\partial\Omega_\mu} \boldsymbol{t}(\boldsymbol{X}_\mu, t) \cdot \boldsymbol{\eta}\, \mathrm{d}A = 0 \quad \forall\boldsymbol{\eta} \in \mathscr{V} \end{aligned} \tag{5.3}$$

where, Ω_μ and $\partial\Omega_\mu$ are representing the volume and the boundary of the RVE in the initial configuration see Figure 5.2. Note that RVE is made of solid and void phase ($\Omega_\mu = \Omega_\mu^s \cup \Omega_\mu^v$) , due to the assumption that there is no traction between the void and solid phase of the RVE, we only considering the solid phase, therefore $\Omega_\mu = \Omega_\mu^s$.

The deformation of the RVE is driven by the macroscopic deformation gradient $\bar{\boldsymbol{F}}$. Therefore, homogenization theory is used here to relate the micro to macro scale deformation gradient and the theory will be described in following section.

5.2 Homogenization

The coupling of macroscopic to microscopic scale is based on homogenization of stress and strain tensors. The homogenize properties, such as, deformation gradient,

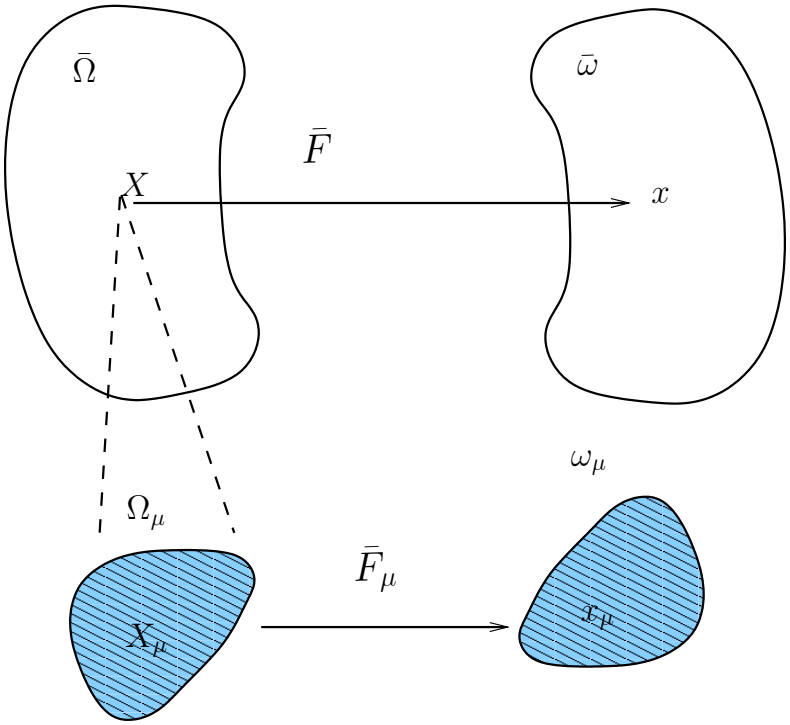

Figure 5.2: Deformation of the macro-continuum and the micro structure. The initial and deformed configurations of the macro-continuum are $(\bar{\Omega}\,, \bar{\omega})$ respectively. The corresponding configurations for the micro structure are $(\Omega_\mu\,, \omega_\mu)$.

appropriate stress, and stress power based on the Hill-Mandel principle and finally, the additive split of the microscopic displacement field is described in the following.

5.2.1 Homogenized Deformation Gradient

The starting point of the kinematical variational framework of multi-scale theory is the relationship between the macroscopic and microscopic strains. The assumption made is that at any time t, the macroscopic deformation gradient $\bar{\boldsymbol{F}}$ at a point $\boldsymbol{X}$ on the macro-continuum is the volume average of the microscopic deformation gradient $\boldsymbol{F_\mu}$ with in the RVE associated with $\boldsymbol{X}$:

$$\bar{\boldsymbol{F}}(\boldsymbol{X}, t) = \frac{1}{V_\mu} \int_{\Omega_\mu} \boldsymbol{F}_\mu \, \mathrm{d}V \tag{5.4}$$

where, V_μ is the volume of the RVE in its initial configuration.

By using the definition of the deformation gradient, the equation above can also be written as,

$$\bar{\boldsymbol{F}}(\boldsymbol{X}, t) = \boldsymbol{I} + \frac{1}{V_\mu} \int_{\Omega_\mu} \nabla \boldsymbol{u}_\mu(\boldsymbol{X}_\mu, t) \, \mathrm{d}V \tag{5.5}$$

5.2.2 Homogenized Stress

The macroscopic first Pilo-Kirchhof tensor $\bar{\boldsymbol{P}}$ at a point $\boldsymbol{X}$ of the macro-continuum is also defined, at any time t, as the volume average of the microscopic first Pilo-Kirchhof stress $\boldsymbol{P}_\mu$ over the RVE.

$$\bar{\boldsymbol{P}} = \frac{1}{V_\mu} \int_{\Omega_\mu} \boldsymbol{P}_\mu \, \mathrm{d}V \tag{5.6}$$

Homogenization also applies to the other stress measure such as, Cauchy, the second Piola-Kirchhoff and Kirchhoff stresses. As, the RVE volume can be in initial or deformed configuration.

The homogenized stress tensor can also be formulated in terms of boundary traction $\boldsymbol{t}$ and body force $\boldsymbol{b}$,

$$\begin{aligned} \frac{1}{V_\mu} \int_{\Omega_\mu} \boldsymbol{P}_\mu \, \mathrm{d}V &= \frac{1}{V_\mu} \int_{\Omega_\mu} \boldsymbol{P}_\mu (\nabla \boldsymbol{X}_\mu)^T \, \mathrm{d}V \\ &= \frac{1}{V_\mu} \int_{\Omega_\mu} \boldsymbol{P}_\mu \boldsymbol{N} \otimes \boldsymbol{X}_\mu \, \mathrm{d}A - \frac{1}{V_\mu} \int_{\Omega_\mu} \mathrm{div} \boldsymbol{P}_\mu \otimes \boldsymbol{X}_\mu \mathrm{d}V \\ &= \frac{1}{V_\mu} \int_{\Omega_\mu} \boldsymbol{t} \otimes \boldsymbol{X}_\mu \, \mathrm{d}A - \frac{1}{V_\mu} \int_{\Omega_\mu} \boldsymbol{b} \otimes \boldsymbol{X}_\mu \, \mathrm{d}V \end{aligned} \tag{5.7}$$

5.2.3 Additive Split of RVE Displacement Field

Microscopic displacement field can be split into sum of homogenized displacement and fluctuation displacement $\tilde{\boldsymbol{u}}_\mu$ as,

$$\boldsymbol{u}_\mu = \bar{\boldsymbol{u}} + \tilde{\boldsymbol{u}}_\mu \tag{5.8}$$

where, $\bar{\boldsymbol{u}} = [\bar{\boldsymbol{F}} - I]\boldsymbol{X}_\mu$.

The displacement $\bar{\boldsymbol{u}}$ varies linearly in $\boldsymbol{X}_\mu$ and is homogeneous over the entire RVE while the displacement fluctuation $\tilde{\boldsymbol{u}}_\mu$ accounts for the deformation occurring at the RVE level and does not contribute to the overall deformation of the macro-continuum. As, the fluctuation displacements field is crucial to define the space of virtual kinematically admissible displacements (will be described in the following section). Hence, the microscopic deformation gradient can also be expressed as,

$$\boldsymbol{F}_\mu = \boldsymbol{I} + \nabla \boldsymbol{u}_\mu = \bar{\boldsymbol{F}} + \nabla \tilde{\boldsymbol{u}}_\mu. \tag{5.9}$$

5.2.4 Hill-Mandel Principle

In macro homogeneity, the Hill-Mandel principle is one of the crucial aspect. It states that, for any kinematically admissible motion of the RVE, the macroscopic stress power is related to the microscopic stress power by volume averaging. It is expressed as,

$$\bar{\boldsymbol{P}} : \dot{\bar{\boldsymbol{F}}} = \frac{1}{V_\mu} \int_{\Omega_\mu} \boldsymbol{P}_\mu : \dot{\boldsymbol{F}}_\mu \, \mathrm{d}V \tag{5.10}$$

This principle says that, the body and traction force are zero according to the chosen constraint. This can be shown by using the additive split into the equation above,

$$\begin{aligned} \bar{\boldsymbol{P}} : \dot{\bar{\boldsymbol{F}}} &= \frac{1}{V_\mu} \int_{\Omega_\mu} \boldsymbol{P} : (\dot{\bar{\boldsymbol{F}}} + \nabla \dot{\tilde{\boldsymbol{u}}}_\mu) \, \mathrm{d}V \\ &= \bar{\boldsymbol{P}} : \dot{\bar{\boldsymbol{F}}} + \frac{1}{V_\mu} \int_{\Omega_\mu} \boldsymbol{P}_\mu : \nabla \dot{\tilde{\boldsymbol{u}}}_\mu \, \mathrm{d}V \end{aligned} \tag{5.11}$$

which implies that,

$$\frac{1}{V_\mu} \int_{\Omega_\mu} \boldsymbol{P}_\mu : \nabla \dot{\tilde{\boldsymbol{u}}}_\mu \, \mathrm{d}V = 0 \quad \forall \dot{\tilde{\boldsymbol{u}}}_\mu \in \mathscr{V} \tag{5.12}$$

By applying integration by part to the above equation and and using the strong form of the equilibrium, the expression (5.12) can be written as,

$$\int_{\partial\Omega_\mu} \boldsymbol{t} \cdot \dot{\tilde{\boldsymbol{u}}}_\mu \, \mathrm{d}A - \int_{\Omega_\mu} \boldsymbol{b} \cdot \dot{\tilde{\boldsymbol{u}}}_\mu \, \mathrm{d}V = 0 \quad \forall \dot{\tilde{\boldsymbol{u}}}_\mu \in \mathscr{V} \tag{5.13}$$

Therefore, this provides the equilibrium equation of the RVE reduces to

$$\int_{\Omega_\mu} \boldsymbol{P}_\mu : \nabla \boldsymbol{\eta} \, \mathrm{d}V = 0 \quad \forall \boldsymbol{\eta} \in \mathscr{V} \tag{5.14}$$

Further, we assume that at any time t the stress at each point $\boldsymbol{X}_\mu$ of the RVE is delivered by a generic constitutive functional $\mathfrak{S}$ of the deformation gradient history at that point up to time t:

$$\boldsymbol{P}_\mu = \mathfrak{S}\{[\bar{\boldsymbol{F}} + \nabla \tilde{\boldsymbol{u}}(\boldsymbol{X}_\mu)]^t\} \tag{5.15}$$

Now by having this assumption together with the RVE equilibrium equation, gives the RVE equilibrium problem which consists in solving for a displacement fluctua-

tion function $\tilde{\boldsymbol{u}}$ for a given macroscopic deformation gradient such that

$$\int_{\Omega_\mu} \mathfrak{S}\{[\bar{\boldsymbol{F}} + \nabla\tilde{\boldsymbol{u}}(\boldsymbol{X}_\mu)]^t\} : \nabla\boldsymbol{\eta}\, \mathrm{d}V = 0 \quad \forall\boldsymbol{\eta} \in \mathscr{V} \tag{5.16}$$

5.3 Kinematical Constraints

The kinematical constraint on the RVE has to be defined. In this case, defining the space of kinematically admissible microscopic displacements and consequently the space of virtual kinematically admissible microscopic displacements $\mathscr{V}$.
Minimum kinematical constraint is one of the kinematical constraint that can be applied to the RVE. Further constraints will be introduced in following sections. By varying the choice of kinematical constraints, there will be different classes of multi-scale models

5.3.1 The Minimum Kinematical Constraint

By making use of Green's theorem to the equation (5.5), it can easily be established that the deformation gradient is equivalent to the following constraint on the allowable deformation of the RVE.

$$\int_{\partial\Omega_\mu} \boldsymbol{u}_\mu \otimes \boldsymbol{N} dA = V_\mu(\bar{\boldsymbol{F}} - \boldsymbol{I}). \tag{5.17}$$

where, $\boldsymbol{N}$ is the outward unit normal field on $\partial\Omega_\mu$.
This constraint requires the space of kinematically admissible RVE displacement fields $\mathscr{K}$ to be subset of the minimally constrained set of kinematically admissible microscopic displacements, $\mathscr{K}^*$:

$$\mathscr{K} \subset \mathscr{K}^* \equiv \left\{\boldsymbol{v}, \text{sufficiently regular} \middle| \int_{\partial\Omega_\mu} \boldsymbol{v} \otimes \boldsymbol{N}\, \mathrm{d}A = V_\mu(\bar{\boldsymbol{F}} - \boldsymbol{I})\right\}, \tag{5.18}$$

with a sufficiently regular field meaning that all the operations in which they are involved make sense [92]. The constrain set can be expressed in terms of the microscopic displacement fluctuations, by using the additive split as

$$\tilde{\mathscr{K}} \subset \tilde{\mathscr{K}}^* \equiv \left\{\boldsymbol{v}, \text{sufficiently regular} \middle| \int_{\partial\Omega_\mu} \boldsymbol{v} \otimes \boldsymbol{N} \mathrm{d}A = 0\right\} \tag{5.19}$$

with $\tilde{\mathscr{K}}$ being the space of kinematically admissible microscopic displacement fluctuations (with $\tilde{\boldsymbol{u}}_\mu \in \tilde{\mathscr{K}}$) and $\tilde{\mathscr{K}}^*$ being the minimally constrained space of kinematically admissible microscopic displacement fluctuations.

For this class of virtual work-based variational setting, the virtual displacements are defined as variations in the kinematically admissible of RVE displacements. Based on that, the associated space of virtual kinematically admissible of microscopic displacements can be expressed as

$$\mathscr{V} \equiv \left\{ \boldsymbol{\eta} = \boldsymbol{v}_1 - \boldsymbol{v}_2 | \boldsymbol{v}_1, \boldsymbol{v}_2 \in \mathscr{K} \right\} \tag{5.20}$$

According to additive split, the equation above can be written in form

$$\mathscr{V} \equiv \left\{ \boldsymbol{\eta} = \tilde{\boldsymbol{v}}_1 - \tilde{\boldsymbol{v}}_2 | \tilde{\boldsymbol{v}}_1, \tilde{\boldsymbol{v}}_2 \in \tilde{\mathscr{K}} \right\} \tag{5.21}$$

Therefore, it coincides with the space of kinematically admissible displacement fluctuations:

$$\mathscr{V} = \tilde{\mathscr{K}} \subset \tilde{\mathscr{K}}^*. \tag{5.22}$$

5.3.2 Multi-Scale Models

The characterization of a multi-scale model depends on the choice of expression (5.19). Classically four types of conditions are used to solve the problem at micro-level: prescribed uniform deformation (or the Taylor) assumption, the linear boundary displacement condition, the periodic boundary displacement fluctuations condition and the uniform boundary traction assumption. The following choices are:

- Taylor:

  Deformation gradient is uniform over the RVE. Therefore, fluctuation displacement is zero over the entire RVE. The equation (5.8) reduces to,

  $$\boldsymbol{u}_\mu = \left[\bar{\boldsymbol{F}} - \boldsymbol{I} \right] \boldsymbol{X}_\mu \quad \forall \boldsymbol{X}_\mu \in \Omega_\mu. \tag{5.23}$$

  Hence, the space $\mathscr{V} = \mathscr{V}^{\text{Taylor}} \equiv \{\boldsymbol{0}\}$

- Linear:

  This class of boundary assumption is derived by assuming that the micro-cell boundary displacement fluctuations vanish. That is to say, the boundary displacements of RVE are prescribed as

$$\boldsymbol{u}_\mu = \left[\bar{\boldsymbol{F}} - \boldsymbol{I}\right]\boldsymbol{X}_\mu \quad \forall \boldsymbol{X}_\mu \in \partial\Omega_\mu. \tag{5.24}$$

  Hence, the body force field is zero in this case. As, they are the reaction to the prescribed boundary displacements of RVE. Also, the corresponding $\mathscr{V}$ is in the form,

$$\mathscr{V} = \mathscr{V}^{\text{lin}} \equiv \left\{\tilde{\boldsymbol{u}}_\mu \in \tilde{\mathscr{K}^*} | \tilde{\boldsymbol{u}}_\mu = 0 \,\forall \boldsymbol{X}_\mu \in \partial\Omega_\mu\right\} \tag{5.25}$$

- Periodic:

  The macro structure is made of periodic repetition of the RVE. The boundary is decomposed into two parts, Γ_i^+ and Γ_i^-, with outward normals $\boldsymbol{n}_i^+$ and $\boldsymbol{n}_i^-$. Boundary sides of the RVE have been equally sized into pair nodes $\{\boldsymbol{X}_\mu^+, \boldsymbol{X}_\mu^-\}$. For point i,

$$\begin{aligned} \Gamma_i^+ \cup \Gamma_i^- &\in \partial\Omega_\mu, \\ \boldsymbol{n}_i^+ &= -\boldsymbol{n}_i^- \end{aligned} \tag{5.26}$$

  It shows that, each point has a corresponding pair. In this case, the fluctuation displacements are also periodic on the boundary of the RVE. However, the boundary surface tractions are anti-periodic and body force is zero.

  For each pair $\{\boldsymbol{X}_\mu^+, \boldsymbol{X}_\mu^-\}$ the displacement fluctuation fields are,

$$\tilde{\boldsymbol{u}}_\mu(\boldsymbol{X}_\mu^+, t) = \tilde{\boldsymbol{u}}_\mu(\boldsymbol{X}_\mu^-, t) \tag{5.27}$$

  And the space $\mathscr{V}$ is,

$$\mathscr{V} = \mathscr{V}^{\text{per}} \equiv \left\{\tilde{\boldsymbol{u}}_\mu \in \tilde{\mathscr{K}^*} | \tilde{\boldsymbol{u}}_\mu(\boldsymbol{X}_\mu^+, t) = \tilde{\boldsymbol{u}}_\mu(\boldsymbol{X}_\mu^-, t) \,\forall \text{pairs}\{\boldsymbol{X}_\mu^+, \boldsymbol{X}_\mu^-\} \in \partial\Omega_\mu\right\}. \tag{5.28}$$

- Uniform boundary traction:

  Uniform boundary traction is also known as the minimally constrained which

is defined by (5.16) earlier. There is no reactive body force and no restriction on the RVE geometry in this case. Also, the space $\mathscr{V}$ is expressed as,

$$\mathscr{V} = \mathscr{V}^{\text{trac}} = \tilde{\mathscr{K}}^{*} \tag{5.29}$$

Note that, by applying different boundary conditions on a given RVE, the estimation of the corresponding homogenized macro materials are different. That is to say, the Taylor model gives the stiffest solution to the microscopic equilibrium problem, and stiffness is decreasing in order, by the linear boundary displacement, the periodic displacement fluctuation and the uniform boundary traction model.

5.4 Numerical Approximation

The description of the computational implementation of multi-scale constitutive theories of the above type within the non-linear finite element framework is provided.

5.4.1 The Incremental of RVE Equilibrium Problem

First, we will assume the constitutive behavior at the RVE level is expressed by conventional internal variable-based dissipative constitutive theories, whereby the stress tensor is obtained by integrating a set of ordinary differential equations in time for the given strain tensor history, typically using Euler-type difference schemes. For atypical time interval $[t^n, t^{n+1}]$ as described in chapter 3 in more details. The solution to the time-discrete version of equilibrium problem (5.16):

$$\int_{\Omega_\mu} \boldsymbol{P}^{n+1}(\bar{\boldsymbol{F}}^{n+1} + \nabla\tilde{\boldsymbol{u}}^{n+1}, \boldsymbol{\alpha}^n) : \nabla\boldsymbol{\eta}\, \mathrm{d}V = 0 \quad \forall\boldsymbol{\eta} \in \mathscr{V}. \tag{5.30}$$

5.4.2 Finite Element Discretization of RVE Boundary Value Problem

By applying the Finite Element (FE) methods explained in chapter 4 to the RVE problem. The discretized version of the linearized microscopic BVP is in the form,

$$\left\{ \int_{\Omega_\mu^h} \boldsymbol{G}^T \boldsymbol{P}^{n+1}(\bar{\boldsymbol{F}}^{n+1} + \boldsymbol{G}\tilde{\boldsymbol{u}}^{n+1}, \boldsymbol{\alpha}^n)\, \mathrm{d}V \right\}.\boldsymbol{\eta} = 0 \quad \forall \boldsymbol{\eta} \in \mathscr{V}^h \tag{5.31}$$

According to the Hill mandel principle there is no external force vector is involved and Newto-Raphson method is used here to solve for the displacement fluctuation field $\tilde{\boldsymbol{u}}_\mu \in \mathscr{V}^h$.

5.4.3 Multi-Scale Models Finite Element

The construction of the the discretized space of virtual kinematically admissible displacements for multi-scale model $\mathscr{V}^h$ differ from the finite element versions of conventional solid mechanics. Therefore, the discretized $\mathscr{V}^h$ depends on the choice of multi-scale model. The linear boundary condition defines the solution of Newton-Raphson by assigning zero displacement fluctuations on all the degrees of freedom of the boundary of the RVE. This is not the case of the other models.

5.4.4 Discretization of Minimally Constrained Model

The discretization form of the minimally constrained model into a FE framework is as

$$\mathscr{V}^{\mathrm{trac},h} = \left\{ \boldsymbol{\eta} = \begin{bmatrix} \boldsymbol{\eta}_i \\ \boldsymbol{\eta}_b \end{bmatrix} \middle| \int_{\partial\Omega_\mu^h} \boldsymbol{N}_b \boldsymbol{\eta}_b \otimes \boldsymbol{n}\, \mathrm{d}A = 0 \right\}, \tag{5.32}$$

where, $\boldsymbol{\eta}_b$ is the the vector of boundary degree of freedom which contains, free, dependent and prescribed degrees of freedom as

$$\boldsymbol{v}_b = \begin{bmatrix} \boldsymbol{\eta}_f \\ \boldsymbol{\eta}_d \\ \boldsymbol{\eta}_p \end{bmatrix} \tag{5.33}$$

And, $\boldsymbol{\eta}_i$ is the internal degrees of freedom vector.

The matrix form of the integral in equation above can be expressed as,

$$\boldsymbol{C}\boldsymbol{\eta}_b = 0, \tag{5.34}$$

where, $\boldsymbol{C}$ is the constraint matrix and the size of the matrix depends on the finite element dimension. The above equation can be written in the form

$$\begin{bmatrix} \boldsymbol{C}_f & \boldsymbol{C}_d & \boldsymbol{C}_p \end{bmatrix} \begin{bmatrix} \boldsymbol{\eta}_f \\ \boldsymbol{\eta}_d \\ \boldsymbol{\eta}_p \end{bmatrix} = 0, \tag{5.35}$$

To prevent rigid body motion the $\boldsymbol{\eta}_p$ degrees of freedom have to be prescribed. Therefore, the the above equation reduces to

$$\begin{bmatrix} \boldsymbol{C}_f & \boldsymbol{C}_d \end{bmatrix} \begin{bmatrix} \boldsymbol{\eta}_f \\ \boldsymbol{\eta}_d \end{bmatrix} = 0, \tag{5.36}$$

The equation above is used to write $\boldsymbol{\eta}_d$ in terms of $\boldsymbol{\eta}_f$ as,

$$\boldsymbol{\eta}_d = \boldsymbol{R}\boldsymbol{\eta}_f, \quad \text{with} \quad \boldsymbol{R} = -\boldsymbol{C}_d^{-1}\boldsymbol{C}_f \tag{5.37}$$

Consequently, the discrete space of fluctuations displacements of RVE can be redefine as

$$\mathscr{V}^{\text{trac},h} = \left\{ \boldsymbol{\eta} = \begin{bmatrix} \boldsymbol{\eta}_i \\ \boldsymbol{\eta}_f \\ \boldsymbol{\eta}_d \end{bmatrix} \middle| \boldsymbol{\eta}_d = \boldsymbol{R}\boldsymbol{\eta}_f \right\}. \tag{5.38}$$

By applying the same split imposed on $\boldsymbol{\eta}$ to the components of linearized Newton-Raphson method and with the definition of the $\mathscr{V}^{\text{trac},h}$ and that it coincides with the space of admissible displacement fluctuations, equation (5.17) can be expressed as

$$\left\{ \begin{bmatrix} \boldsymbol{F}_i \\ \boldsymbol{F}_f \\ \boldsymbol{F}_d \end{bmatrix}^{(k-1)} + \begin{bmatrix} \boldsymbol{K}_{ii} & \boldsymbol{K}_{if} & \boldsymbol{K}_{id} \\ \boldsymbol{K}_{fi} & \boldsymbol{K}_{ff} & \boldsymbol{K}_{fd} \\ \boldsymbol{K}_{di} & \boldsymbol{K}_{df} & \boldsymbol{K}_{dd} \end{bmatrix}^{(k-1)} \begin{bmatrix} \partial\tilde{\boldsymbol{u}}_i \\ \partial\tilde{\boldsymbol{u}}_f \\ \boldsymbol{R}\partial\tilde{\boldsymbol{u}}_f \end{bmatrix}^{(k)} \right\} \cdot \begin{bmatrix} \boldsymbol{\eta}_i \\ \boldsymbol{\eta}_f \\ \boldsymbol{R}\boldsymbol{\eta}_f \end{bmatrix} = 0 \tag{5.39}$$

By using the above procedure, the system reduces to

$$\begin{bmatrix} \boldsymbol{K}_{ii} & \boldsymbol{K}_{if} + \boldsymbol{K}_{id}\boldsymbol{R} \\ \boldsymbol{K}_{fi} + \boldsymbol{R}^T\boldsymbol{K}_{di} & \boldsymbol{K}_{ff} + \boldsymbol{K}_{fd}\boldsymbol{R} + \boldsymbol{R}^T\boldsymbol{K}_{df} + \boldsymbol{R}^T\boldsymbol{K}_{dd}\boldsymbol{R} \end{bmatrix}^{(k-1)} \begin{bmatrix} \partial\tilde{\boldsymbol{u}}_i \\ \partial\tilde{\boldsymbol{u}}_f \end{bmatrix}^{(k)} = - \begin{bmatrix} \boldsymbol{F}_i \\ \boldsymbol{F}_f \end{bmatrix}^{(k-1)} \tag{5.40}$$

To solve for the internal and free degrees of freedom displacement fluctuations, afterwards, using the relation (5.22) to compute for the dependent degrees of freedom.

5.4.5 Discretization of the Periodic Boundary Fluctuations Model

As mentioned, in periodic boundary condition, each boundary node has a pair, under this assumption, the kinematically admissible fluctuation displacements vectors follows the same procedure described above and is discretized as

$$\mathscr{V}^{\mathrm{per},h} = \left\{ \boldsymbol{\eta} = \begin{bmatrix} \boldsymbol{\eta}_i \\ \boldsymbol{\eta}_+ \\ \boldsymbol{\eta}_- \end{bmatrix} | \boldsymbol{\eta}_+ = \boldsymbol{\eta}_- \right\}, \tag{5.41}$$

where, $\boldsymbol{\eta}_i$, $\boldsymbol{\eta}_+$ and $\boldsymbol{\eta}_-$ are a vector of interior node, positive nodes which belong to Γ^+ and negative nodes belong to Γ^- respectively. To mention that some nodes are prescribed with zero displacement fluctuations to prevent rigid body motion.
According to the above definition and the relation between the space of virtual displacement and the space of displacement fluctuations, the discretization of linearized Newton-Raphson method, the relation (5.26) can be obtained as,

$$\left\{ \begin{bmatrix} \boldsymbol{F}_i \\ \boldsymbol{F}_+ \\ \boldsymbol{F}_- \end{bmatrix}^{(k-1)} + \begin{bmatrix} \boldsymbol{K}_{ii} & \boldsymbol{K}_{i+} & \boldsymbol{K}_{i-} \\ \boldsymbol{K}_{+i} & \boldsymbol{K}_{++} & \boldsymbol{K}_{+-} \\ \boldsymbol{K}_{-i} & \boldsymbol{K}_{-+} & \boldsymbol{K}_{--} \end{bmatrix}^{(k-1)} \begin{bmatrix} \partial\tilde{\boldsymbol{u}}_i \\ \partial\tilde{\boldsymbol{u}}_+ \\ \partial\tilde{\boldsymbol{u}}_+ \end{bmatrix}^{(k)} \right\} \cdot \begin{bmatrix} \boldsymbol{\eta}_i \\ \boldsymbol{\eta}_+ \\ \boldsymbol{\eta}_+ \end{bmatrix} = 0 \tag{5.42}$$

Due to the repetition of the vectors of nodal degree of freedom, the equation above reduces to the linear system of algebraic equations for the unknown vectors $\partial\tilde{\boldsymbol{u}}_i$ and $\partial\tilde{\boldsymbol{u}}_+$,

$$\begin{bmatrix} \boldsymbol{K}_{ii} & \boldsymbol{K}_{i+} + \boldsymbol{K}_{i-} \\ \boldsymbol{K}_{+i} + \boldsymbol{K}_{-i} & \boldsymbol{K}_{++} + \boldsymbol{K}_{-+} \quad \boldsymbol{K}_{+-} + \boldsymbol{K}_{--} \end{bmatrix}^{(k-1)} \begin{bmatrix} \partial\tilde{\boldsymbol{u}}_i \\ \partial\tilde{\boldsymbol{u}}_+ \end{bmatrix}^{(k)} = - \begin{bmatrix} \boldsymbol{F}_i \\ \boldsymbol{F}_+ + \boldsymbol{F}_- \end{bmatrix}^{(k-1)} \tag{5.43}$$

5.4.6 Discretization of the Linear Boundary Displacements Model

In linear model, all the boundary displacements are set to zero. Therefore, the only free degrees of freedom are interior nodes which makes this model simpler than the other two. The discretization of the linear boundary displacements model is given by,

$$[\boldsymbol{K}_{ii}]^{(k-1)}[\partial\tilde{\boldsymbol{u}}_i]^{(k)} = -[\boldsymbol{F}_i]^{(k-1)}, \tag{5.44}$$

which coincides with the conventional FE solution procedure.

Note that, as mentioned earlier, the Taylor model does not require any numerical solution as all the degrees of freedom on the boundaries and in the interior of the RVE are set to zero displacement fluctuations.

5.5 Numerical Examples

In this section numerical examples are presented to show the scope of the described computational strategy above. The first numerical example is validation of the computational multi-scale approach by using the analytical method for porous elastic materials, proposed by [86]. More information is available in details in [93]. The second set of numerical examples focuses on RVEs simulations to show the effect of boundary conditions, topology and distribution of heterogeneities.

5.5.1 Porous Elastic Material

Void volume fraction theory is used to predict the effective isotropic elastic properties of a porous material in both plane strain and stress. The method has been discussed by Nemat-Nasser [93] in more detail. The void volume fraction, f, is the ratio of the sum of the voids volume over the total volume, V_μ, of the RVE. The effective shear modulus $\bar{\mu}$ under the prescribed macro-strain and stress assumption is given as,

$$\begin{aligned} \frac{\bar{\mu}}{\mu} &= 1 - f(k+1) \quad \text{Macro-stress} \\ \frac{\bar{\mu}}{\mu} &= \{1 + f(k+1)\}^{-1} \quad \text{Macro-strain} \end{aligned} \tag{5.45}$$

where,

$$k = \begin{cases} (3-\nu)/(1+\nu) & \text{for plane stress} \\ 3-4\,\nu & \text{for plane strain,} \end{cases} \tag{5.46}$$

Problem Specification and Numerical Results

In this work, we are considering four RVEs with different size of voids as shown in Figure 5.3. The elastic properties of the matrix are, $E = 70$ MPa and, $\nu = 0.2$ for all the models.

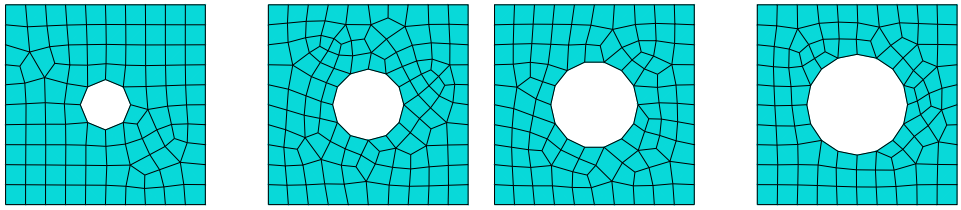

5% void ratio 10% void ratio 15% void ratio 20% void ratio

Figure 5.3: Different RVEs based on various values of void volume fraction (VVF).

The numerical test to obtain the homogenized properties of the micro-structures above, a single square macro-structure is defined with suitable boundary condition and by applying the prescribed displacement on the RVE the variation of the effective shear modulus, $\bar{\mu}$ from multi-scale analysis for different boundary conditions, with respect to the matrix shear modulus, μ, has been plotted in Figure 5.4. And, the results are compared against the prescribed macro-stress and macro-strain based on the void volume fraction theory.

It can be seen that, the Taylor assumption presents the upper bound for the homogenized material properties. The closest curve to the linear displacement boundary assumption is the prescribed macro-stress curve. The results obtained for the periodic boundary displacement fluctuations condition are located between the prescribed macro-stress and macro-strain curves. On the other hand, the softest behavior, which is obtained by the uniform boundary traction assumption, tends to the analytical curve which has been plotted based on the prescribed macro-strain assumption. Hence, the prescribed macro-stress and macro-strain, give the upper and lower limit for the overall elastic material properties for porous media respectively.

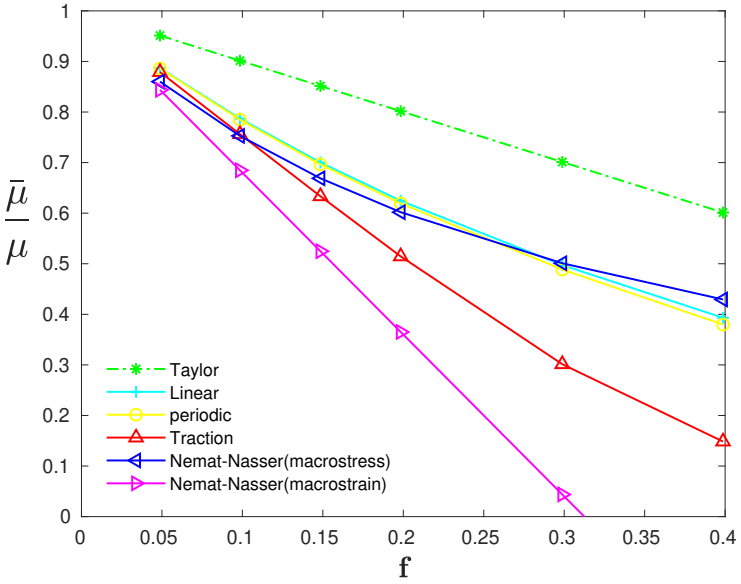

Figure 5.4: Normalized shear modulus for $\nu = 0.2$.

5.5.2 Effect of Cavity Distribution on Homogenized Properties

A unit square RVE cell is considered at the microlevel. The RVE is composed of elasto-plastic material. Two models are taken in this work: First, a RVE with a circular void with radius of 0.1784 which is equivalent to 10% void ratio and located at $\{0.5\,, 0.5\}$. The second model, is made of randomly generated distribution of voids with an overall 10% void ratio. Both models are depicted in Figure 5.5 The

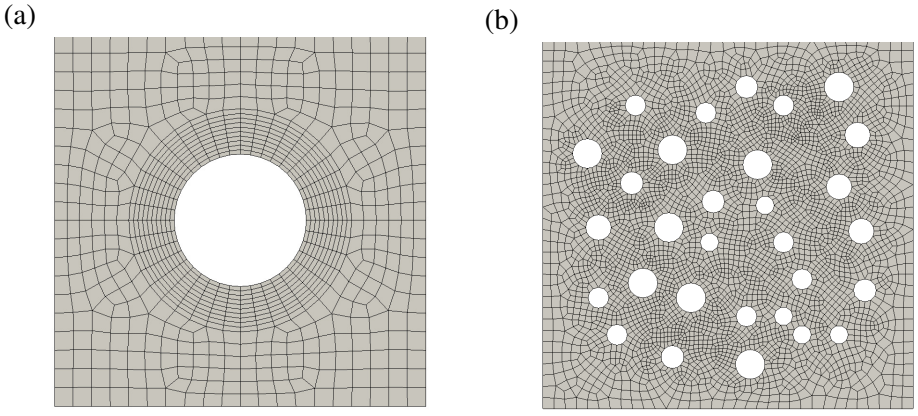

Figure 5.5: RVEs models.(a) regular cavity model and (b) 30 randomly generated voids.

applied finite element for both models is four-node quadrilateral element, a mesh of 788 and 4235 elements is employed for regular cavity and randomly generated model respectively. The matrix for both models is composed of Drucker-Prager elasto-plastic material with associative flow rule. The assigned material properties

are: Young's modulus $E = 3000$ MPa, Poisson's ratio $\nu = 0.3$, both friction and dilatancy angles ϕ and ψ are set to 16.7° and cohesion $c = 1$ MPa.

The simulations in this section have been carried out by employing the computational homogenization under the plane strain assumption in finite strain. The homogenized stress is produced by imposing the macro-deformation gradient over the RVE and solving the microscopic initial boundary value problem for the boundary condition assumed. The imposed macroscopic deformation gradient tensor is expressed by

$$\bar{F} = \begin{bmatrix} 1 & 0.005 \\ 0.005 & 1 \end{bmatrix}$$

The analysis is performed under three different boundary conditions: linear boundary displacements, periodic boundary displacement fluctuations and uniform boundary traction. Figure 5.6 and Figure 5.7 show the deformed mesh and the equivalent plastic distribution (Eps) for all the three different boundary conditions for the RVE with regular cavity and randomly distributed voids respectively. It can be seen that each boundary condition has a different plastic zone pattern. Also, all deformed meshes in Figure 5.6 and Figure 5.7 have been produced with large displacements to visualized the effect of the boundary conditions.

The deviatoric homogenized stress and deviatoric homogenized strain in Figure 5.8, given, respectively as, $q = \sqrt{J_2(\boldsymbol{s}(\boldsymbol{\sigma}))}$, and $\boldsymbol{\varepsilon}_d$.

In Figure 5.8, It can be observed that the RVE with randomly void distribution shows a small difference between the three different boundary conditions and both periodic and uniform traction are closer to the linear boundary condition. This clearly indicates the convergence of the average properties with the increase of the statistical sample representing the heterogeneities at the microlevel [91].

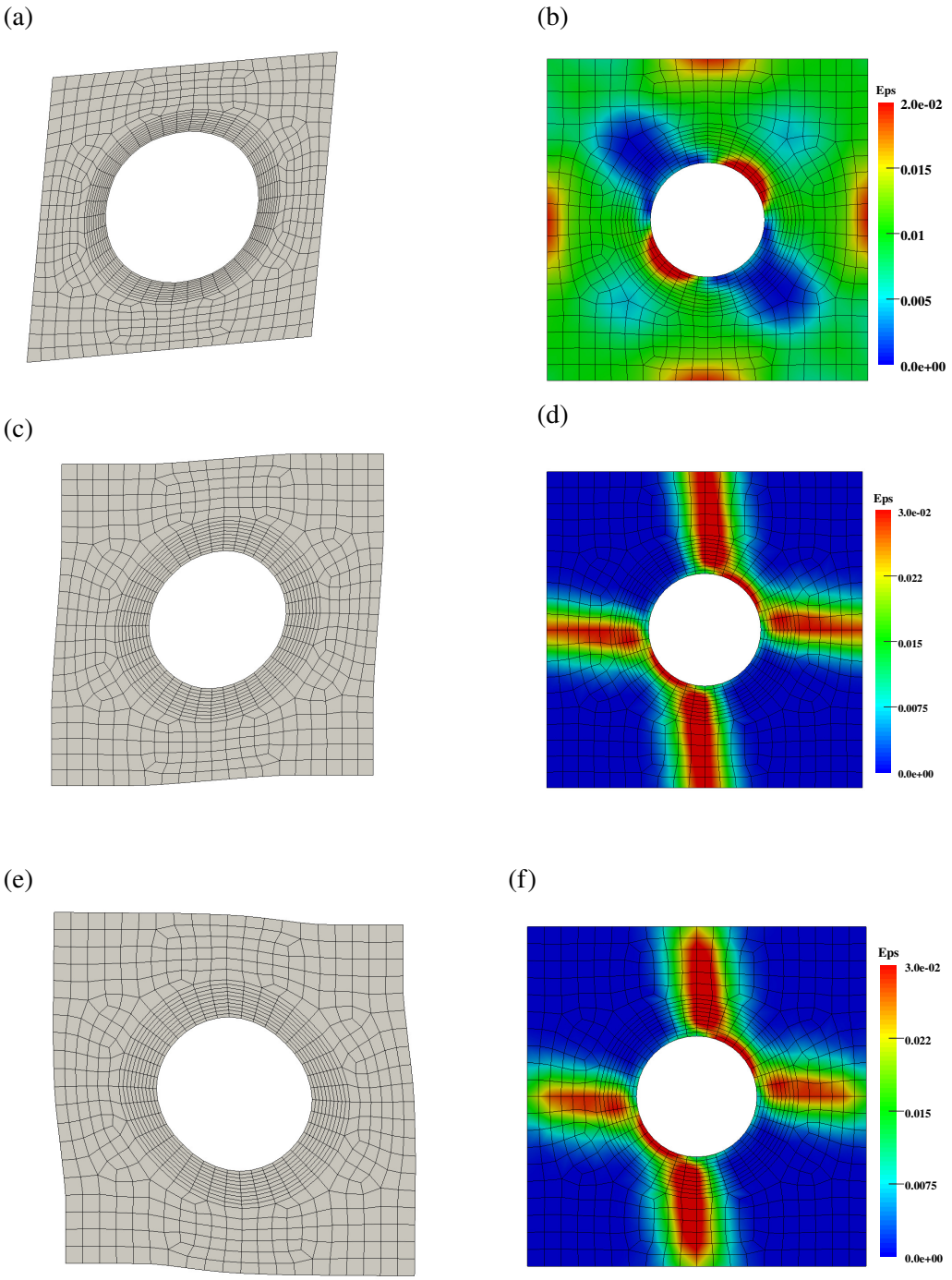

Figure 5.6: RVE with one void at the center: (a) and (b) under linear boundary condition, (c) and (d) periodic condition and, (e) and (f) under uniform traction boundary condition. (a), (c) and (e) are the deformed mesh and (b), (d) and (f) represent effective plastic strain contour plots.

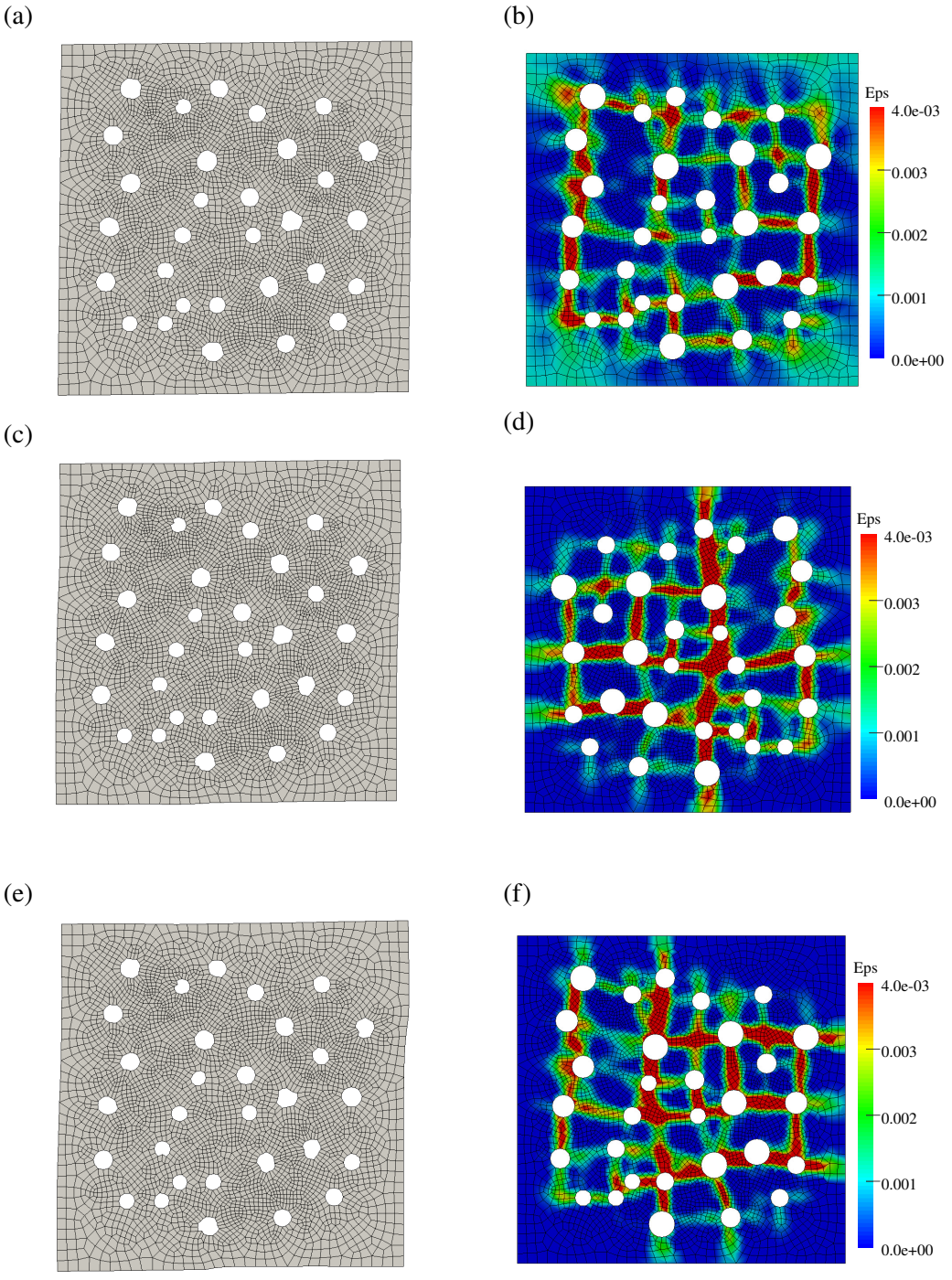

Figure 5.7: RVE with distributed voids:(a) and (b) under linear boundary condition, (c) and (d) periodic condition and, (e) and (f) under uniform traction boundary condition. (a), (c) and (e) are the deformed mesh and (b), (d) and (f) represent effective plastic strain contour plots.

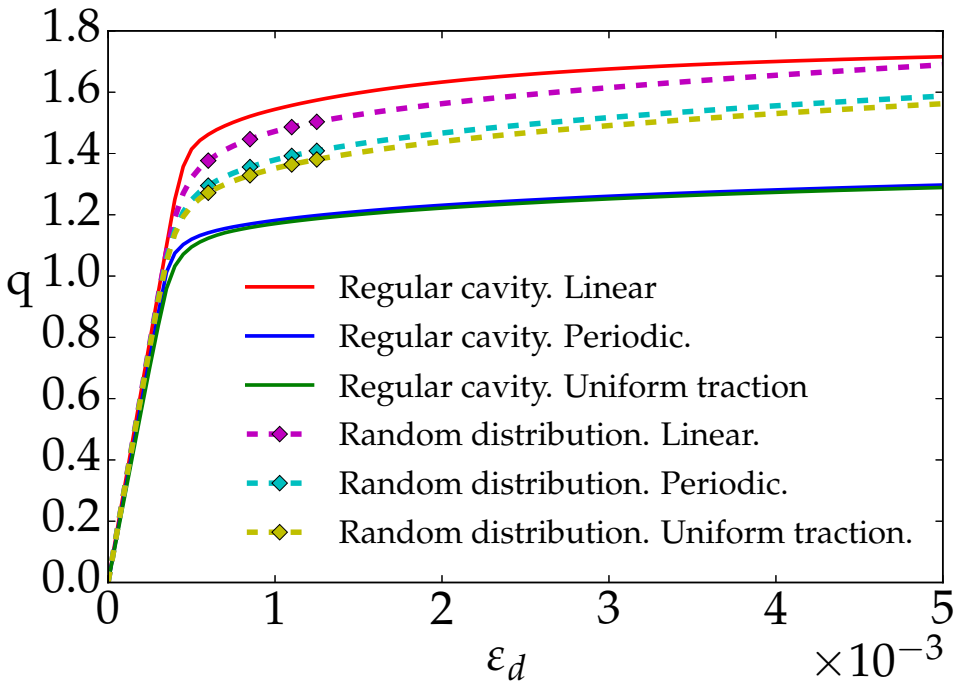

Figure 5.8: Stress–strain curves. Regular cavity model and random cavity distribution model under different RVE boundary conditions.

Chapter 6

A Virtual Testing Strategy to Determine Effective Yield Criteria for Porous Pressure Sensitive Solids

6.1 Introduction

In many practical situations it is necessary to consider several length scales in order to provide predictive modeling of a problem at hand. This situation arises, for instance, in the area of geomechanical analysis of geological problems, where macro scale is commonly of the order of several kilometers, while relevant rock samples that characterize material behavior typically measure several centimeters. Traditional approach of such problems has relied on extensive experimental testing of material samples in order to provide a phenomenological constitutive model to be used in modelling at the macroscopic scale. However, designing an extensive experimental programme can be difficult as samples are often recovered at great expense and scarcely available. There is therefore a need to enhance experimental programme with computationally based techniques.

The present chapter discusses such a computational strategy with objective to construct a constitutive model that may be used in simulation of large scale problems. At the core of such computational strategy is a multi-scale modeling methodology that relies on homogenization of a suitable chosen Representative Volume Elements (RVEs). Since the basic principles for the multi-scale modeling of heterogeneous

materials were introduced (see [94; 95]), this methodology has proved to be a very effective way to deal with arbitrary physically non-linear and time dependent material behavior at micro-level. During the last decade or so various approaches and techniques for the multi-scale modeling and simulation of heterogeneous materials have been proposed. Among these we highlight the contributions by [36], Suquet and co-workers [37; 96], [47], Miehe and co-workers [45; 49; 97], [98], Ladevèze et al. [99], [44] and [88].

The aim is to design a strategy to construct effective yield criteria to be used in simulation at the macroscopic length scale. The effective yield criteria have been successfully constructed for porous materials with elasto-plastic von Mises matrix, starting with the classical work by [100], who first proposed an analytical yield criteria and flow rules for porous ductile media composed of von Mises matrix. Numerous publications have since been contributed on the topic as reported in a review article by [101], which discusses a wide variety of extensions of the original Gurson's model and its applications. Notable recent refinements and extensions of the original model are described in articles by [102], [103], [104], [105] and [106]. A significant practical and research interest exists in characterization of porous materials with pressure sensitive elasto-plastic matrix, which can often be encountered in geomaterials and solid polymers. In early works [107] and [108] extend the Gurson's approach to determine an effective yield criteria for porous materials with elasto-plastic Coulomb and Drucker-Prager matrix, respectively. More recently, a substantial research effort has been invested to provide characterization of porous materials with pressure sensitive matrix for different elasto-plastic constitutive laws and varied void configurations (see, for instance, [109], [110], [111], [102], [112], [113] and [114], and references therein).

The objective of this work is to determine effective yield criteria for porous solids with pressure sensitive matrix by employing a computational homogenization approach following a unified variational formulation described in [92] and [91]. The formulation can be applied to arbitrary materials and provides bounds on the effective material properties for a given choice of the Representative Volume Element (RVE). It has already been successfully applied in prediction of yielding behavior of ductile porous materials with pressure insensitive von Mises matrix (see [115],

[116] and [117]). This chapter describes the first attempt to employ a generic computational homogenization technique in constructing a macroscopic yield criterion for porous material with pressure sensitive Drucker-Prager type matrix.

The overall procedure has many similarities to the approach normally undertaken when performing experimental characterization of the material behavior and is therefore termed the *virtual testing strategy*. Main ingredients of a generic virtual testing strategy have recently been described by [118] and [119], and applied to the construction of the initial yield surface for sheet metal forming operations and heterogeneous composite with von Mises matrix, respectively.

The chapter is organized as follows: Section 6.2 provides a brief summary of constitutive models considered in this work. Main steps of the virtual testing strategy are given in section 6.3, while section 6.4 provides numerical examples and includes comparative analysis against the results available in literature. Finally, the main conclusions and recommendations for future work are discussed.

6.2 Constitutive Models

Pressure sensitive elasto-plastic materials are widely encountered, both as naturally occurring (rocks, soils) and artificially designed (concrete, solid polymers). Hence, characterization of constitutive behavior of such materials has attracted a significant research and practical interest. This section briefly reviews three elasto-plastic yield criteria for pressure sensitive materials, starting with a classical Drucker-Prager yield criterion, and then discusses the constitutive description of two yield criteria that have more recently been proposed to characterize behavior of porous materials with pressure sensitive matrix.

6.2.1 Standard Drucker-Prager Model

The classical Drucker–Prager yield criterion is a simple extension of the von Mises yield criterion, in which pressure sensitivity is introduced through a linear dependence of the yield function on the hydrostatic pressure. Due to its simplicity the Drucker-Prager yield criterion has often been used as a first approximation of pressure sensitive elasto-plastic behavior in wide range of materials such as soils, rock,

concrete, solid polymers, foams, etc. For more details see section 3.2.1 In the space of principal stress the Drucker-Prager yield criterion can be represented as a simple cone as illustrated in Figure 6.1.

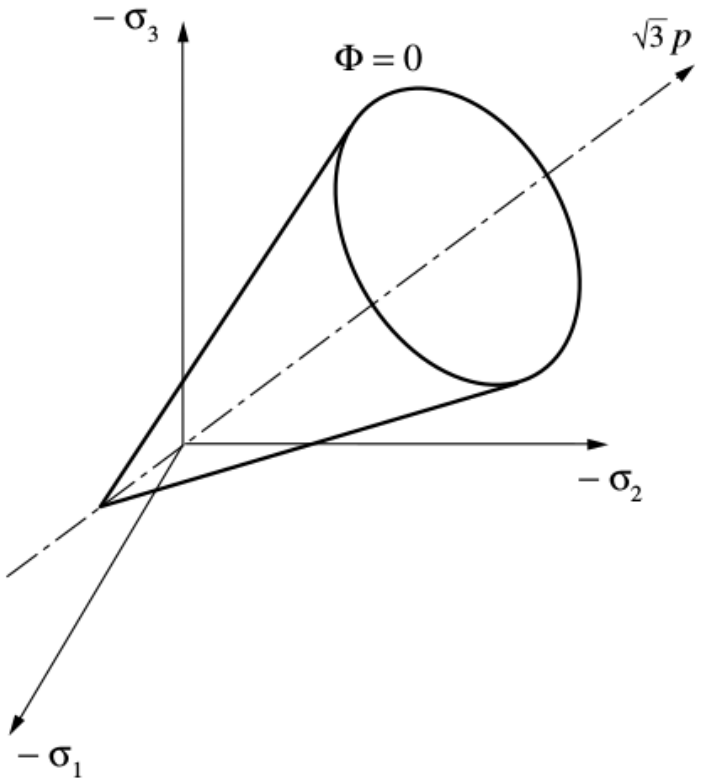

Figure 6.1: Drucker-Prager yield surface in 3D space of principal stresses

6.2.2 Constitutive Model for Porous Solids with Drucker-Prager Elasto-Plastic Matrix

Constitutive description of porous materials with the pressure sensitive elasto-plastic matrix has received some attention. Early work [108] extended the Gurson's approach to determine an effective yield criteria for porous materials with elasto-perfectly plastic Drucker-Prager matrix. More recently, an increased research effort has been invested to provide characterization of porous materials with pressure sensitive elasto-plastic matrix and varied void configurations (see, for instance, [109], [110], [111], [102], [112] and [113], and references therein).

In particular, Shen et al [114] provide a convenient mathematical expression of the macroscopic yield criterion for porous material with Drucker-Prager elasto-plastic

matrix and spherical voids. The macroscopic yield surface is expressed as,

$$\bar{q} = \left\{ \left(-2f\cosh\left(\frac{2M + \text{sign}(\bar{p})}{2M}\ln\left(1 - 3M\bar{p}\right)\right) + 1 + f^2\right)\left[1 - \frac{3M\bar{p}}{(1-f)}\right]^2\right\}^{\frac{1}{2}} \quad (6.1)$$

where $M = \dfrac{\tan(\phi)}{\sqrt{3}}$, f = void ratio , ϕ is friction angle, $\bar{q}$ and $\bar{p}$ are, respectively, deviatoric and hydrostatic stresses normalised by $\sqrt{3}\,c$(cohesion).

The analytical expression (6.1) above is an update of the macroscopic yield surface proposed earlier by [108] and given as

$$\bar{q} = \left\{ \left(-2f\cosh\left(\frac{\frac{3}{2\bar{p}}}{1 - \frac{3M\bar{p}}{(1-f)}} + 1 + f^2\right)\left[1 - \frac{3M\bar{p}}{(1-f)}\right]^2\right\}^{\frac{1}{2}} \quad (6.2)$$

Some differences can be found between the two criteria, especially on the argument of the function "cosh(). Figure 6.2 illustrates the comparison between the yield surfaces respectively predicted by (6.1) (Solid line) and(6.2) (Dashed line) for the case $f = 0.1$ and $M = 0.1$ (the corresponding friction angle is $\phi = 16.7°$.) There is a good agreement between these two surfaces for positive stress triaxialities (tensile mean stresses) and for low negative stress triaxialities (compressive stress states). However, important differences are obtained for high stress triaxialities.

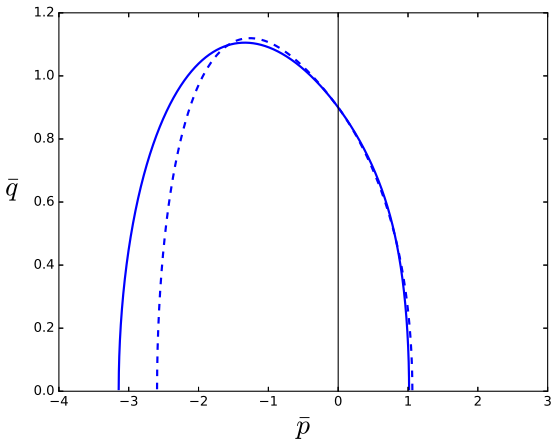

Figure 6.2: Comparison between yield surface given by (6.1) (Solid line) and (6.2) (Dashed line) for frictional angle $\phi = 16.7°$.

6.2.3 The Soft Rock SR4 Model

The SR4 is a generic elastic-plastic critical state constitutive model originally designed to describe porous elasto-plastic materials such as sandstones [56]. The SR4

has proved very successful in description of much larger class of geomaterials and in this work it is employed to the describe macroscopic behavior of heterogeneous elasto-plastic materials with pressure sensitive matrix. See section 3.2.2 for more details.

In order to match the SR4 yield surface with the Drucker-Prager yield shape the g factor (yield surface shape in deviatoric plane) is taken as 1 by setting $\beta_0^\pi = 0$, see equation 3.72. It should be noted that in order to provide accurate representation of material behavior the SR4 yield surface is often combined with a separate flow surface, as shown in Figure 3.2, thus define a non-associative elasto-plastic constitutive law.

6.3 Virtual Testing Strategy

This section discusses a computational strategy, which is designed with an objective to construct a constitutive model that may be used in simulation of macroscopic scale problems. The overall procedure has many similarities with the approach normally undertaken when performing experimental characterization of the material behavior and is therefore termed the *virtual testing strategy*. Main ingredients of a generic virtual testing strategy have recently been described by [118] and [119], and applied to the construction of the initial yield surface for sheet metal forming operations and heterogeneous composite with von Mises matrix, respectively. In this context notable are also recent contributions by [117], [106] and [120].

At the core of a virtual testing strategy is a multi-scale modeling methodology that relies on homogenization of a suitable chosen Representative Volume Elements (RVEs). This work employs a computational homogenization approach that follows a unified variational formulation described in [91] and [92], which is briefly summarized in sections A.1 and A.2. The formulation can be applied to arbitrary materials and has a very useful feature that it provides bounds on the effective material properties for a given choice of the Representative Volume Element (RVE). It should be observed that a virtual testing strategy based on such an RVE formulation has already been successfully applied in prediction of yielding of ductile porous materials with pressure insensitive von Mises matrix (see [115], [116] and

[117]). This article describes the first attempt to employ a virtual testing strategy to construct a macroscopic yield criterion for porous material with pressure sensitive Drucker-Prager type matrix. As will be discussed below, the construction of an effective yield surface for pressure sensitive materials presents unique challenges not faced when employing the von Mises type materials and requires very careful and judicious choices when defining an effective constitutive law.

The main steps of the virtual testing strategy used in this work are illustrated in Figure 6.3. It should be noted that in order to describe the behavior of practically relevant problems, two strategies may be distinguished that correspond to different length scales of the problem at hand. In strategy A the virtual testing strategy provides an effective constitutive law for the behavior of material at microscopic scale. The RVEs size are usually taken as millimetres (mm). The effective constitutive law within the virtual testing strategy is applied directly in simulation of a macroscopic scale problem with size meters or even kilometres (km). In strategy B the virtual testing involves an additional step that provides an effective constitutive law for the behavior of material at mesoscopic scale. Mesoscopic scales are RVEs with high heterogeneities and complex structures and they are bigger in size compares with microscales. Strategy B is employed when significant heterogeneities are present at multiple length scales of material and size of the RVEs in mesoscopic scale are usually taken as centimetres (cm). Both strategies will be discussed in more detail in sections 6.3.1-6.3.3 .

6.3.1 RVE Choice

Two unit cube RVEs are considered for all numerical results generated in section 6.3.1: (i) A cube with a single spherical void at the center, and (ii) a cube with eight variable size randomly distributed spherical voids. The void ratio V_μ^v is kept constant at 10% for all numerical examples. This represents a void volume fraction typical for sandstone. The RVEs are discretized by eight noded hexahedral elements. RVEs are shown in Figure 6.4, with cuts through discretized finite element meshes with void ratio $f = 10\%$ depicted in Figure 6.5. The RVE shown in Figure 6.5(a) is discretized with 106636, while the one in Figure 6.5(b) is discretized with 1567766

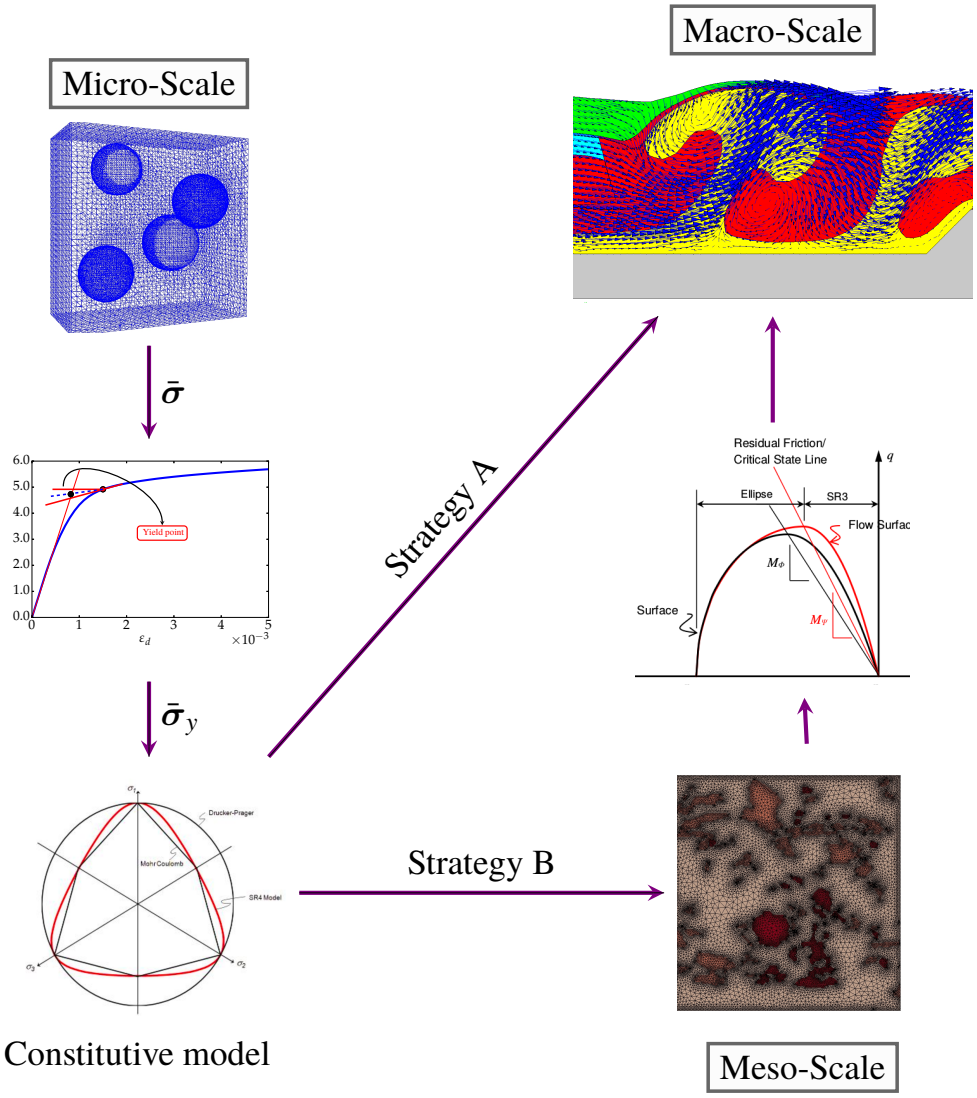

Figure 6.3: Virtual testing strategy.

hexahedral elements.

6.3.2 Yield Criterion Estimate

A crucial aspect of the described virtual testing strategy is identification of the yield stress under different loading conditions. For the RVEs composed of the pressure insensitive von Mises type elasto perfectly plastic material, plastic collapse of the RVE is considered to have occurred when no changes in macroscopic (homogenized) stress are observed for the increasing load factor. This procedure allows a straightforward estimate of the von Mises and hydrostatic components of the macroscopic collapse stress, which define a yield surface point (see [115], [116]

(a) (b)

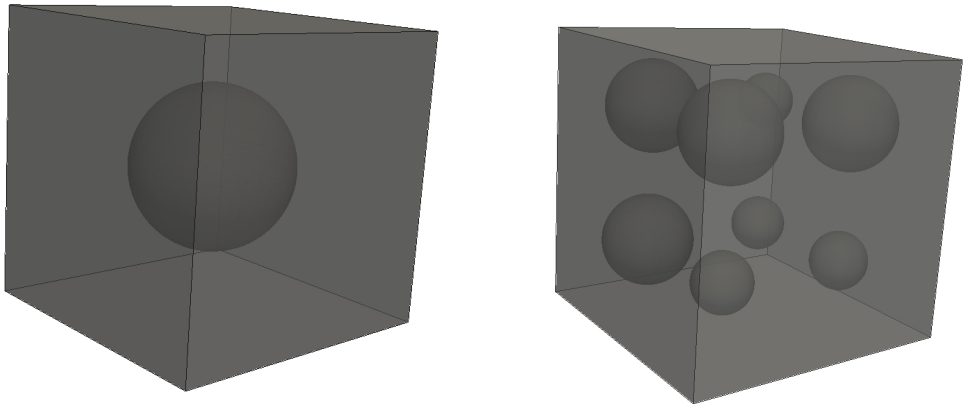

Figure 6.4: RVE models with 10% void ratio.

(a) (b)

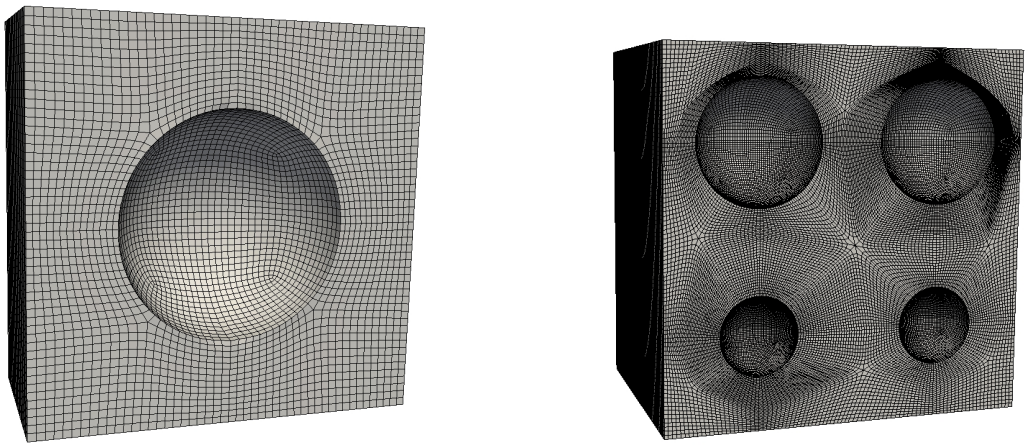

Figure 6.5: RVEs spatial descretization.

and [117] for details of the methodology and examples).

For the RVEs composed of pressure sensitive elasto perfectly plastic materials this has proved to be a more challenging task. While the above procedure is applicable for tensile and shear side of the $p-q$ diagram, the pressure sensitivity of material does not allow a simple estimate of the yield stress at the compressive side of the $p-q$ diagram. In order to overcome the ambiguity and in the spirit of the described virtual testing strategy, in this work the Casagrande method [121] is employed to identify the yield point in $p-\varepsilon_v$ and $q-\varepsilon_d$ diagrams for all loading conditions, where ε_v and ε_d are volumetric and deviatoric strain, respectively. It should be noted that the Casagrande method has originally been proposed to predict

the preconsolidation pressure of soil sample and is nowadays commonly employed to estimate first yield stress during experimental procedure involving soil and rock materials. Graphical illustration of the Casagrande method is given in Figure 6.6. Within the classical Casagrande method the yield stress is identified at the intersect of the linear virgin elastic loading curve and the bisect of a horizontal and tangent drawn at the point on the stress-strain response curve of maximum curvature (see Figure 6.6). This procedure has proved essential in identifying yield stress for the cases when transition between elastic and plastic deformation regime is slow, resulting in a gradual change of slope of the stress-strain curve.

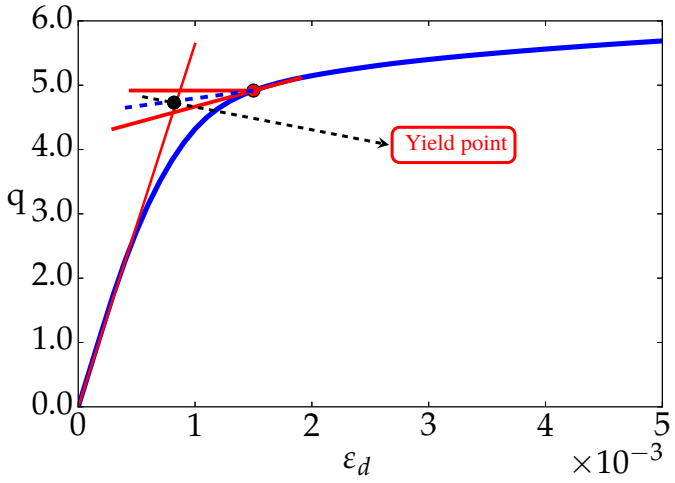

Figure 6.6: Illustration of the Casagrande method.

In order to make sure the method above is the correct choice for our case and, it gives consistent choice of the yield stress, the loading-unloading diagrams are plotted at the different applied strain (see, Figures 6.7 to 6.11). To roughly identify the strain at which the maximum dissipation of the RVE model occurs, we are plotting the plastic dissipation (see equation (6.3)) against time. Note that, the given strain is incremented by $\frac{\varepsilon}{\text{time}} = 0.002$.

The D_p – time diagrams are plotted in case of pure shear for both friction angles $\phi = 16.7°$ and $\phi = 30.2°$ as shown in Figures 6.7(a) and 6.8(a) respectively. It can be seen that, the plastic dissipation is a good procedure to approximately indicate the strain at which to start for the loading-unloading plots.

$$D_p(\varepsilon^p;\xi) = \frac{\sqrt{2\dot{\varepsilon}^p_{ij}\dot{\varepsilon}^p_{ij}}}{\sqrt{1+\mu^2}} \tag{6.3}$$

where, $\dot{\varepsilon}^p_{ij} = \dot{\gamma}\left(\frac{1}{2\sqrt{J_2(\boldsymbol{s}(\boldsymbol{\sigma}))}}\boldsymbol{s} + \frac{\bar{\eta}}{3}\boldsymbol{I}\right)$ and $\mu = \frac{\tan(\phi)}{\sqrt{3}}$.

Figures 6.9(b) to 6.9(d) illustrate the $p-\varepsilon_{\mathrm{v}}$ diagrams in case of triaxial compression for friction angle $\phi = 16.7°$. The loading-unloading are plotted at different strain (increments) according to the plastic dissipation plot. That is to say, loading the RVE at time (increments) where dissipation is low and unloading it, repeating the process for the different increments until the loading-unloading diagram does not change after certain strain. For the friction angle $\phi = 30.2°$ is even more difficult to visualize the yield stress (see Figures Figures 6.10(b) to 6.10(d)). But, the explained method can still be applied. Figure 6.11 illustrates the $p-\varepsilon_{\mathrm{v}}$ and $q-\varepsilon_{\mathrm{d}}$ diagrams under combined loading in compression side with friction angle $\phi = 30.2°$. It can be seen that, adding triaxial shear loading to the triaxial compression, allows a better estimation of the yield stress. Note that, the red line indicates loading and the blue line indicates unloading in the following figures.

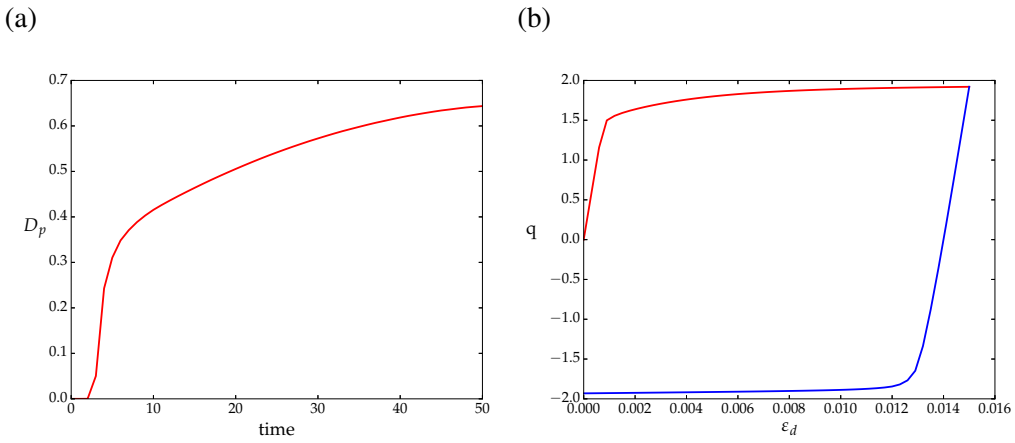

Figure 6.7: Loading-unloading and dissipaton-time curves of the RVE with a spherical void under linear boundary condition for $\phi = 16.7°$, under pure shear: (a) plastic dissipation agaist time and (b) loading-unloading stress-strain.

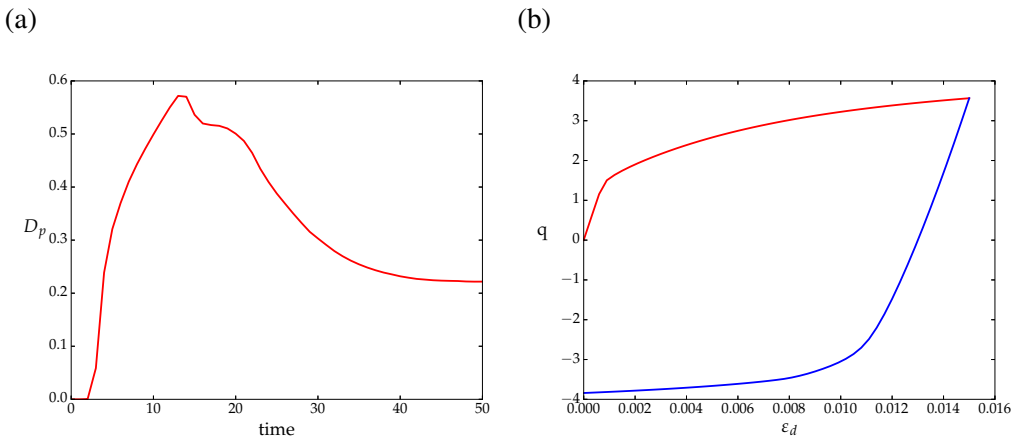

Figure 6.8: Loading-unloading and dissipaton-time curves of the RVE with a spherical void under linear boundary condition for $\phi = 30.2°$, under pure shear: (a) plastic dissipation agaist time and (b) loading-unloading stress-strain.

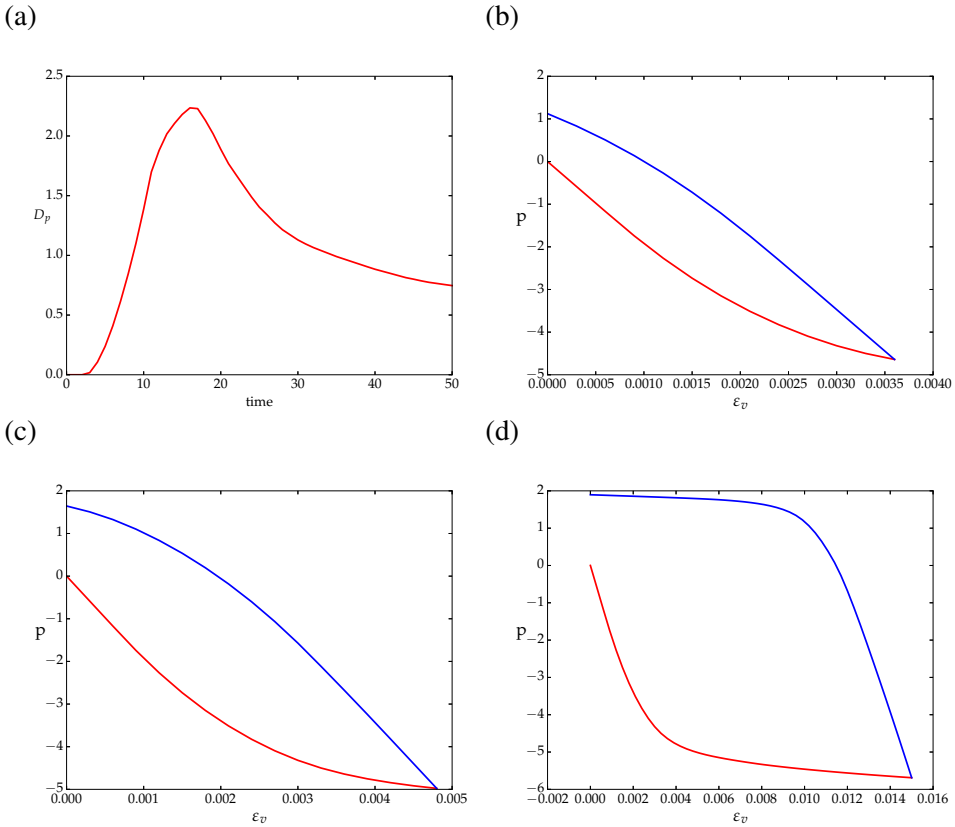

Figure 6.9: Loading-unloading curves of the RVE with a spherical void under linear boundary condition for $\phi = 16.7°$, at different increments under pure compression: (a) plastic dissipation agaist time, (b) unloading before the maximum dissipation, (c) unloading at the maximum dissipation and (d) unloading after the maximum dissipation.

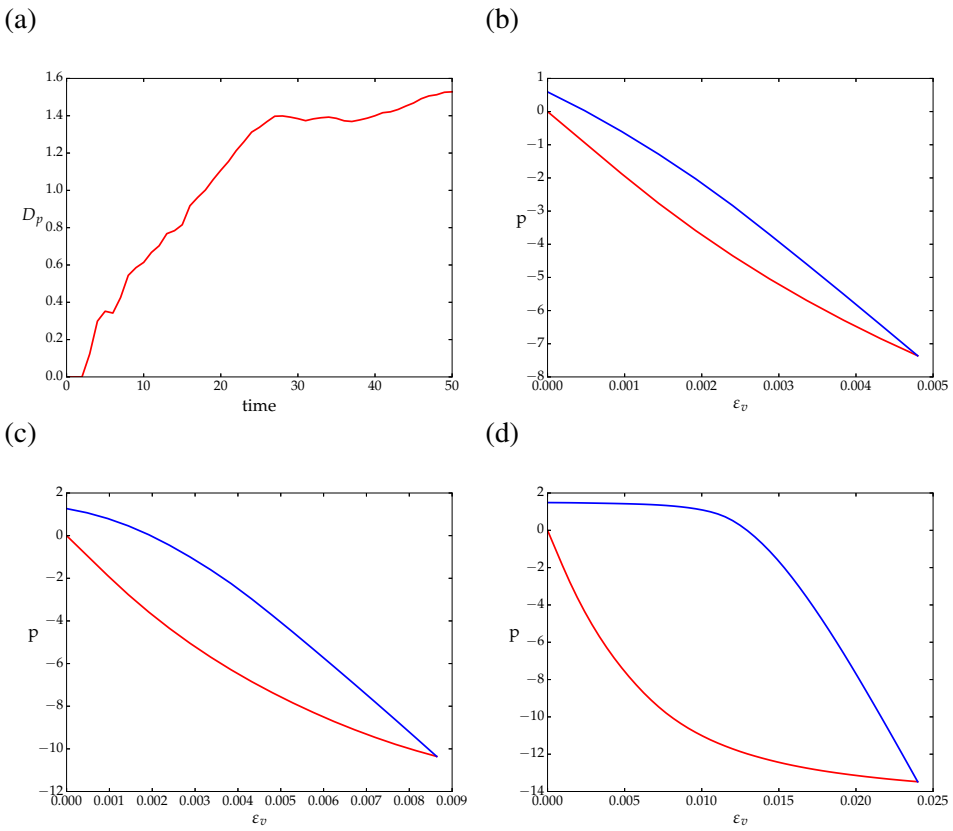

Figure 6.10: Loading-unloading curves of the RVE with a spherical void under linear boundary condition for $\phi = 30.2°$, at different increments under pure compression: (a) plastic dissipation agaist time, (b) unloading before the maximum dissipation, (c) unloading at the maximum dissipation and (d) unloading after the maximum dissipation.

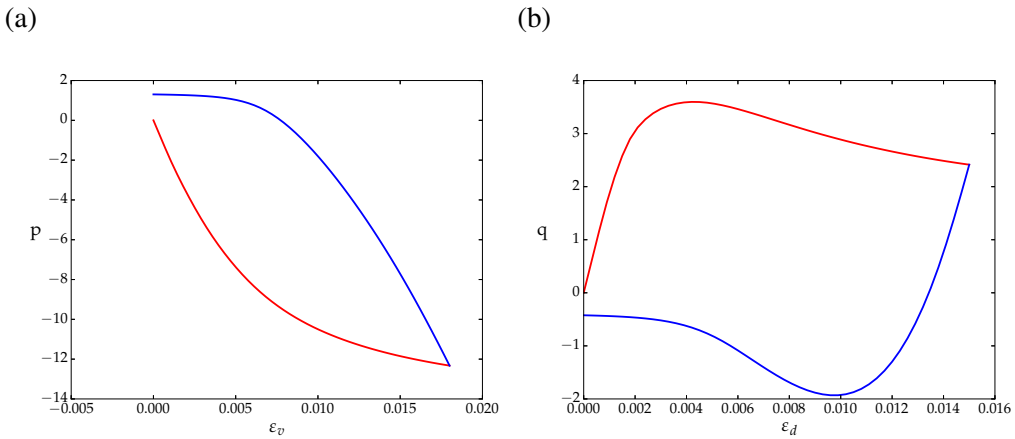

Figure 6.11: The (a) $p-\varepsilon_{\mathrm{v}}$ and (b) $q-\varepsilon_{\mathrm{d}}$ loading-unloading curves for the RVE with a spherical void under linear boundary condition with $\phi = 30.2°$ under combined loading (compression side).

6.3.3 RVE Loading

The loading programme consists in prescribing a macroscopic strain path

$$\varepsilon(\gamma) = \gamma\bar{\varepsilon} \tag{6.4}$$

where γ where is the loading parameter and $\bar{\varepsilon}$ is the strain imposed on the RVEs. In order to construct a yield criterion in the stress space the macroscopic strain $\bar{\varepsilon}$ is varied according to the following rule:

$$\bar{\varepsilon} = \alpha_1 \begin{bmatrix} \frac{1}{200} & 0 & 0 \\ 0 & \frac{1}{200} & 0 \\ 0 & 0 & \frac{1}{200} \end{bmatrix} + \sqrt{1-\alpha_1^2} \begin{bmatrix} 0 & \frac{1}{200} & \frac{1}{200} \\ \frac{1}{200} & 0 & \frac{1}{200} \\ \frac{1}{200} & \frac{1}{200} & 0 \end{bmatrix} \tag{6.5}$$

where $\alpha_1 \in [0, 1]$ for the compressive side of the $p - q$ diagram, while for the tension side the following expression is employed

$$\bar{\varepsilon} = \alpha_2 \begin{bmatrix} \frac{1}{1000} & 0 & 0 \\ 0 & \frac{1}{1000} & 0 \\ 0 & 0 & \frac{1}{1000} \end{bmatrix} + \sqrt{1-\alpha_2^2} \begin{bmatrix} 0 & \frac{1}{200} & \frac{1}{200} \\ \frac{1}{200} & 0 & \frac{1}{200} \\ \frac{1}{200} & \frac{1}{200} & 0 \end{bmatrix} \tag{6.6}$$

in which $\alpha_2 \in [0, 1]$. Note that $\alpha_1 = 0$ and $\alpha_2 = 0$ correspond to a pure shear direction, whereas $\alpha_1 = -1$ corresponds to triaxial compression, while $\alpha_2 = 1$ defines triaxial tension loading. By varying parameters α_1 between -1 and 0 and α_2 between 0 and 1 a sufficient number of yield points can be determined to allow an accurate yield surface to be constructed.

6.4 Numerical Results

Virtual testing strategy described in section 6.3 is employed in this section to construct a macroscopic yield surface for porous pressure sensitive material with Drucker-Prager elasto perefctly plastic matrix. Numerical results are obtained by using an in-house implicit finite element code described in [54] and the commercial finite element software ParaGeo that relies on explicit solution strategy. Numerically generated results are compared against the analytical estimates of yield criteria given by expressions in section 6.2.

In order to generate numerical results the following set of material constants has been selected: Young's modulus, $E = 3000$ MPa and Poisson's ratio, $\nu = 0.3$. Two friction angles are considered, $\phi = 16.7°$ and $\phi = 30.2°$, while cohesion is taken as $c = 1$ MPa. Both friction angles are selected in order to match numerical results with the analytical yield function proposed by [108].

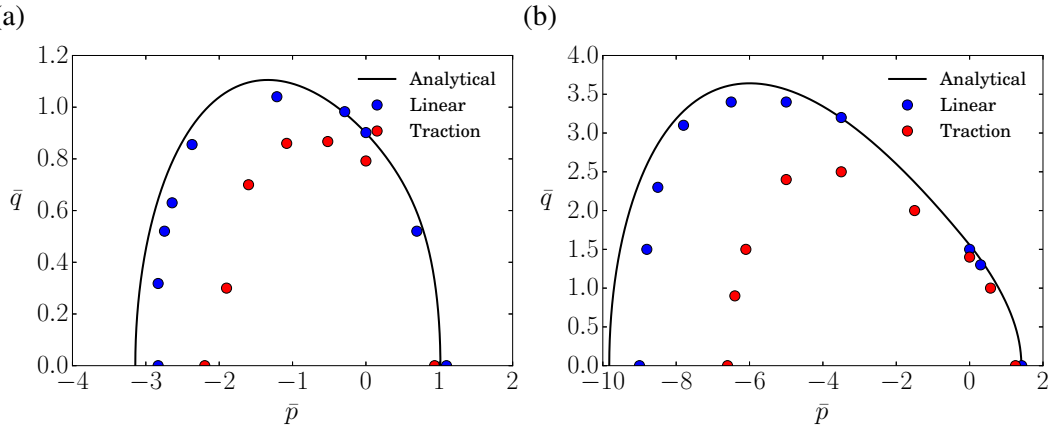

Figure 6.12: Comparison of the analytical solution with the RVE with spherical void at the center under linear and uniform traction boundary conditions under small strain implicit finite element. For friction angles: (a) $\phi = 16.7°$ and (b) $\phi = 30.2°$.

6.4.1 Role of RVE Boundary Conditions

Virtual tests have first been performed for an RVE with a single spherical void in the centre of the RVE, while linear and uniform traction boundary conditions are considered, which are expected to provide upper and lower bound solutions, respectively, as discussed in section 5.3. Virtual testing results are generated by employing an implicit solution procedure and compared against analytical expression given in

equation (6.1). Figures 6.12(a) and 6.12(b) provide, respectively, a comparison between numerical and analytical results for two selected friction angles $\phi = 16.7°$ and $\phi = 30.2°$. It is evident that virtual test results well capture trends observed in $p - q$ diagram for the pressure sensitive elasto-plastic Drucker-Prager material, with linear boundary conditions providing an excellent agreement with analytical expression (6.1) as it is providing a better agreement for high stress triaxialities.

Figures 6.13 and 6.14 depict stress-strain evolution diagrams for both friction angles $\phi = 16.7°$ and $\phi = 30.2°$, respectively. In particular, Figures 6.13(a), 6.13(b), 6.14(a) and 6.14(b) give $p - \varepsilon_v$ evolution diagrams for triaxial compression and tension, respectively, while Figures 6.13(c) and 6.14(c) give $q - \varepsilon_d$ for pure shear loading. The diagrams are used to identify yield stress for each loading combination, clearly illustrating the difficulty in selecting the appropriate value of the yield stress.

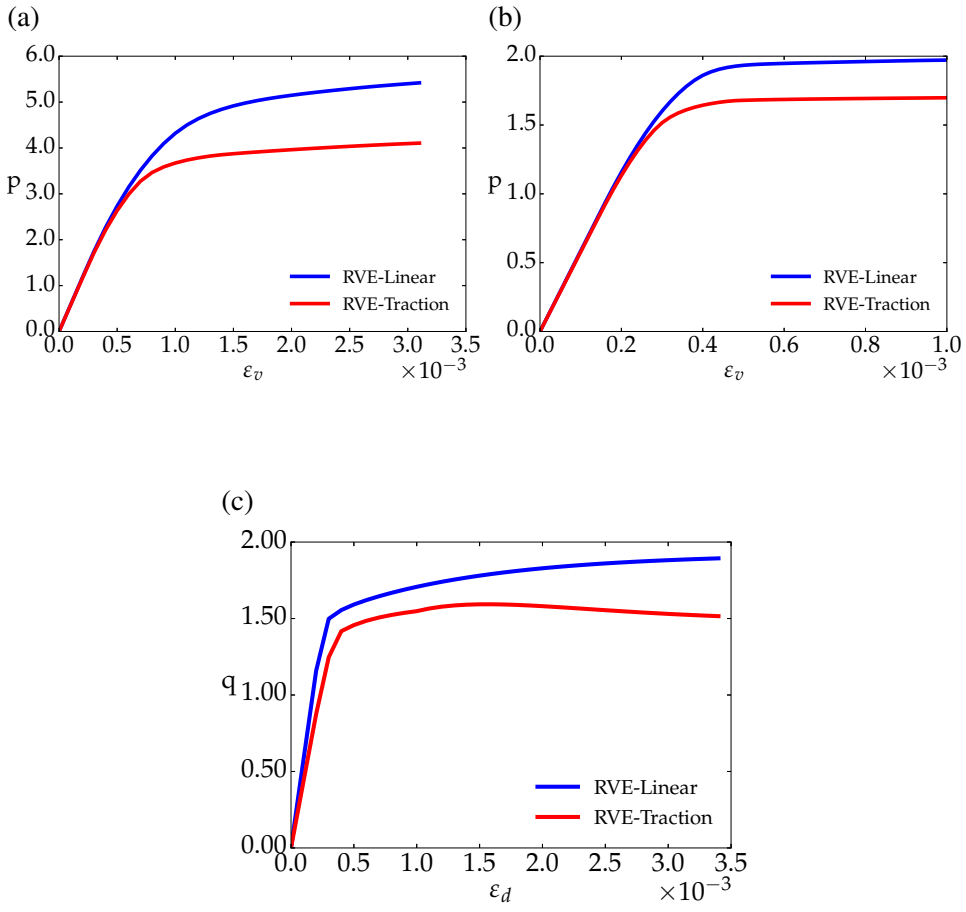

Figure 6.13: Stress-strain curves of the RVE with a spherical void under linear and uniform traction boundary conditions for $\phi = 16.7°$, under different loadings: (a) pure compression, (b) pure tension and (c) pure shear.

They provide a justification for the use of Casagrande method as described in section 6.3.2 to identify the yield stress within the virtual testing strategy. This is particularly evident for larger value of frictional angle $\phi = 30.2°$.

6.4.2 Choice of RVE

In order to illustrate the influence that the choice of RVE may have on constructed yield surface the virtual testing procedure is in this section performed on different RVEs described in section 6.3.1 and given in Figures 6.5 and 6.6. With a view to practical applications the virtual testing strategy described in section 6.3 has been implemented in the commercial software ParaGeo.

Virtual testing results are generated by employing linear boundary condition, which has been shown in previous section 6.4.1 to lead to the yield surface that is in excellent agreement with analytical expression. Figure 6.15 provides a comparison

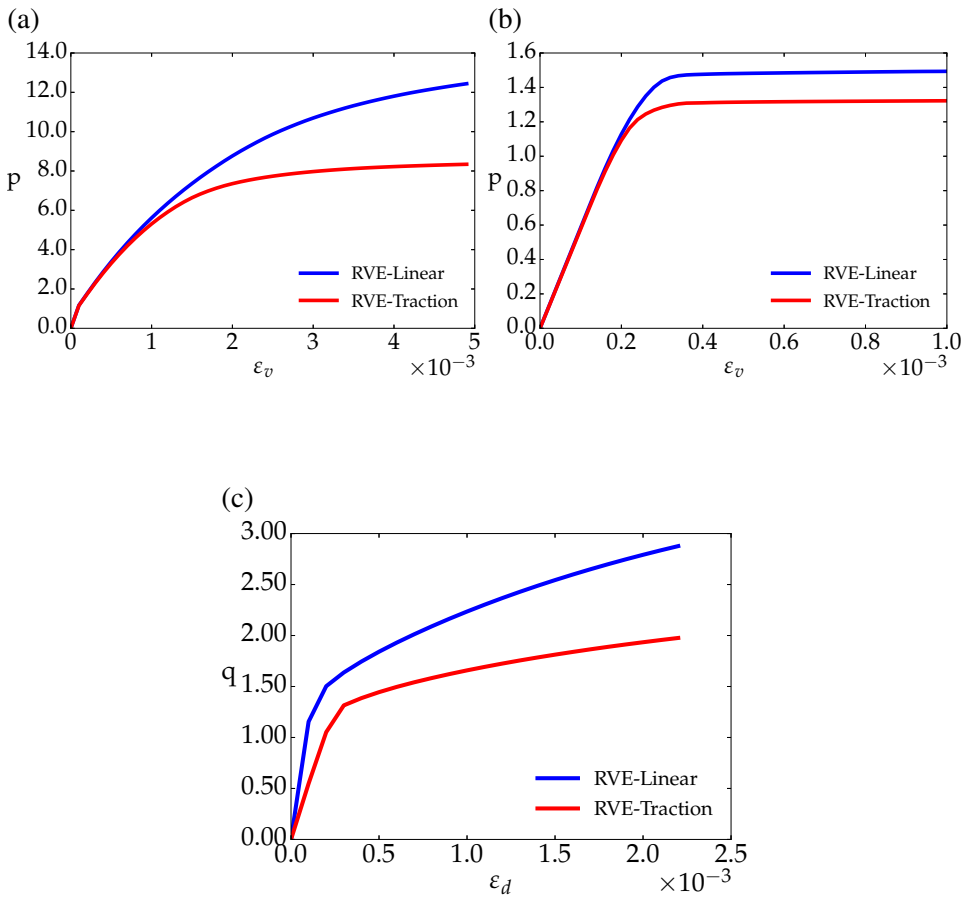

Figure 6.14: Stress-strain curves of the RVE with a spherical void under linear and uniform traction boundary conditions for $\phi = 30.2°$, under different loadings: (a) pure compression, (b) pure tension and (c) pure shear.

between numerically constructed yield surfaces and analytical expression (6.1) for two selected friction angles $\phi = 16.7°$ and $\phi = 30.2°$. It can be observed that virtual testing results show excellent agreement with analytical expression for both choices of RVE, with no significant differences between RVEs with a single and multiple voids. Notably, for friction angle $\phi = 30.2°$ the RVE with multiple voids provides slightly softer response than the RVE with a single void as can be observed by comparing Figures 6.15(b) and 6.15(d).

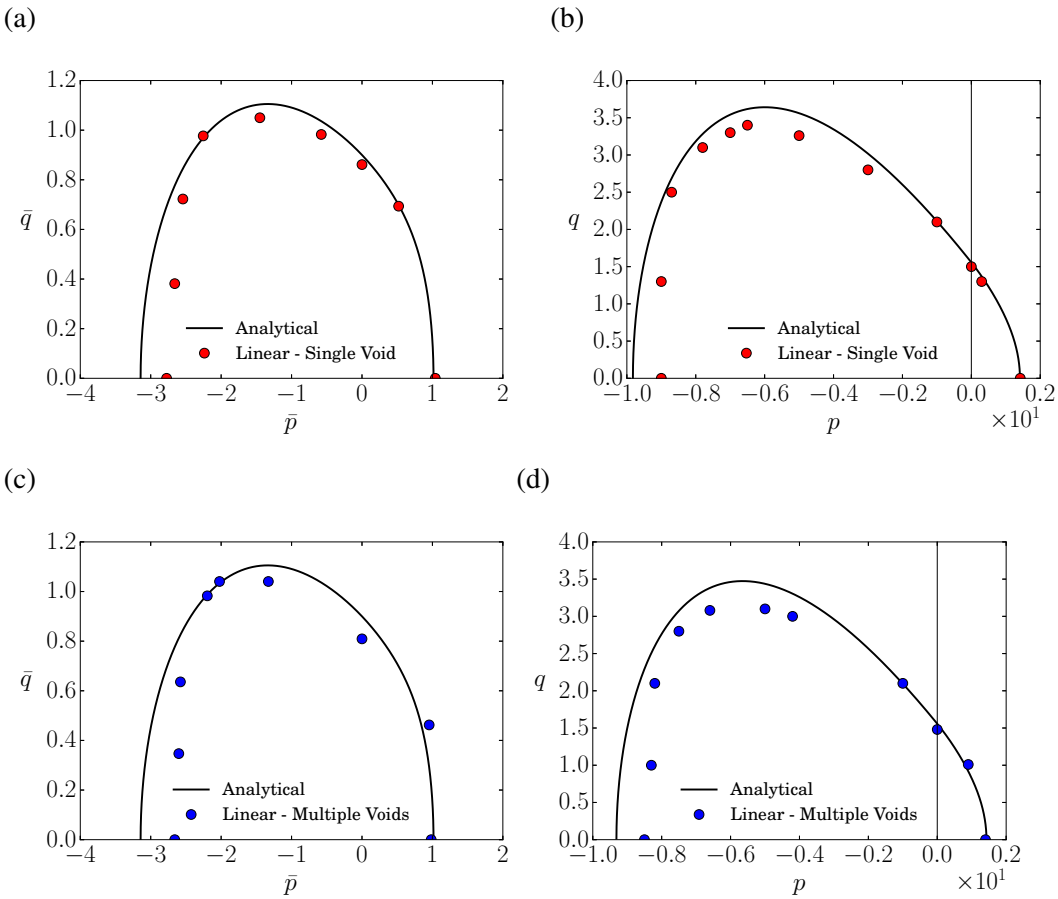

Figure 6.15: Comparison between yield surface predicted by (6.1) solid line and numerical solution. (a) and (c) display results for RVE with single void and eight voids, respectively, with the friction angle $\phi = 16.7°$, while (b) and (d) show results for RVE with single void and eight voids, respectively, with the friction angle $\phi = 30.2°$. All results are obtained by employing ParaGeo.

Figures 6.16(a), 6.16(b), 6.17(a) and 6.17(b) depict stress-strain evolution diagrams for friction angles $\phi = 16.7°$ and $\phi = 30.2°$, respectively. Figures 6.16 and 6.16(b) give $p - \varepsilon_v$ evolution diagrams for triaxial compression and tension, respectively, while Figures 6.16(c) and 6.17(c) give $q - \varepsilon_d$ for pure shear loading. The stress-strain evolution is displayed for an RVE with a single void for both in-house implicit

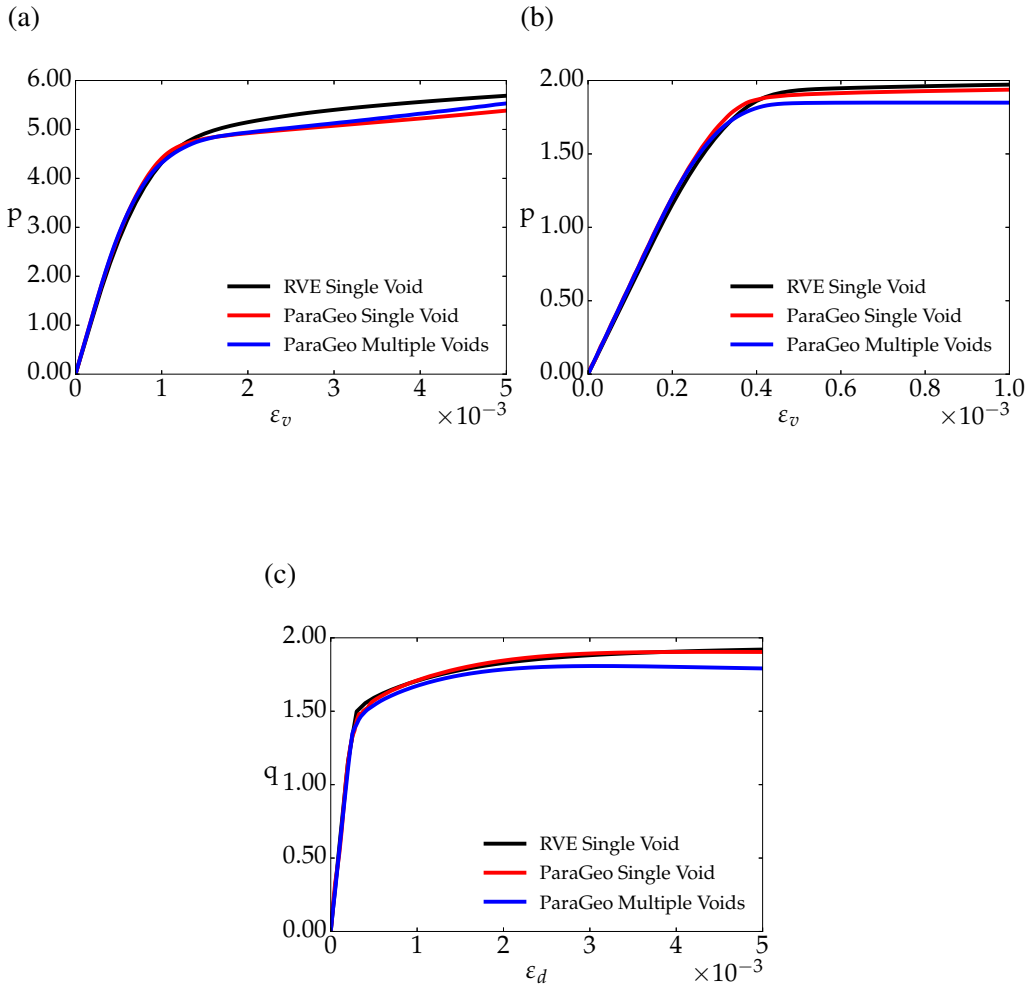

Figure 6.16: Stress-strain curves of the RVE with a single void and multiple voids for linear boundary condition and $\phi = 16.7°$, under different loading conditions: (a) pure compression, (b) pure tension and (c) pure shear.

code and ParaGeo results, while results for RVE with multiple voids are based on ParaGeo simulation. Clearly, the stress-strain diagrams obtained by both codes are providing a good agreement. However, the results could be indistinguishable by improving the meshing and minimising the dynamic factor in explicit ParaGeo code. These diagrams provide typical stress-strain curves that are used to identify yield stress for each loading combination, again clearly illustrating the difficulty in selecting the appropriate value of the yield stress particularly for larger value of frictional angle $\phi = 30.2°$. They provide further justification for the use of Casagrande method as described in section 6.3.2 to identify the yield stress within the virtual testing strategy.

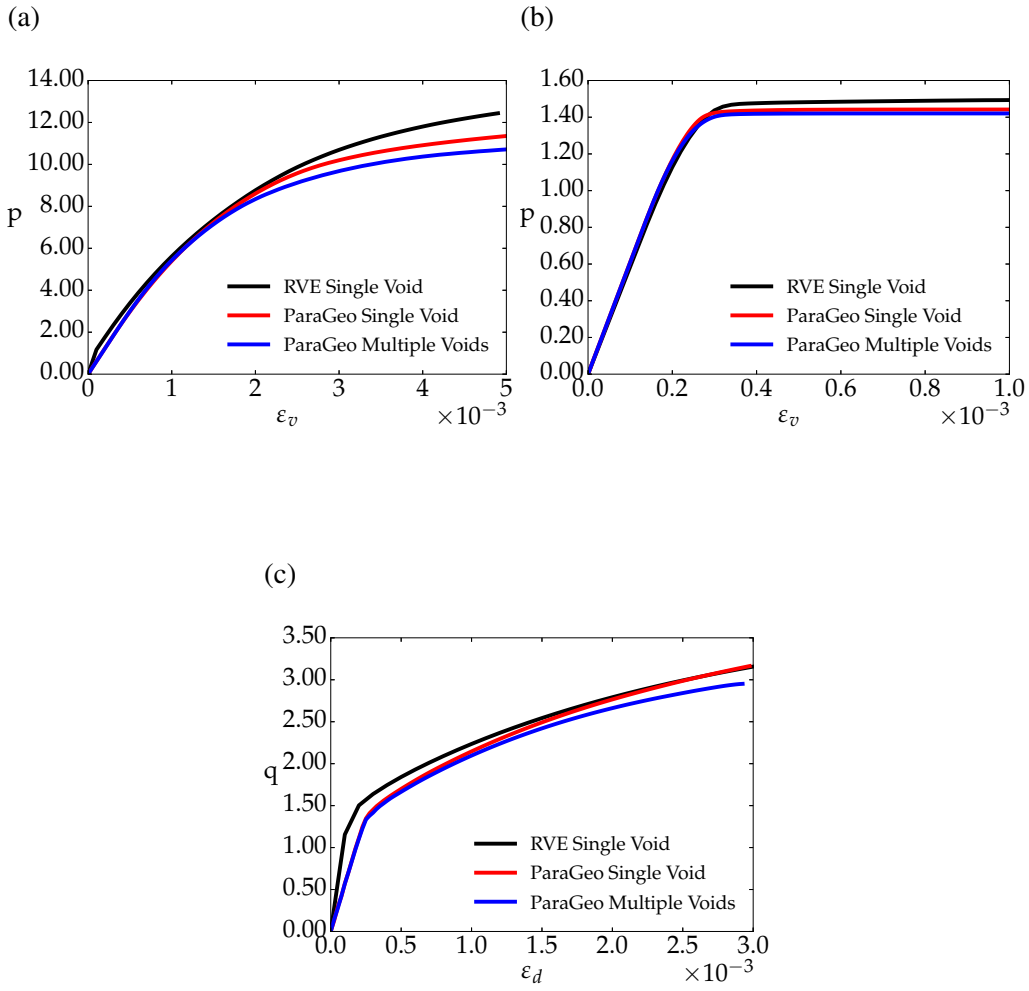

Figure 6.17: Stress-strain curves of the RVE with a single void and multiple voids for linear boundary condition and $\phi = 30.2°$, under different loading conditions: (a) pure compression, (b) pure tension and (c) pure shear.

6.4.3 Mechanisms of Plastic Collapse

In order to get an insight into mechanisms of plastic collapse for porous materials composed of pressure sensitive elasto-plastic matrix, the equivalent plastic strain distribution plots are depicted in Figures 6.18 to 6.20.

Figures 6.18 and 6.20 illustrate the effective plastic strain distribution for the RVEs with a single and multiple voids, respectively, corresponding to the loads at which plastic collapse takes place. The results for the RVE with a single void shown in Figure 6.18 are obtained by imposing two kinematical constraints on the RVE: Figures 6.18(a), 6.18(c) and 6.18(e) depict equivalent plastic strain for linear, while Figures 6.18(b), 6.18(d) and 6.18(f) depict results for uniform traction boundary condition. Similar distributions of equivalent plastic strain can be observed for both

linear and traction boundary conditions, however, the strains at which these levels have been achieved are lower for the uniform traction boundary conditions. This confirms that the uniform traction boundary conditions with minimal kinematical constrains provide a lower bound solution to the plastic collapse of the RVE as clearly illustrated in stress-strain diagrams given in Figures 6.13 and 6.14, and yield surface estimates shown in Figure 6.12.

It can be observed from Figure 6.19 that the plastic collapse for the triaxial loading conditions takes place by development of a plastic deformation in a layer of material surrounding the void (Figure 6.19(c)), which spreads to the boundary causing extensive plastification and collapse (Figure 6.19(d)). This failure pattern is clearly illustrated for triaxial compression in Figures 6.18(a) and 6.18(b) and for triaxial tension in Figures 6.18(c) and 6.18(d). For pure shear loading depicted in Figures 6.18(e) and 6.18(f), the failure pattern starts similarly by development of a plastic deformation in a layer of material surrounding the void, but then spreads diagonally to reach the boundary along the direction of principal tensile stress. This failure pattern is very clearly illustrated for the uniform traction boundary condition depicted in Figure 6.18(f), while the plastic zone appears more diffused for linear boundary condition shown in Figure 6.18(e). Plastic zones for the RVE with multiple voids are illustrated in Figures 6.20 and 6.21, and their development agrees with observations made above for the RVE with a single void.

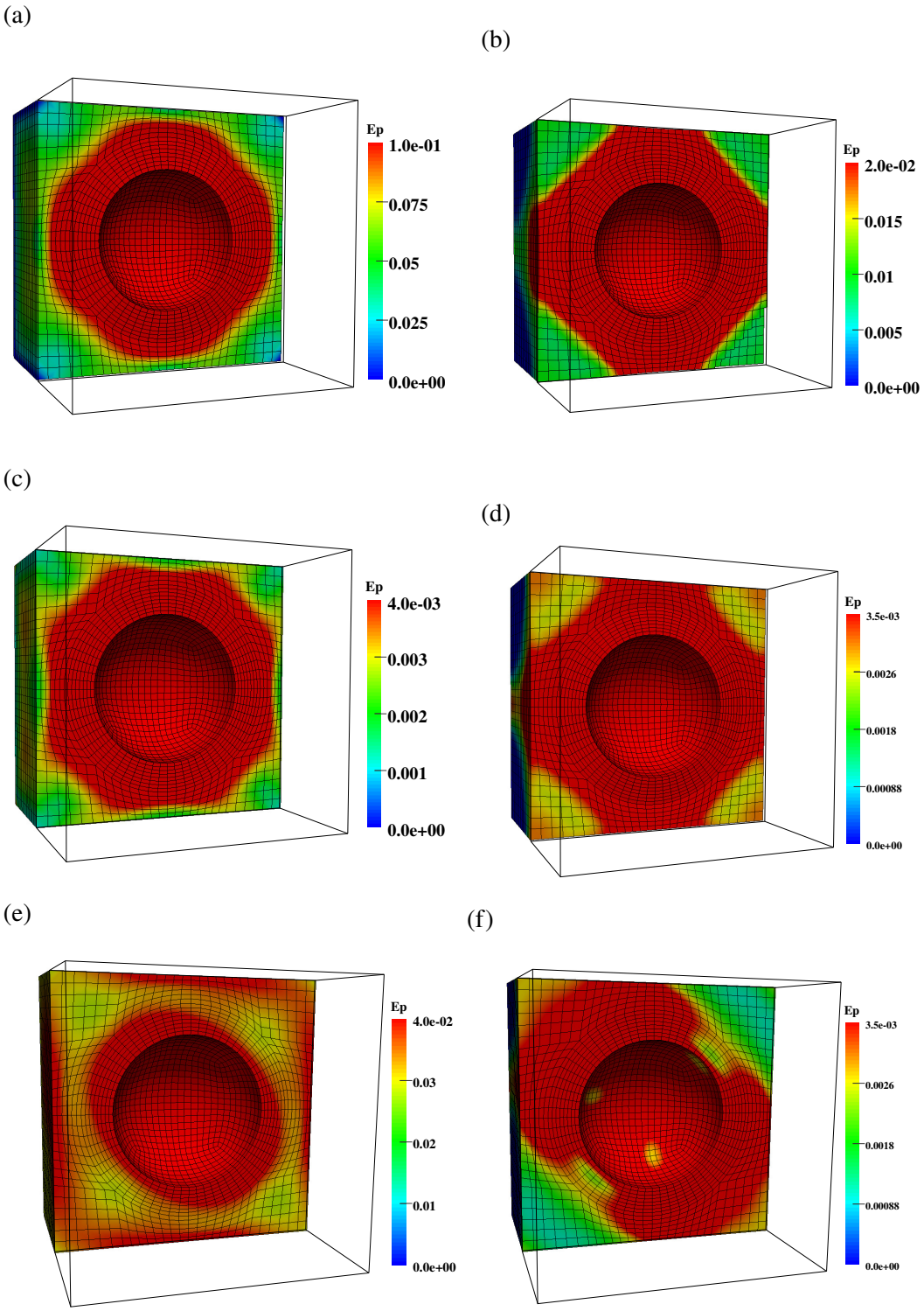

Figure 6.18: Evolution of equivalent plastic strain for the RVE with single void and friction angle $\phi = 16.7°$. (a), (c) and (e) display results under linear boundary condition, while (b), (d) and (f) display results under uniform traction boundary condition. (a)-(b) triaxial compression, (c)-(d) triaxial tension and (e)-(f) pure shear.

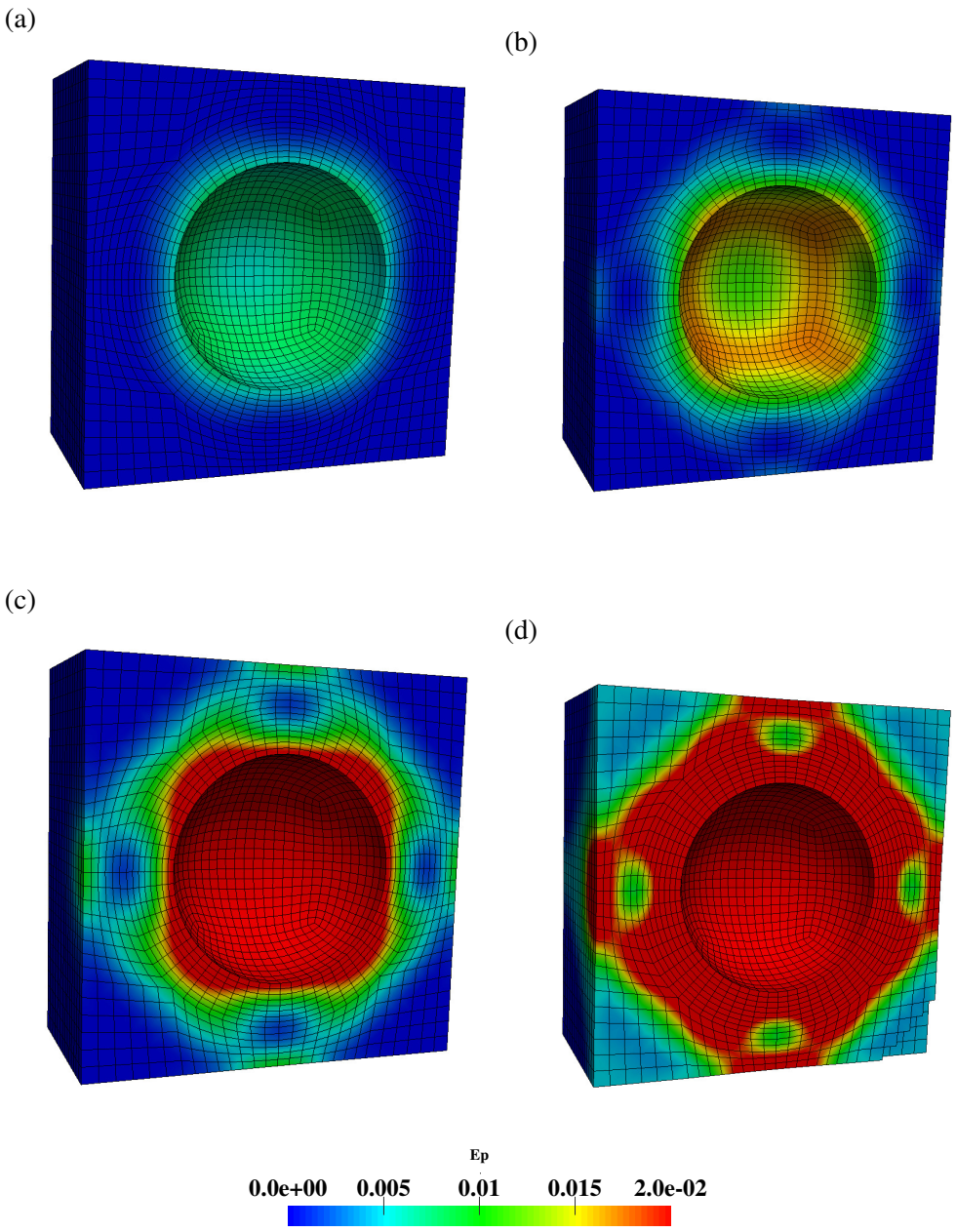

Figure 6.19: Evolution of equivalent plastic strain for the RVE with single void and friction angle $\phi = 16.7°$ under uniform traction boundary condition. Triaxial compression loading at different load levels: (a) 5% of the total load (b) 7% of the total load, (c) 10% of the total load, and (d) 20% of the total load .

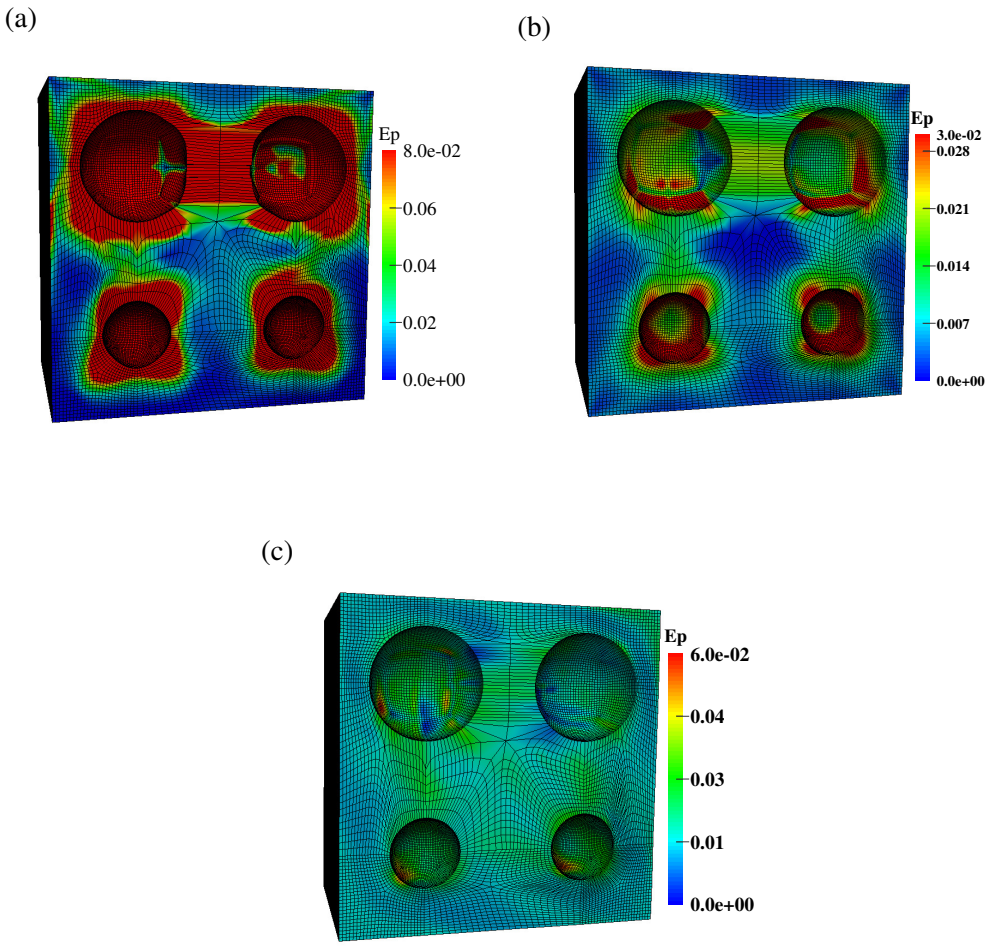

Figure 6.20: Evolution of equivalent plastic strain for the RVE with multiple voids and friction angle $\phi = 30.2°$. (a) triaxial compression, (b) triaxial tension and (c) pure shear.

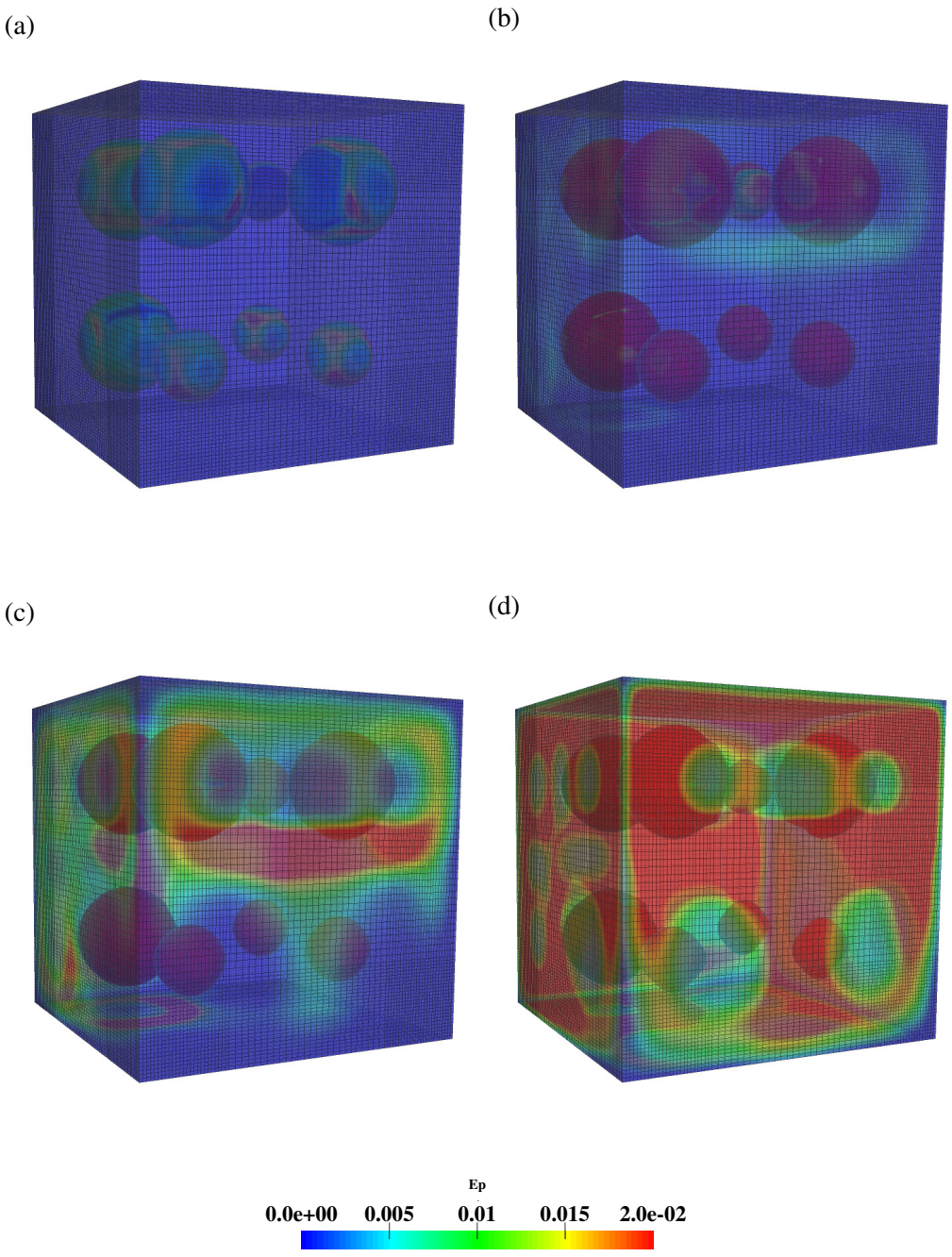

Figure 6.21: Evolution of equivalent plastic strain for the RVE with multiple voids and friction angle $\phi = 16.7°$ under linear boundary condition. Triaxial compression loading at different load levels: (a) 10% of the total load (b) 20% of the total load, (c) 40% of the total load, and (d) 50% of the total load .

6.5 Multi-Scale Application

In order to provide a demonstration of the potential that the described virtual testing strategy, given in section 6.3, can have a wide range of practical applications, this section describes the application of the virtual testing strategy to the realistic soft rock sample. The virtual testing procedure is implemented in the commercial code ParaGeo [122] to allow simulation of large scale problems associated with complex heterogeneous rock microstructure. In order to provide more flexibility in the description of constitutive behaviour the SR4 constitutive model described in section 6.2.3 is employed.

The SR4 model is an extension of the SR3 model proposed by [52], which has proved very successful in simulation of a wide range of problems from geological practice (see, e.g. [56; 123; 124]). The SR4 is a generic critical state model which includes non-associated hardening law and by the appropriate choice of material parameters can provide a close match to the porous Drucker-Prager type elasto perfectly plastic material as shown in Figure 6.22.

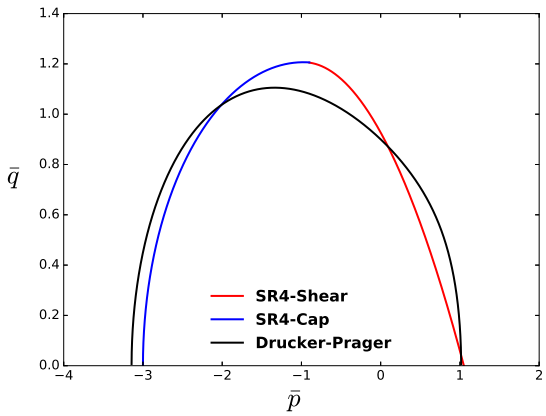

Figure 6.22: Comparison of macroscopic SR4 yield surface with analytical expression for porous elasto-plastic material with Drucker-Prager matrix.

Figure 6.23(a) shows a digital image of a real rock sample typical for a sandstone, which is composed of pressure sensitive elasto-plastic matrix and two types of elastic inclusion particles. Quartz_1 has Young's modulus of $E = 70000$ MPa, while softer Quartz_2 has Young's modulus of $E = 50000$ MPa. The matrix is composed of a porous elasto-plastic material characterized by SR4 constitutive model with Young's Modulus $E = 3000$ MPa, tensile intercept $p_t = 1.5$ MPa, pre-consolidation pressure $p_c = -3.2$ MPa and both friction ϕ and dilation angle ψ

given as $\phi = \psi = 50°$. To fit SR4 materials to Drucker-Prager model, optimisation strategy is used. The digital image is 164 by 169 px and taken from a real sandstone model. The Poisson's ratio $\nu = 0.3$ is used for all materials in the sample. The inclusion ratio of the sample stands at 17%. The discretised model depicted in Figure 6.23(b) is meshed with 65648 triangular elements.

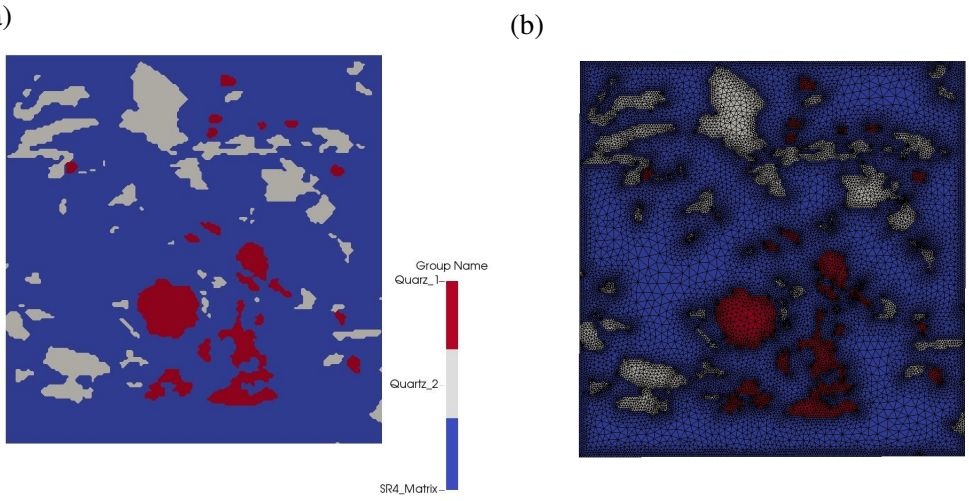

Figure 6.23: Sandstone RVE: (a) digital image, (b) finite element mesh.

Figure 6.24 depicts stress-strain evolution diagrams for characteristic loading conditions. Figure 6.24(a) and Figure 6.24(b) give $p - \varepsilon_v$ evolution diagrams for compression and tension loading, respectively, while Figure 6.24(c) give $q - \varepsilon_d$ for pure shear loading. The diagrams Figures 6.24(a) to 6.24(c) provide typical stress-strain curves that are used to identify yield stress for each loading combination, again clearly illustrating the importance of using the Casagrande method described in section 6.3.2 to identify the yield stress within the virtual testing strategy.

Figure 6.25 illustrates the effective plastic strain distribution corresponding to the loads at which plastic collapse takes place. It can be observed from Figures 6.25(a) and 6.25(b) that the plastic collapse for both compression and tension dominated loading conditions takes place by development of large plastic deformations at the interface between hard particles and soft rock matrix, which them spreads to the boundary leading to extensive plastification and rock sample collapse. For shear loading depicted in Figure 6.25(c), the failure pattern starts similarly by development of a plastic deformation at the interface between hard particles and soft rock matrix, but then spreads by formation of shear bands that reach the boundary leading to

plastic collapse.

Figure 6.26 depicts a set of yield points recovered by virtual testing procedure and numerically constructed yield surface. The yield surface is obtained by employing the SR4 constitutive model and an appropriate choice of material parameters that provides the best fit to the set of yield points. The yield surface constructed in such a way defines the meso-scale type constitutive model, which, within the virtual testing strategy - type B (see Figure 6.3), provides a constitutive model to be used for numerical simulations at the macro-scale.

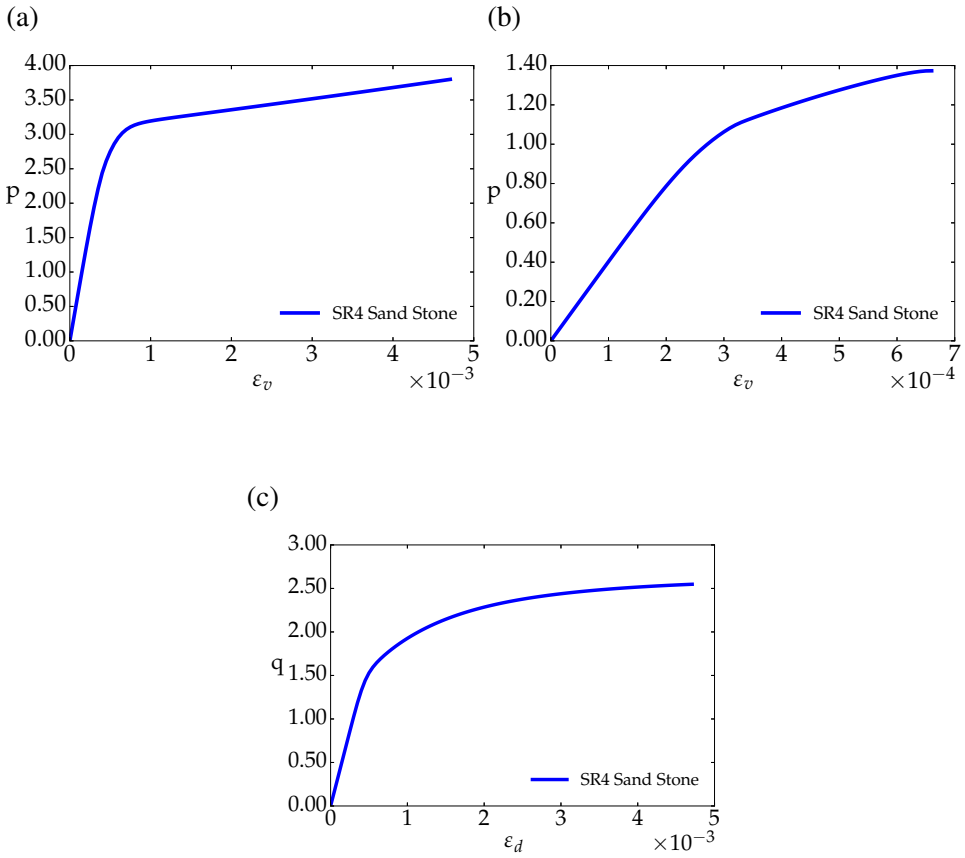

Figure 6.24: Stress-strain curves of the sandstone RVE under different loading conditions: (a) compression, (b) tension and (c) shear.

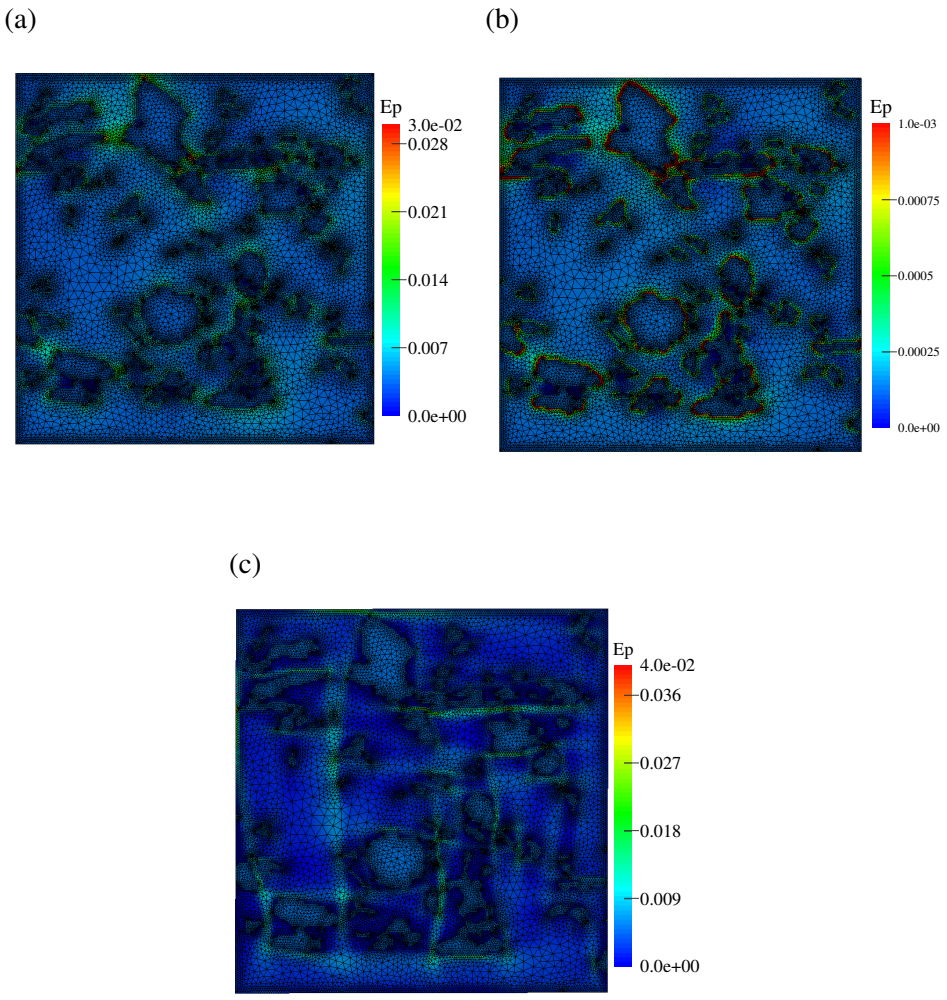

Figure 6.25: Equivalent plastic strain distribution for the sandstone RVE under different loading conditions: (a) compression, (b) tension and (c) shear.

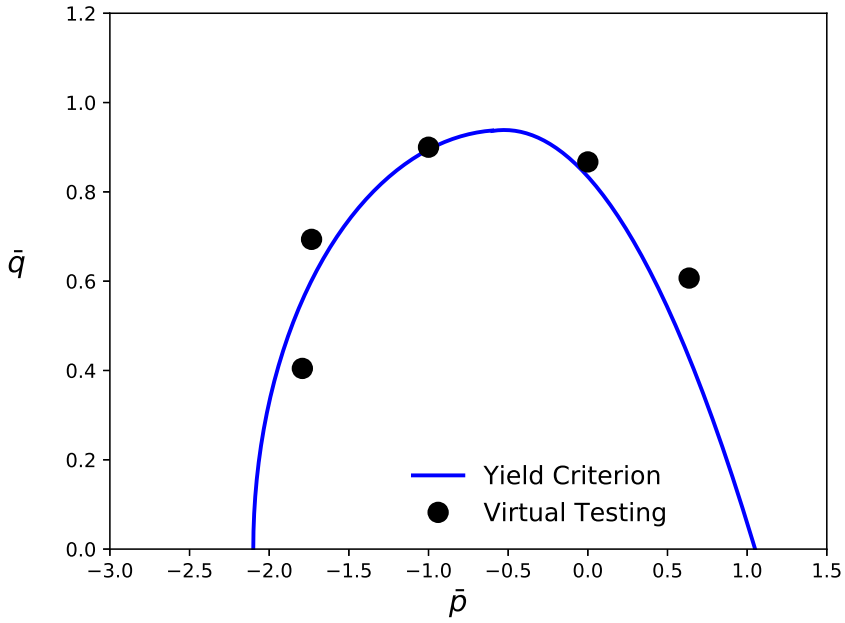

Figure 6.26: Set of yield stress points together with yield surface constructed by the virtual testing procedure.

6.6 Concluding Remarks

Virtual testing strategy has been developed in this work based on computational homogenisation approach following a unified variational formulation. The potential of the strategy is illustrated by performing estimate of the effective properties of porous solid with elasto-plastic Drucker-Prager matrix. Excellent correspondence has been demonstrated between the computationally generated effective yield criteria for porous solids and the recently proposed analytical estimates for Drucker-Prager type solids and the SR4 constitutive model for soft rocks. Animportant feature of the proposed virtual testing strategy is use of the Casagrande procedure ([121]) to identify yield points and thus to construct an effective yield surface for heterogeneous elasto-plastic matariels. This procedure is commonly employed in experimental characterisation of geological materials that invariably display appreciable pressure sensitivity. A range of numerical tests performed in this work demonstrates that the virtual testing strategy enhanced by the Casagrande procedure provides an efficient and accurate methodology for constructing yield surface for a wide range of realistic geological materials.

The virtual testing procedure has been implemented in the commercial code ParaGeo ([52]) to allow simulation of large scale problems associated with complex

heterogeneous rock microstructures. In order to illustrate the potential that the developed virtual testing strategy may have on characterisation of practically relevant materials, the effective yield surface has been constructed for the realistic soft rock sample based on a digital image of a sandstone.

Chapter 7

Effective Yield Criteria for Layered Composite Model

Sedimentary rock and underground salt usually consist of a series of parallel layers. The thickness of these layers can vary between millimetres to meters with the properties of the layers changing with either symmetric or non-symmetric pattern. Both theoretical and experimental approaches have been carried out by several researchers, e.g., ([118; 119]) to provide the equivalent properties of such a layered system.

In this work, computational homogenization methodology is applied to these layered systems to obtain effective macroscopic yield failure surface.

The first section provides computational yield surface of the composite layered system in deviatoric-pressure stress diagram. The effective yield surface is obtained under both periodic and uniform traction boundary conditions. The details of the set-up of the virtual laboratory are also introduced with some numerical examples. In the second section, the numerically generated effective yield surfaces for 2-D composite layered system under plane stress assumption are obtained. The predicted computational yield surfaces are presented in principal stresses. Finally, based on the numerical simulations, the closest fit to the proposed analytical yield functions by Hill [18] and Hoffman [51] are obtained. The details of the set-up of the numerical simulations are provided.

7.1 Effective Anisotropic Yield Surface of a Layered Composite Model

In this example, we perform homogenization in small strain analysis of three uniform layers which represent a rock-salt model. As shown in Figure 7.1, a unit cubic rectangular model is made of three uniform layers. Each layer is modeled by a von-Mises type perfectly plastic elasto-plastic law with different material properties. The material properties for each layer are given as;

$$\begin{aligned} &\text{Group\_1}: \quad \sigma_y = 10 \text{ MPa}, \ E = 25000 \text{ MPa}, \ \text{and } \nu = 0.3 \\ &\text{Group\_2}: \quad \sigma_y = 2 \text{ MPa}, \ E = 5000 \text{ MPa}, \ \text{and } \nu = 0.25 \\ &\text{Group\_3}: \quad \sigma_y = 15 \text{ MPa}, \ E = 45000 \text{ MPa}, \ \text{and } \nu = 0.38 \end{aligned} \tag{7.1}$$

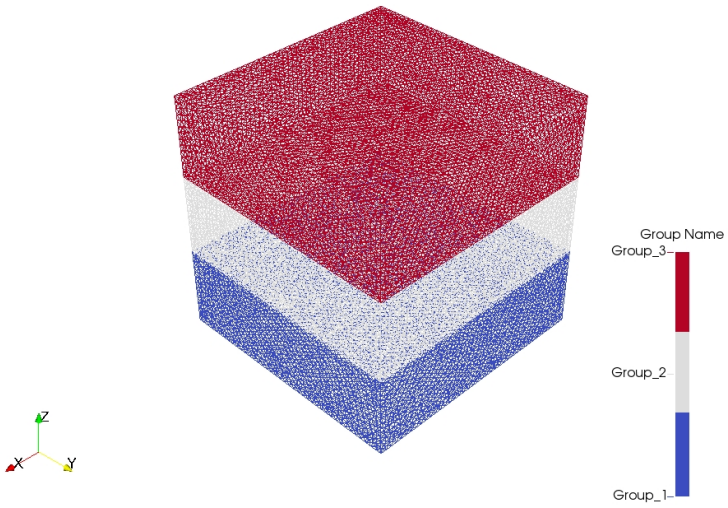

Figure 7.1: Geometry of a 3D layered composite model.

The loading consists in prescribing a macroscopic tri-axial shear strain and changing the macroscopic tri-axial pressure. The macroscopic strain imposed on the model is given as,

$$\bar{\varepsilon} = [\alpha(\frac{1}{100}, \frac{1}{100}, \frac{1}{100}), 0.005, 0.005, 0.005] \tag{7.2}$$

By varying the load $0 \leq \alpha \leq 1$, the above array fully covers the loading spectrum. In the following section, we are providing the macroscopic pressure and deviatoric strain under both linear and uniform traction boundary conditions.

7.1.1 Effective Anisotropic Yield Surface under Linear Boundary Condition.

In this section, the equivalent plastic strain and the variation of the stress against strain under linear boundary condition are represented. As illustrated in Figures 7.2(a) and 7.2(b), the yield point is clear in case of pure shear and equivalent plastic strain is distributed over the layers respectively. However in case of pure compression, the equivalent plastic strain is localized and the yield point can not be selected precisely (see Figure 7.3).

In order to show the macroscopic yield surface of the layered system in $p - q$ diagram, we are applying the macroscopic loading in equation (7.2) on the composite layer. Some of the $q - \varepsilon_d$ plots are shown in Figure 7.4 for different imposed compression. It can be seen that, the stress at failure is lower when the compressive stress increases. The reduction of the failure stress is limited to only relatively small value of compression soon afterwards the failure stress remains constant. The macroscopic yield surface for the von-Mises material type is represented in Figure 7.5 .

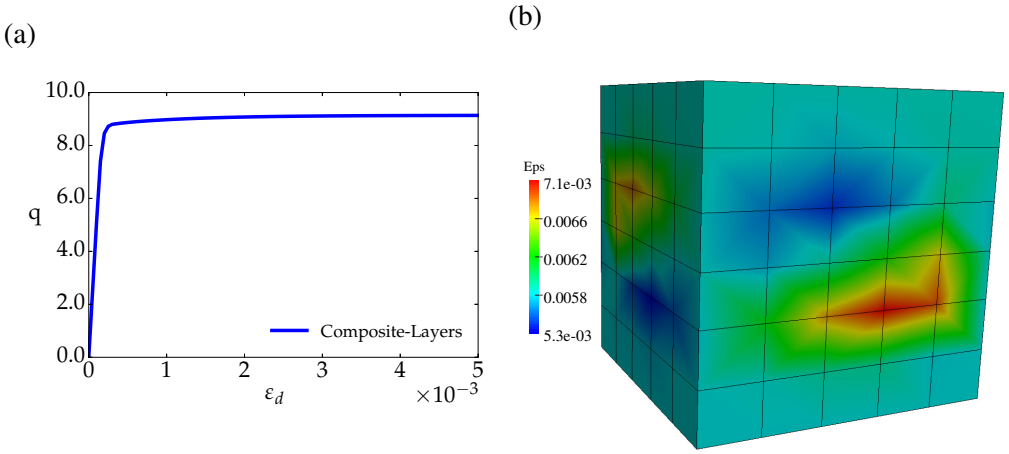

Figure 7.2: Layered composite model: (a) variation of deviatoric stress versus strain and (b) equivalent plastic strain (EP) distribution under linear boundary condition.

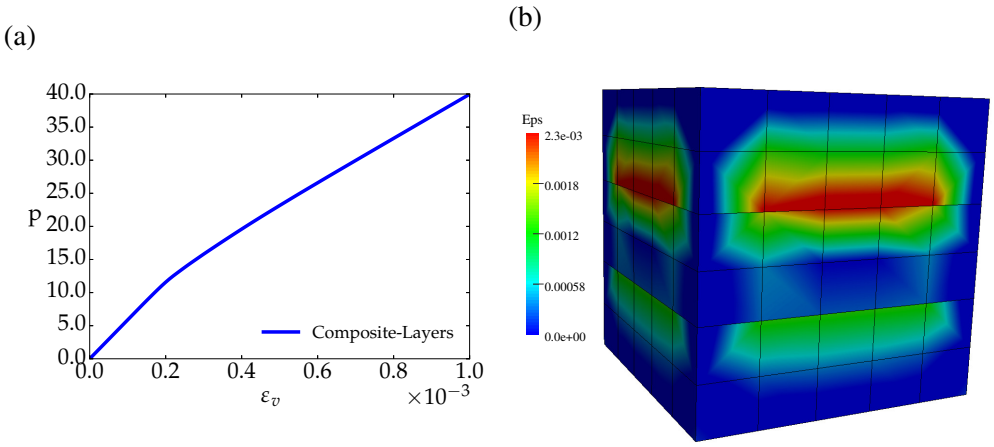

Figure 7.3: Layered composite model: (a) variation of pressure stress versus volumetric strain and (b) equivalent plastic strain (EP) distribution under uniform linear boundary condition.

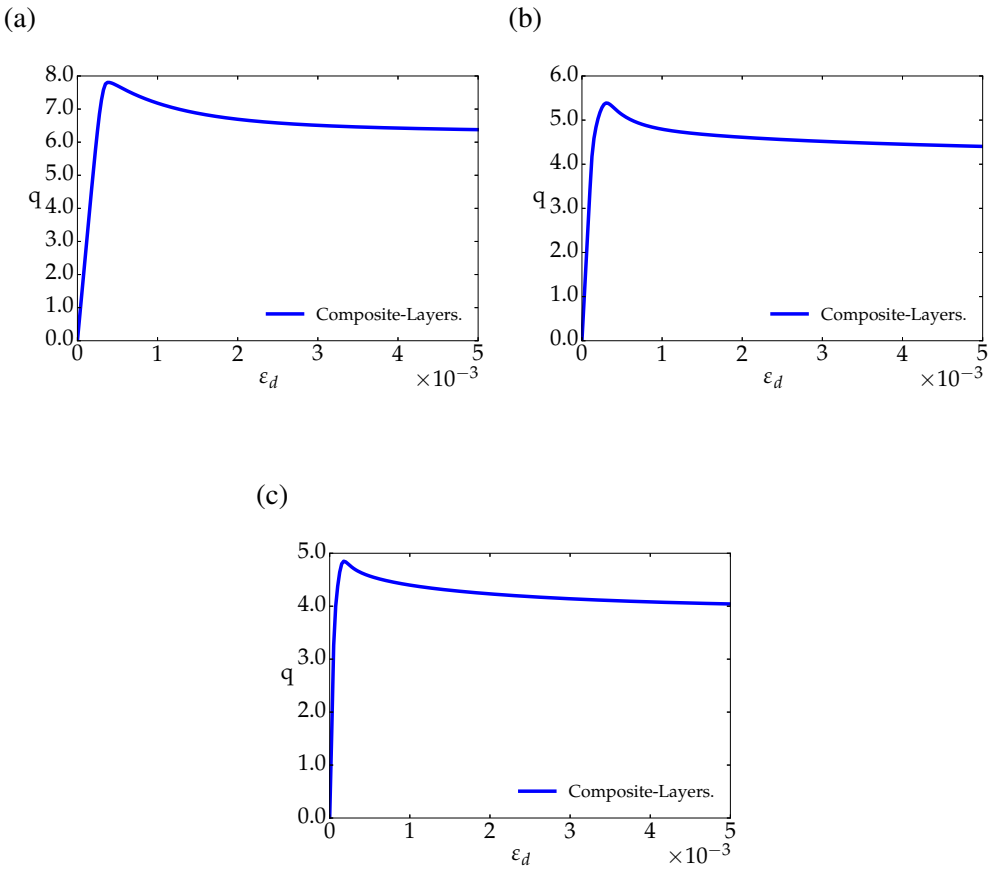

Figure 7.4: Variation of deviatoric stress versus strain in case of linear boundary condition with increasing compressive stress, (a) compressive stress with $\alpha = 0.2$, (b) compressive stress with $\alpha = 0.8$ and (c) compressive stress with $\alpha = 1$.

Next, we are applying uni-axial compressive stress to the uniformed layered system in both horizontal and vertical directions. The orientation axis of the model is shown in Figure 7.6.

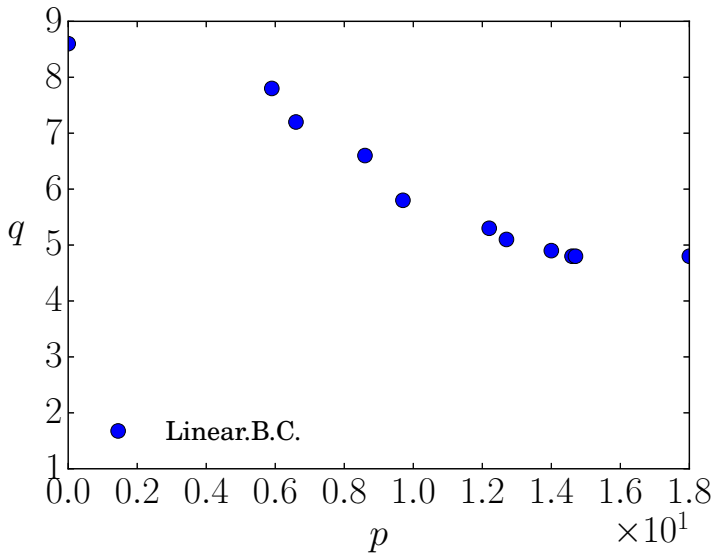

Figure 7.5: Yield surface for a layered composite with the von Mises material in case of linear boundary condition.

The variation of pressure over volumetric strain, deviatoric stress over strain, and the equivalent plastic strain distribution for both xx and zz (horizontal) directions and yy (vertical) direction are shown in Figures 7.7 to 7.9. respectively.

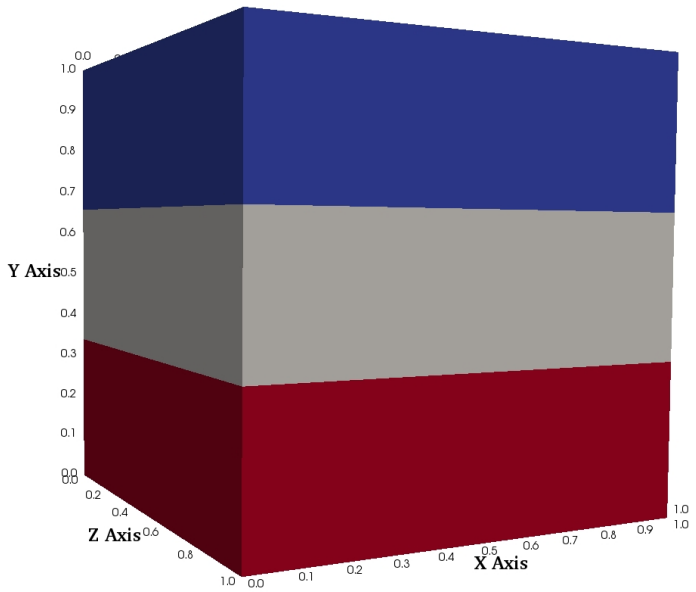

Figure 7.6: Layered composite model: geometry and axes orientation.

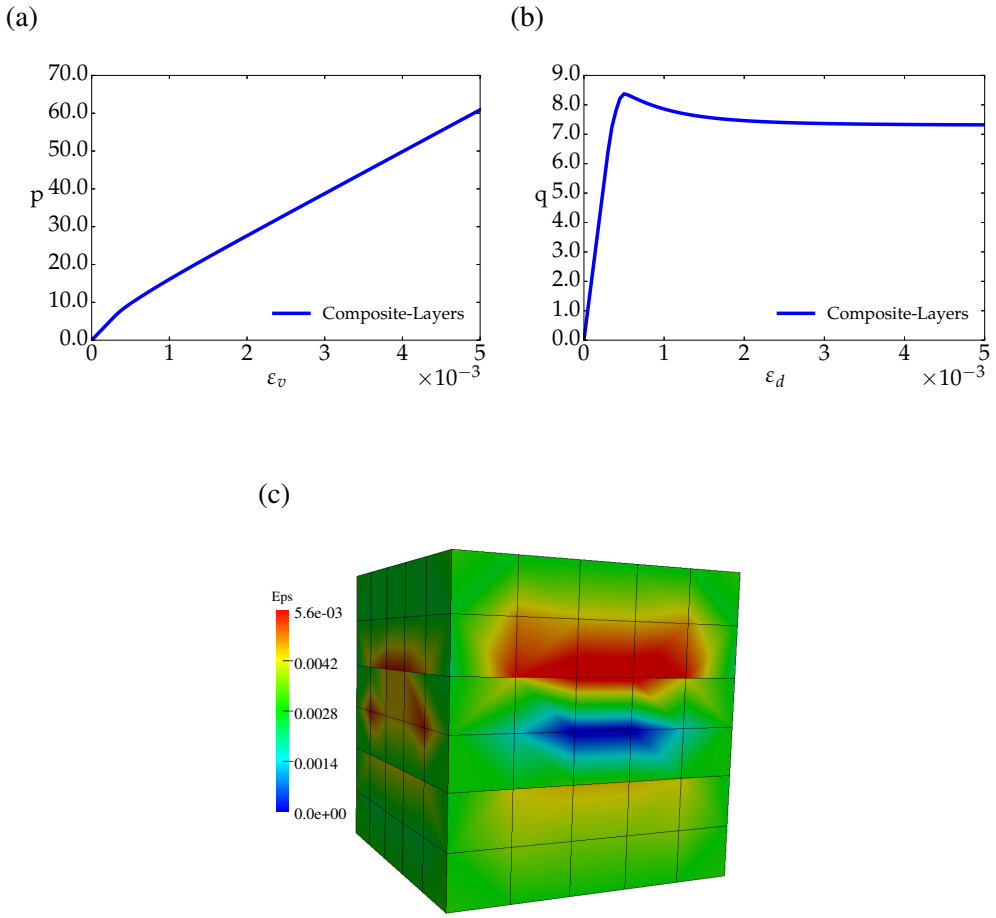

Figure 7.7: Hydrostatic pressure in xx direction in case of linear boundary condition (a) pressure versus volumetric strain, (b) deviatoric stress versus strain and (c) equivalent plastic strain (EP) distribution.

It can be seen that, the homogenized stress in vertical direction differs from the horizontal directions. That is to say, the model with uniform and zero orientation layers is behaving in an anisotropic manner due to different material properties assigned to each layer.

7.1.2 Effective Anisotropic Yield Surface under Uniform Traction Boundary Condition.

In this section we are repeating the same process as the previous section. But, under uniform traction boundary condition. As illustrated in Figure 7.12, the stress at the failure remains constant and does not vary with increasing the compressive stress. This case is related to material properties of the weakest layer (see Figure 7.13), the uniform traction boundary condition has the minimum kinematic constraint and

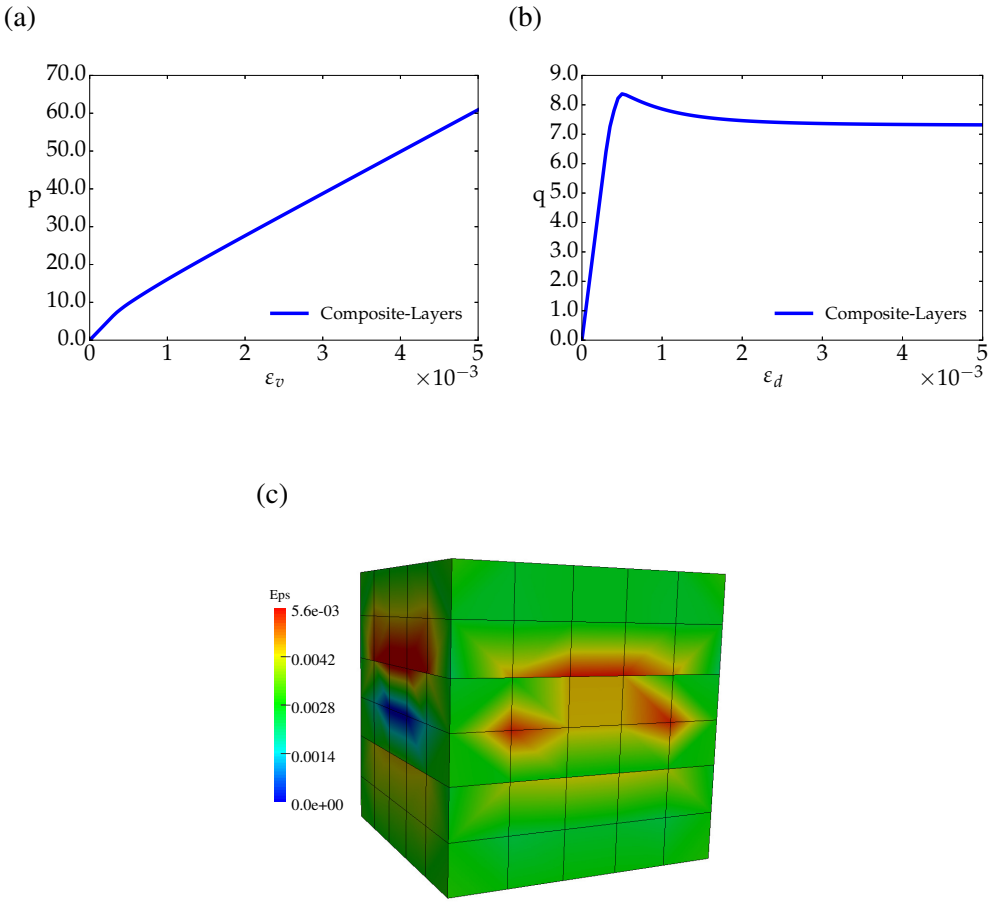

Figure 7.8: Hydrostatic pressure in zz direction in case of linear boundary condition (a) pressure versus volumetric strain, (b) deviatoric stress versus strain and (c) equivalent plastic strain (EP) distribution.

allows deformation of the middle layer independent of the other layer.

Note that, the model behaves in an anisotropic manner as the failure stresses in vertical direction differs from the horizontal stresses (see Figures 7.14 to 7.16).

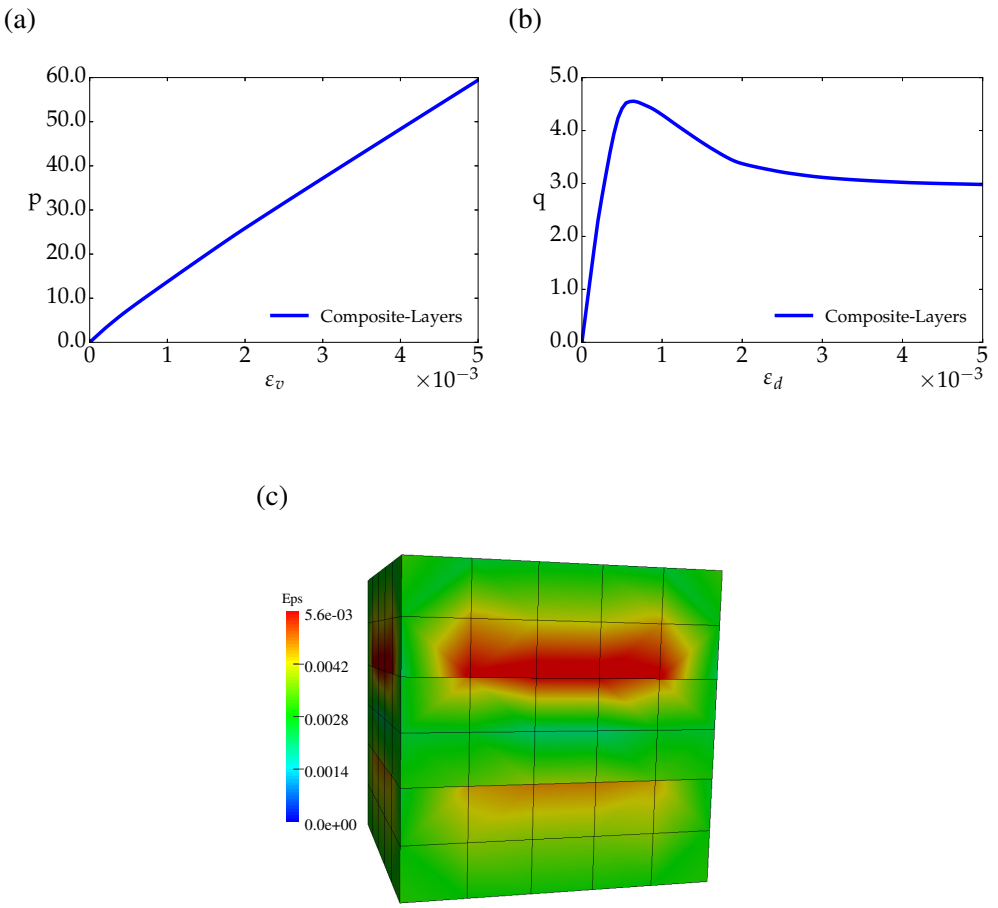

Figure 7.9: Hydrostatic in yy direction in case of linear boundary condition (a) pressure versus volumetric strain, (b) deviatoric stress versus strain and (c) equivalent plastic strain (EP) distribution.

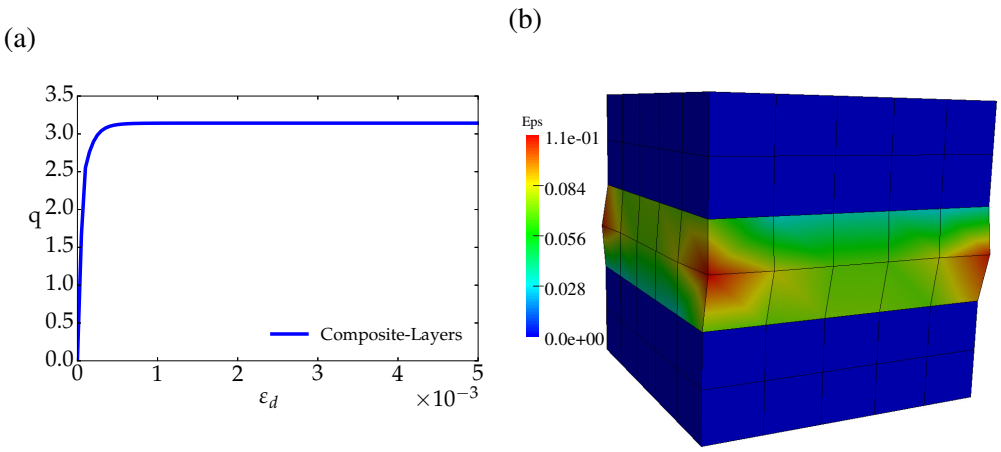

Figure 7.10: Layered composite model: (a) variation of deviatoric stress versus strain and (b) equivalent plastic strain (EP) distribution under uniform traction boundary condition.

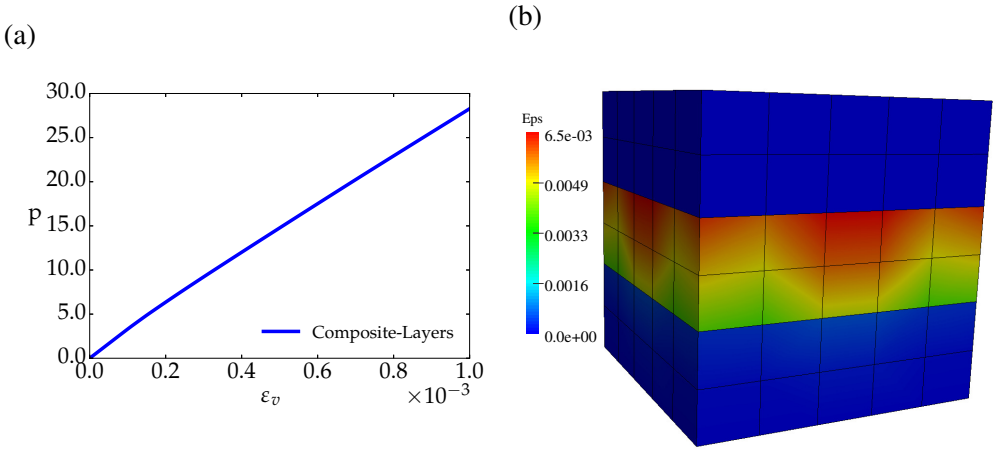

Figure 7.11: Layered composite model: (a) variation of pressure stress versus volumetric strain and (b) equivalent plastic strain (EP) distribution under uniform traction boundary condition.

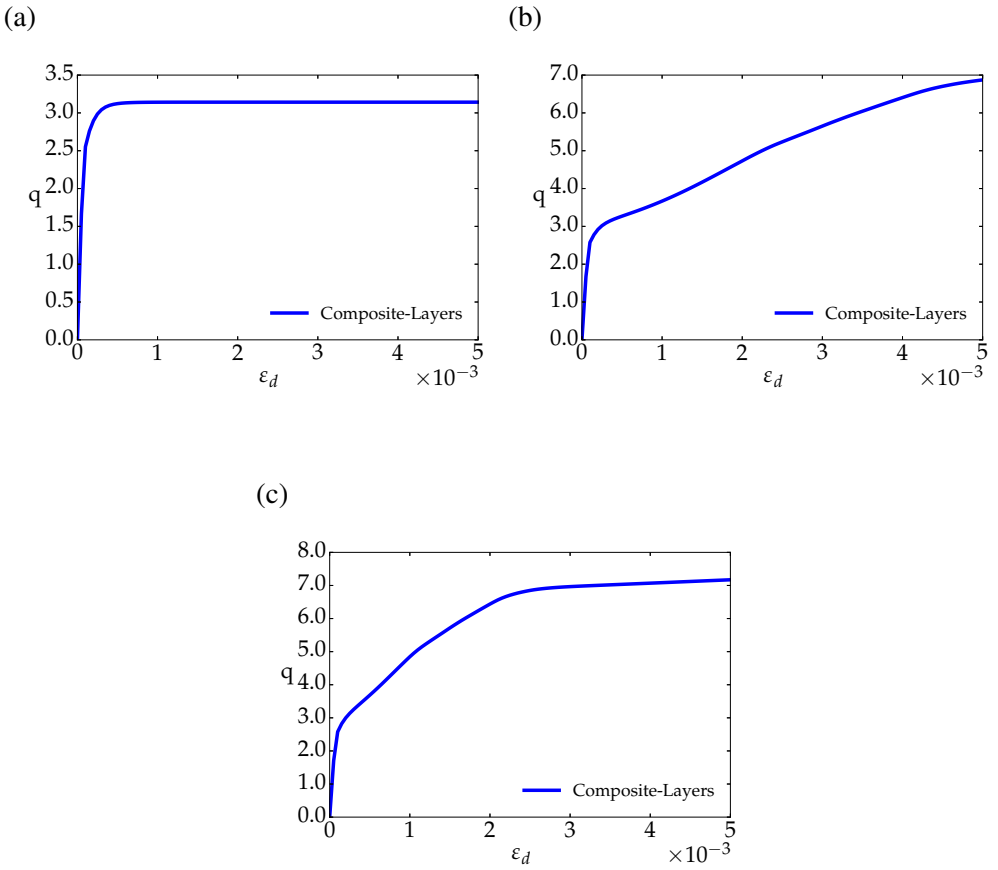

Figure 7.12: Variation of deviatoric stress versus strain in case of linear boundary condition with increasing compressive stress, (a) compressive stress with $\alpha = 0$, (b) compressive stress with $\alpha = 0.2$ and (c) compressive stress with $\alpha = 0.4$.

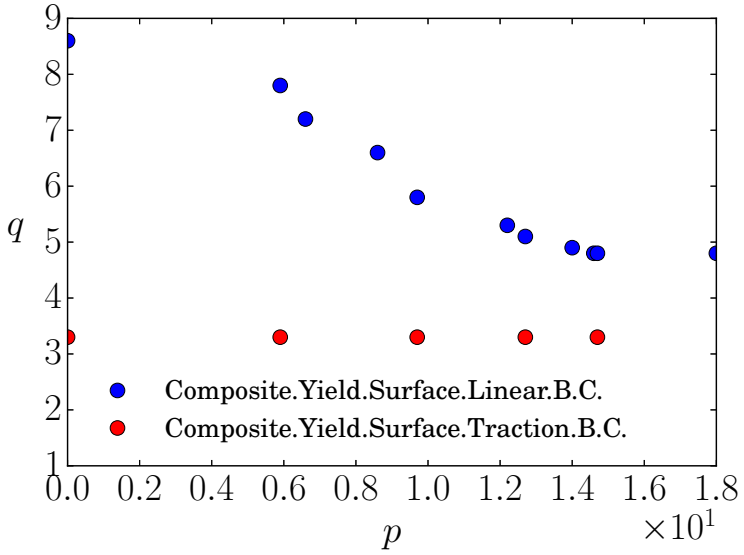

Figure 7.13: Yield surface for a layered composite with the von Mises material for linear and uniform traction boundary condition.

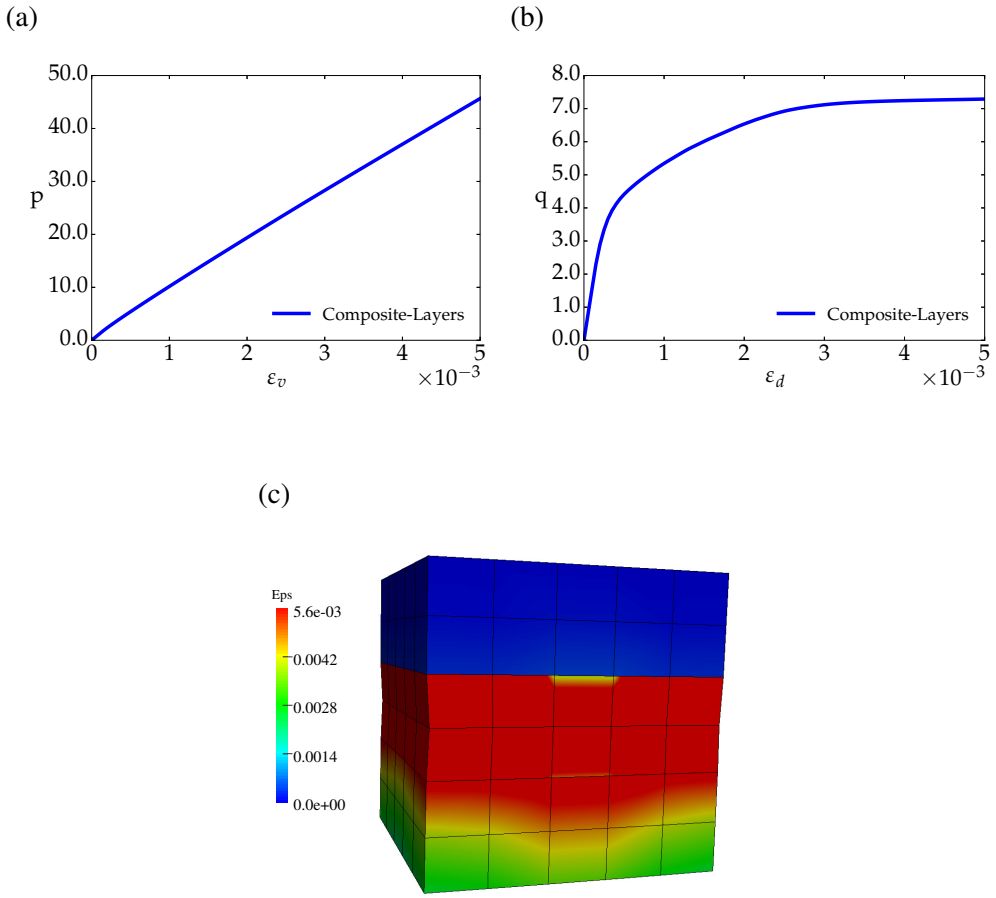

Figure 7.14: Hydrostatic pressure in *xx* direction in case of uniform traction boundary condition (a) pressure versus volumetric strain, (b) deviatoric stress versus strain and (c) equivalent plastic strain (EP) distribution.

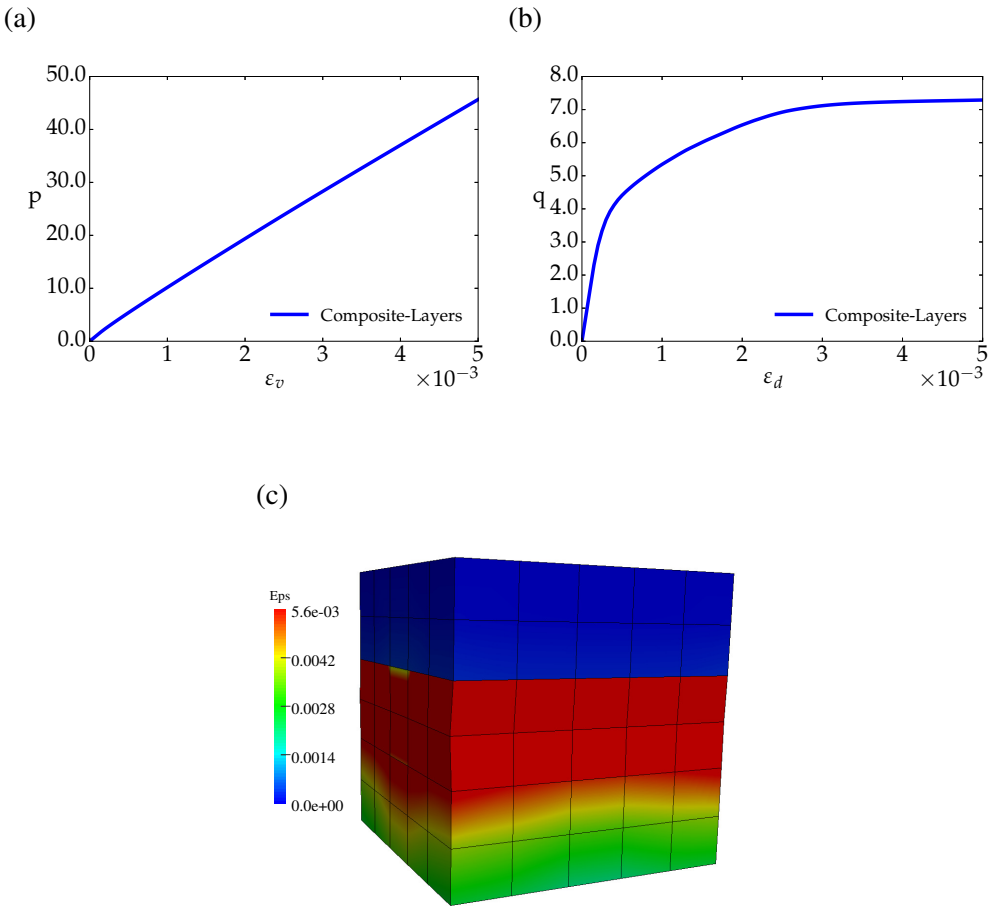

Figure 7.15: Hydrostatic pressure in zz direction in case of uniform traction boundary condition (a) pressure versus volumetric strain, (b) deviatoric stress versus strain and (c) equivalent plastic strain (EP) distribution.

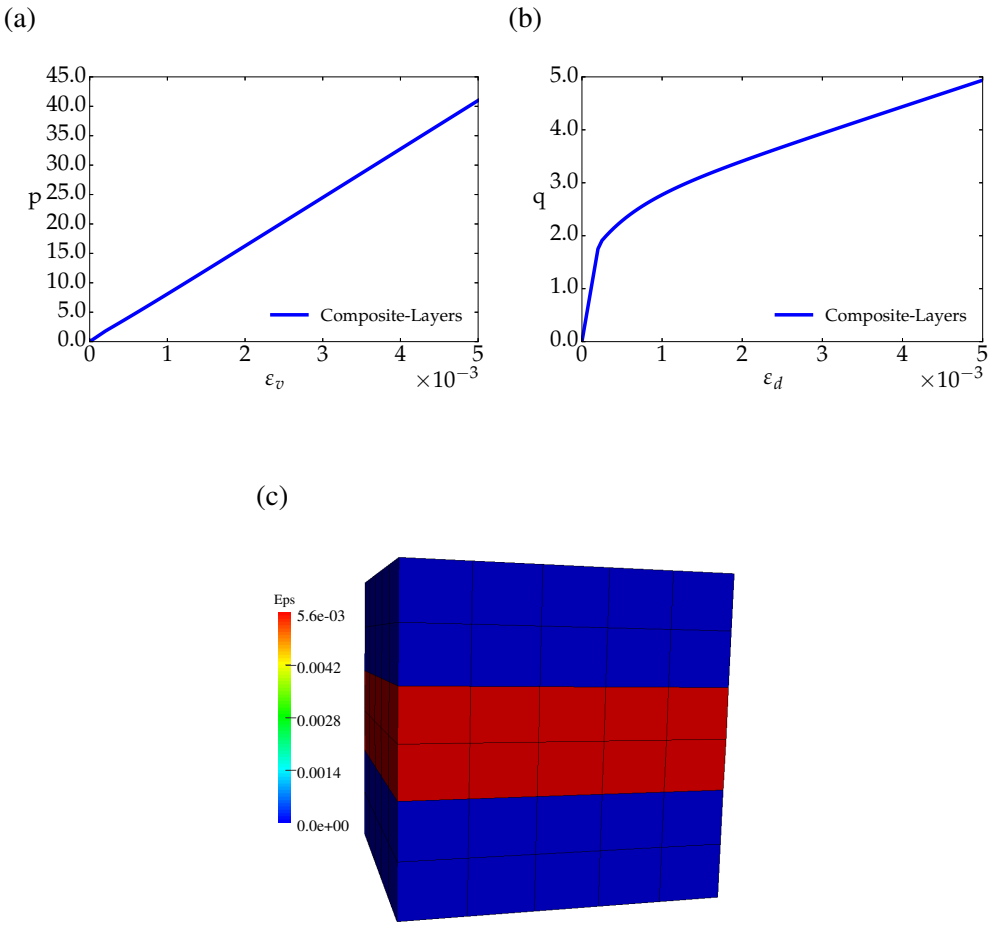

Figure 7.16: Hydrostatic pressure in yy direction in case of uniform traction boundary condition (a) pressure versus volumetric strain, (b) deviatoric stress versus strain and (c) equivalent plastic strain (EP) distribution.

7.2 Effective Anisotropic Yield Surface of a Layered Composite in Plane Stress

In this section, we are considering a 2-D composite layered model under plane stress assumption. The first system considered of three identical layers (homogeneous) which is modeled by von-Mises material while the second one consist of three uniform layers with varying the von-Mises material properties. By applying the computational methodology to the models, we are obtaining the effective macroscopic yield surface in principal axes. Note that, the material properties for

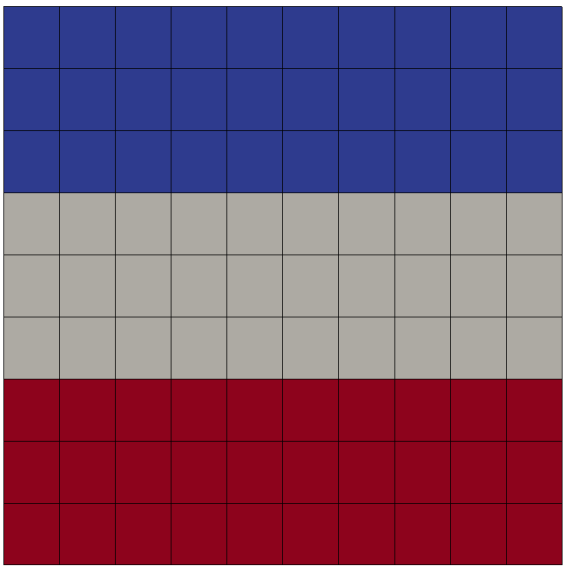

Figure 7.17: Layered composite model with the von Mises material properties under plane stress conditions.

each layer are identical to the ones given in the equation (7.1). The details of the numerical simulations are in the sections below.

7.2.1 Phenomenological Yield Functions

In this work, three yield functions, i.e., plane stress von-Mises model, Hill and Hoffman are investigated. The yield functions are given as follows,

The plane stress von Mises yield criterion: The von-Mises yield criterion under plane stress conditions is given by the following expression:

$$(\sigma_y)^2 + (\sigma_x)^2 + (\sigma_x - \sigma_y)^2 - \sigma_{\text{yield}} = 0 \tag{7.3}$$

Hill: In 1948 Hill [18] proposed the first measurable treatment of plastic anisotropy. He considered three orthogonal axes of anisotropy, x, y, and z about which there is a two-fold symmetry of properties. Therefore, the yz, zx, and xy planes are planes of mirror symmetry. In a rolled sheet, the x, y, and z-axes are usually taken as the rolling direction, the transverse direction and the sheet-plane normal (for more detail see, [125]).

Hill's yield criterion is a generalization of the von-Mises criterion:

$$\begin{aligned} F(\sigma_y - \sigma_z)^2 + G(\sigma_z - \sigma_x)^2 + H(\sigma_x - \sigma_y)^2 + \\ 2L\tau_{yz}^2 + 2M\tau_{zx}^2 + 2N\tau_{xy}^2 - \sigma_{\text{yield}} = 0, \end{aligned} \tag{7.4}$$

where, constants $F, G, H, L, M$and N describe anisotropy. However in case of plane stress and no shear, the expression above reduces to,

$$F(\sigma_y)^2 + G(\sigma_x)^2 + H(\sigma_x - \sigma_y)^2 - \sigma_{\text{yield}} = 0\,. \tag{7.5}$$

Hoffman: For many materials, the difference between yield stress levels in tension and compression can be observed (the Bauschinger effect). In some composite materials, this phenomenon is noticeable. Therefore, to model such effects, Hoffman [51] proposed an extension to the Hill criterion which is described by the following yield function:

$$\begin{aligned} C_1(\sigma_x - \sigma_y)^2 + C_2(\sigma_y - \sigma_z)^2 + C_3(\sigma_z - \sigma_x)^2 + \\ C_4\sigma_{xy}^2 + C_5\sigma_{yz}^2 + C_6\sigma_{xz}^2 + C_7\sigma_x + C_8\sigma_y + C_9\sigma_z - \sigma_{\text{yield}}^2 = 0, \end{aligned} \tag{7.6}$$

where, $C_1 - C_9$ are constants that describe anisotropy.

In order to identify the parameters for fitting the Hill and Hoffman yield functions for the composite model in Figure 7.17, we use the predicted anisotropic yield stresses. Based on the simulated yield stress point of composite materials, the parameters for proposed analytical models are obtained with ellipse fit by Taubin's [53] method. The details of the approach are described in the following section.

7.2.2 Analysis Approach

The computational homogenization under plane stress assumption has been used for all numerical simulations. The homogenized principal stress is obtained by imposing the macro-strain over the 2-D model for defined boundary condition (preferably uniform traction) over the RVE. The generic imposed macro-strain tensor is expressed by the following form:

$$\bar{\varepsilon} = [\alpha_1 \bar{\varepsilon}_{11} \, , \alpha_2 \bar{\varepsilon}_{22} \, , 0 \,] \tag{7.7}$$

where, $\alpha_1 = \cos\theta$, $\alpha_2 = \sin\theta$ and $0 \leq \theta \leq 360$ in order to cover the whole yield surface.

Finally, the $p - \varepsilon_v$ is plotted for each loading to specify the yield stress. As can be seen from the figures below yield surfaces have been predicted by interpolation from the homogenized principal stresses at yield obtained for different loading paths.

7.2.3 Yield Stress Surfaces

This section is divided into two parts. The first part is comparison of the virtual laboratory simulations of a homogeneous model under traction boundary condition against the plane stress von-Mises criteria (see, Figure 7.18).

The next part is comparison of the virtual laboratory simulations of a composite layers under both periodic and uniform traction boundary conditions against the Hoffman and Hill yield surfaces. Figure 7.19 illustrates predicted anisotropic yield surfaces for the composite layer system in the principal stress space.

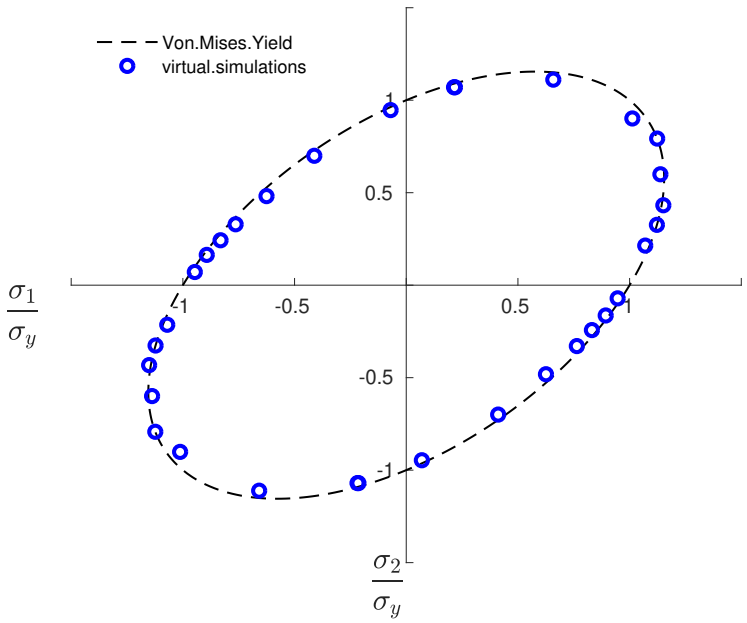

Figure 7.18: Comparison of the von-Mises yield surface ($\sigma_{12} = 0$) against the virtual laboratory simulations of the 2-D homogeneous model.

It can be observed from Figure 7.19 that the Hoffman yield function identified by the virtual laboratory under both periodic and uniform traction boundary conditions gives close approximation of the predicted yield stresses. However, the identified Hill yield function gives a poor fit to the predicted yield stresses.

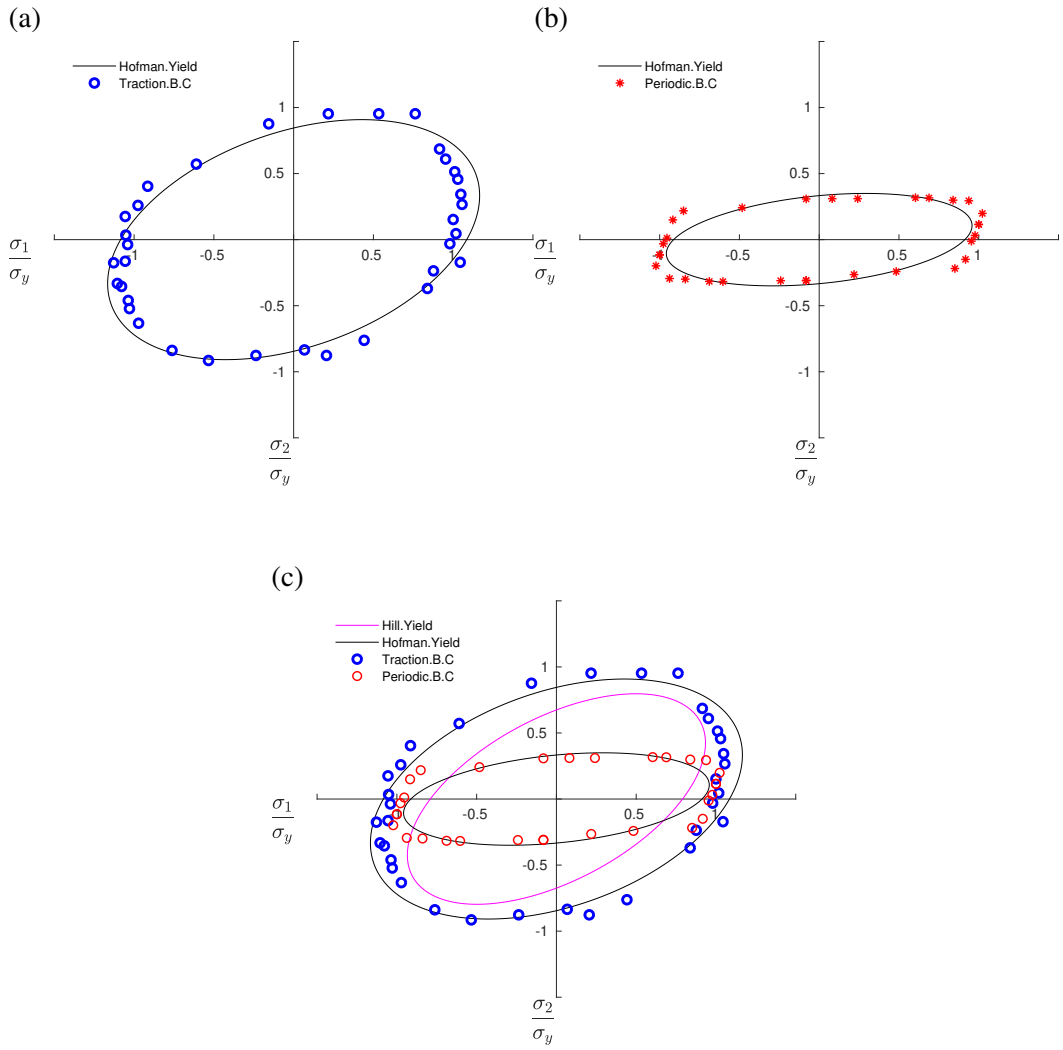

Figure 7.19: Comparison of the computationally obtained yield stresses ($\sigma_{12} = 0$) of the layered composite against the yield functions proposed by Hill [18] and Hoffman [51]. σ_y denotes the uni-axial tensile yield stress along the x-axis obtained from the virtual tests. (a) computational yield surface under traction boundary condition is compared against Hoffman yield surface, (b) computationally obtained yield stresses under periodic boundary conditions are compared against the Hoffman yield surface and, (c) comparison of computational yield surface of the composite model under both uniform traction and periodic boundary conditions against both Hill and Hoffman yield surfaces.

Chapter 8

Conclusions

The objective of this thesis was focused on establishment of a macroscopic yield criterion for a class of porous materials with a pressure sensitive matrix and spheroidal voids through a virtual laboratory approach. This approach is based on multi-scale analysis of solids that relies on homogenization and finite element methodology.

The multi-scale framework which relates the micro to macro scale was developed in small and large strain regimes. The homogenization problem relies on a variational treatment, which introduces a boundary conditions at the micro-scale (RVE). These consists of uniform displacement, uniform traction and periodic displacements including the corresponding tangent constitutive operators. In the implicit finite element method, the derivation of the homogenized tangent modulus are crucial for the solution of the non-linear macro-scale problems though the Newton-Raphson method.

A comprehensive set of numerical examples were presented. First, numerical multi-scale tests were performed to validate the accuracy of the obtained homogenized elastic material properties with the existing analytical solution proposed by [86]. Applying the different boundary conditions to the RVE with different percentage of the micro-cavities were considered for the test.

The effect of the distribution of cavities with a pressure sensitive matrix on material properties was studied. It was shown that increasing the density of pores causes the overall properties of the RVE under the three different boundary conditions to converge towards each other. However, the results of the linear displacement boundary condition still give the upper limit. All the boundary conditions for the

RVE with distributed voids give similar patterns of plastic strain distribution.

A computational homogenization framework for the linear and non-linear analysis of the elasto-plastic transition of porous pressure sensitive ductile materials through the virtual test was proposed. The homogenized macroscopic stress was obtained from the volume averaging of the stress tensor over a unit cube three-dimensional RVE with a pressure sensitive matrix, under the assumption of both implicit and explicit finite element method. The macroscopic yield curves are obtained for the two different RVEs geometry with 10% void ratio. From the systematic analysis of RVEs, considering two distinct kinematical models: linear boundary displacements (upper bound) and uniform boundary traction (lower bound). The yield surfaces predicted by the a computational framework have been evaluated through the comparisons with the analytical macro yield surface (see [114]) for both RVEs, and with two different matrix friction angles. It was found that the yield surfaces predicted by the computational strategy are very close to both macro surfaces, SR4 and Drucker-Prager for porous elasto-plastic solids. The accuracy of the computational homogenization through virtual tests had been carried out by applying it to the sand-stone box.

It is concluded that the SR4 and the proposed analytical criteria provide a valuable approximation of the macroscopic yield stress for porous materials with a Drucker-Prager matrix and spheroidal pores.

Finally, by applying this virtual laboratory concept to investigate the mechanical anisotropy of a series of parallel layers, such as rock-salt. The parameters of two yield functions used in sheet composite material, e.g., Hill [18] and Hoffman [51], were determined for two different boundary conditions of the RVE.

A large number of virtual tests, applying macroscopic strains over the RVE were performed by using the virtual laboratory. The computational yield stress points were used to identify the parameters of the analytical yield functions. Further, uniaxial tensile tests in different directions were also performed to normalized yield stresses.

The Hoffman yield function, shows good performance in fitting the yield surfaces. In contrast, the Hill yield function shows poor flexibility in fitting the composite yield surfaces, as it is not considering the Bauschinger effect.

8.1 Future Directions

A further study of virtual testing strategies in this area will consist of considering matrices described by constitutive models accounting for more complex phenomenological effects such as plastic anisotropy and crystal plasticity. The consideration of more complex loading paths may also provide a better insight on the failure mechanisms. Also the investigation of the mechanical anisotropy of biological materials based on multi-scale analysis is a clear direction for future research. In addition, the proposed numerical scheme can be extended to identify parameters for the advanced yield functions.

References

[1] J C Maxwell. *Homogenization techniques for composite media.* Clarendon Press, Oxford, 1873, p. 365.

[2] Rayleigh Lord. On the Influence of Obstacles Arranged in Rectangular Order Upon the Properties of a Medium. *Philosophical Magazine,*, 34:481–502, 1892.

[3] Z Hashin. The elastic moduli of heterogeneous materials. *Journal of Applied Mechanics*, 29:143–150, 1962.

[4] B Budiansky. On the elastic moduli of some heterogeneous materials. *Journal of the Mechanics and Physics of Solids*, 13:223–227, 1965.

[5] T. Mori and K Tanaka. Average stress in the matrix and average elastic energy of materials with misfitting inclusions. *Acta Metallurgica*, 21:571–574, 1973.

[6] E Kroner. Berechnung der elastischen Konstanten des Vielkristalls aus den Konstanten des Einkristalls. *Z. für Phys*, 151 (4):504–518, 1958.

[7] E. SanchezPalencia and A Zaoui. *Homogenization techniques for composite media.* Springer, New York, 1987.

[8] A. Tolenado and H. Murakami. A high-order mixture model for periodic particulate composites. *Int. J. Solids Struct*, 23:989–1002, 1987.

[9] J M. Guedes and N Kikuchi. Preprocessing and postprocessing for materials based on the homogenization method with adaptive finite element methods. *Comput. Meth. Appl. Mech. Engng.*, 83:143–198, 1990.

[10] P. Raghavan and Ghosh. S. Concurrent multi-scale analysis of elastic composites by a multi-level computational model. *Comput. Meth. Appl. Mech. Engng.*, 5,4:311–384, 1998.

[11] E. Hinton and B Hassani. A review of homogenization and topology optimization I- homogenization theory for media with periodic structure. *Computers and Structure*, 69:707–717, 1998.

[12] M. Gologanu, J B. Leblond, and J Devaux. Approximate models for ductile metals containing non-spherical voids—Case of axisymmetric prolate ellipsoidal cavities. *J. Mech. Phys. Solids*, 41 (11):1723–1754, 1993.

[13] V. Monchiet and D Kondo. Combined voids size and shape effects on the macroscopic criterion of ductile nanoporous materials. *Int. J. Plasticity*, 43:20–41, 2014.

[14] S M. Keralavarma and A A Benzerga. A constitutive model for plastically anisotropic solids with non-spherical voids. *J. Mech. Phys. Solids*, 58:874–901, 2010.

[15] J W. Yoon, F. Barlat, R E Dick, and M E Karabin. Prediction of six or eight ears in a drawn cup based on a new anisotropic yield function. *Int. J. Plast*, 22:174–193, 2006.

[16] F. Roters, P. Eisenlohr, L. Hantcherli, D D. Tjahjanto, T R. Bieler, and D Raabe. Overview of constitutive laws, kinematics, homogenization, and multiscale methods in crystal plasticity finite element modeling: theory, experiments, applications. *Acta Mater*, 58:1152–1211, 2010.

[17] R von Mises. Mechanik der plastischen Formanderung von Kristallen. *ZAMM Z. Angew. Math. Mech.*, 8:161–185, 1928.

[18] R Hill. A theory of the yielding and plastic flow of anisotropic metals. *Proc. R. Soc. A Math. Phys. Eng. Sci*, 193 (1033):281–297, 1948.

[19] R Hill. Constitutive modelling of orthotropic plasticity in sheet metals. *J. Mech. Phys. Solids*, 38 (3):405–417, 1948.

[20] F. Barlat and K Lian. Plastic behavior and stretchability of sheet metals. Part I: a yield function for orthotropic sheets under plane stress conditions. *Int. J. Plast*, 5 (1):51–66, 1989.

[21] F. Barlat, J C. Brem, J W. Yoon, K. Chung, R E. Dick, D J. Lege, F. Pourboghrat, S H. Choi, and E Chu. Plane stress yield function for aluminum alloy sheetsdpart 1: theory. *Int. J. Plast*, 19 (9):1297–1319, 2003.

[22] F. Barlat, H. Aretz, J W. Yoon, M E. Karabin, J C. Brem, and R E Dick. Linear transfomation-based anisotropic yield functions. *Int. J. Plast*, 21 (5):1009–1039, 2005.

[23] F. Barlat, Y. Maeda, K. Chung, M. Yanagawa, J C. Brem, Y. Hayashida, D J. Lege, K. Matsui, S J. Murtha, S. Hattori, R C. Becker, and S Makosey. Yield function development for aluminum alloy sheets. *J. Mech. Phys. Solids*, 45 (11-12):1727–1763, 1997.

[24] A P. Karafillis and M C Boyce. A general anisotropic yield criterion using bounds and a transformation weighting tensor. *J. Mech. Phys. Solids*, 41 (12):1859–1886, 1997.

[25] D. Banabic, T. Kuwabara, T. Balan, D S. Comsa, and D Julean. Non-quadratic yield criterion for orthotropic sheet metals under plane-stress conditions. *Int. J. Mech. Sci*, 45 (5):797–811, 2003.

[26] F. Barlat, H. Aretz, J W. Yoon, M E. Karabin, J C. Brem, and R E Dick. Linear transfomation-based anisotropic yield functions. *Int. J. Plast*, 20 (4-5):937–963, 2005.

[27] G Sachs. *Mitteilungen der deutschen Materialprüfungsanstalten.*, chapter chapter Zur Ableitung einer Fließbedingung, pp. 94-97. 1929.

[28] G I Taylor. Plastic strains in metals. *J. Inst. Metals*, 62:307–324, 1938.

[29] J F W. Bishop and R Hill. A theory of the plastic distortion of a polycrystalline aggregate under combined stresses. *Philos. Mag*, 42 (327):414–427, 1951.

[30] W F Hosford. A generalized isotropic yield criterion. *J. Appl. Mech*, 39 (2):607–609, 1972.

[31] P Van Houtte. Application of plastic potentials to strain rate sensitive and insensitive anisotropic materials. *Int. J. Plast*, 10 (7):719–748, 1994.

[32] S. Li, E. Hoferlin, A. Van Bael, P. Van Houtte, and C Teodosiu. Finite element modeling of plastic anisotropy induced by texture and strain-path change. *Int. J. Plast*, 19 (5):647–674, 2003.

[33] K. Kowalczyk and W Gambin.

[34] D. Raabe, P. Klose, B. Engl, K P. Imlau, F. Friedel, and F Roters. Concepts for integrating plastic anisotropy into metal forming simulations. *Adv. Eng. Mater*, 4 (4):169–180, 2002a.

[35] A Anthoine. A Derivation of in-plane characteristics of masonry through homogenization theory. *Int. J. Solids*, 32:137–163, 1995.

[36] S. Ghosh, K Lee, and S Murthy. Two scale analysis of heterogeneous elastic-plastic materials with asymptotic homogenization and voronoi cell finite element method. *Comp. Meth. Appl. Mech. Engng.*, 132:63–116, 1996.

[37] J C. Michel, H. Moulinec, and P Suquet. Effective properties of composite materials with periodic microstructure: A computational approach. *Comp. Meth. Appl. Mech. Engng.*, 172:109–143, 1999.

[38] C Miehe. Strain-driven homogenization of inelastic microstructures and composites based on an incremental variational formulation. *Int. J. Num. Meth. Engng.*, 55:1285–1322, 2002.

[39] K. Zhang, B. Holmedal, O S. Hopperstad, S. Dumoulin, J. Gawad, A V. Bael, and P V Houtte. Multi-level modelling of mechanical anisotropy of com- mercial pure aluminium plate: crystal plasticity models, advanced yield functions and parameter identification. *Int. J. Plast.*, 66:3–30, 215.

[40] A. Prakash and R A Lebensohn. Simulation of micromechanical behavior of polycrystals: finite elements versus fast Fourier transforms. *Model. Simul. Mater. Sci. Eng*, 17:064010–064016, 2009.

[41] R A. Lebensohn, A K. Kanjarla, and P Eisenlohr. An elasto-viscoplastic formulation based on fast Fourier transforms for the prediction of micromechanical fields in polycrystalline materials. *Int. J. Plast*, 33:59–69, 2012.

[42] P. Eisenlohr, M. Diehl, R A. Lebensohn, and F Roters. A spectral method solution to crystal elasto-viscoplasticity at finite strains. *Int. J. Plast*, 46:37–53, 2013.

[43] S. Ghosh, K. Lee, and S Moorthy. Multiple scale analysis of heterogeneous elastic structures using homogenisation theory and Voronoi cell finite element method. *Int. J. Solids Struct*, 32:27–62, 1995.

[44] K. Terada and N. Kikuchi. A class of general algorithms for multi-scale analyses of heterogeneous media. *Comput. Meth. Appl. Mech. Engng.*, 190:5427–5464, 2001.

[45] C. Miehe, J. Schotte, and J. Schröder. Computational micro-macro transitions and overall tangent moduli in the analysis of polycrystals at large strains. *Comput. Materials Sci.*, 16:372–382, 1999a.

[46] C. Miehe, J. Schröder, and J. Schotte. Computational homogenization analysis in finite plasticity. Simulation of texture development in polycrystalline materials. *Comput. Meth. Appl. Mech. Engng.*, 171:387–418, 1999.

[47] F. Feyel and J-L Chaboche. Fe^2 multiscale approach for modelling the elastoviscoplastic behaviour of long fibre SiC/Ti composite materials. *Comp. Meth. Appl. Mech. Engng.*, 183:309–330, 2000.

[48] S. Ghosh, K. Lee, and P Raghavan. A multi-level computational model for multi-scale damage analysis in composite and porous materials. *Int. J. Solids Struct*, 38:2335–2385, 2001.

[49] C. Miehe and A. Koch. Computational micro-to-macro transitions of discretized microstructures undergoing small strains. *Arch. Appl. Mech.*, 72:300–317, 2002.

[50] R J M. Smit, W A M. Brekelmans, and H E H Meijer. Prediction of the mechanical behaviour of non-linear heterogeneous systems by multi-level

finite element modeling. *Comput. Meth. Appl. Mech. Engng.*, 155:181–192, 1998.

[51] O Hoffman. The brittle strength of orthotropic materials. *J. Composite. Mater.*, 1:200–206, 1967.

[52] A J L. Crook, S M. Willson, J G. Yu, and D R J Owen. Predictive modelling of structure evolution in sandbox experiments. *J. Struct. Geol.*, 28:729–744, 2006.

[53] G Taubin. Estimation of Planar Curves, Surfaces, and Nonplanar Space Curves Defined by Implicit Equations with Applications to Edge and Range Image Segmentation. *IEEE Transactions on Pattern Analysis and Machine Intelligence.*, 13(11):1115–1138, 1991.

[54] E A. de Souza Neto, D. Peric, and D R J Owen. *Computational Methods for Plasticity: Theory and Applications*. Wiley, Chichester, 2008.

[55] J. Bonet and R D Wood. *Nonlinear Continuum Mechanics for Finite Element Analysis.* Cambridge University Press, 2008.

[56] J. Obradors-Prats, M. Rouainia, A C. Aplin, and A J L Crook. Assessing the implications of tectonic compaction on pore pressure using a coupled geomechanical approach. *Marine Petroleum Geol.*, 79:31–43, 2017.

[57] J. Lemaitre and J L Chaboche. *Mechanics of Solids Materials.* Cambridge University Press, 1990.

[58] D Perić. Computational plasticity, lecture notes. 2004.

[59] E H Lee. Elastic-plastic deformation at finite strains. *J. Appl. Mech*, 36(1-6), 1969.

[60] E H. Lee and D T Liu. Finite strain elastic-plastic theory with application to plane-wave analysis. *J. Appl. Phys*, 38(19-27), 1967.

[61] D D. Somer, D. Perić, E A. de Souza Neto, and W G Dettmer. On the characterisation of elastic properties of long fibre composites using computational homogenisation. *Comput. Mater. Sci.*, 83:149–157, 2014.

[62] P V Lade. Instability, shear banding, and failure in granular materials. *Int. J. Solids Structures*, 39(3337-3357), 2002.

[63] C S. Desai and M R Salami. A constitutive model and associated testing for soft rock. *Int. J. Rock Mech. Min. Sci.*, 24(299-307), 1987.

[64] D. Perić and D R J Owen. Computational Modeling of Forming Processes. *Encyclopedia of Computational Mechanics Second Edition*, pages 1–51, 2017.

[65] O C. Zienkiewicz and R L Taylor. *The Finite Element Method for Solid and Structural Mechanics.* Elsevier Butterworth and Heinemann, Oxford, England, sixth edition, 2005.

[66] T. Belytschko, W K. Liu, and B Moran. *Nonlinear Finite Elements for Continua and Structures.* Wiley: New York, 2000.

[67] K J Bathe. *Finite Element Procedures (2nd edn).* Prentice-Hall: Englewood Cliffs, 1996.

[68] T J R Hughes. *The Finite Element Method. Linear Static and Dynamic Finite Element Analysis.* Prentice-Hall: Englewood Cliffs, 1987.

[69] J C. Simo and T J R Hughes. *Computational Inelasticity.* Springer-Verlag: New York, 1998.

[70] T J R. Hughes and J Winget. Finite rotation effects in numerical integration of rate constitutive equations arising in large deformation analysis. *Int. J. Numer. Methods Eng*, 15:1862–1867, 1980.

[71] J C. Simo and R L Taylor. Consistent tangent operators for rate independent elastoplasticity. *Comput. Methods Appl. Mech. Eng*, 48:101–118, 1985.

[72] J C. Simo and F Armero. Geometrically non-linear enhanced strain mixed methods and the method of incompatible modes. *Int. J. Numer. Methods Eng*, 33:1413–1449, 1992.

[73] T. Sussman and K J Bathe. A finite element formulation for non-linear incompressible elastic and inelastic analysis. *Comput. Struct*, 26:357–409, 1987.

[74] B. Moran, M. Ortiz, and F Shih. Formulation of implicit finite element methods for multiplicative finite deformation plasticity. *Int. J. Numer. Methods Eng*, 29:483–514, 1990.

[75] I C. Nagtegaal, D M. Parks, and J R Rice. NAGTEGAAL*, D.M. PARKS and J.R. RICE. 4:153–177, 1974.

[76] E A. de Souza Neto, D. Perić, and D R J Owen. F-bar based linear triangles and tetrahedra for finite strain analysis of nearly incompressible solids. part i: Formulation and bench marking. *Int. J. Numer. Methods Eng*, 2004; in press.

[77] James M Kennedy. Wing Kam LIU. *Applied Mechanics and Engineering*, 1984.

[78] G Maenchen and S Sack. *The TENSOR code, in: B. Alder et al., eds., Methods in Computational Physics, Vol. 3.* Academic Press, New York,, 1964.

[79] B. Irons and S Ahmad. *Techniques of Finite ELements.* Ellis Horwood, Chichester, 1980.

[80] T. Belytschko, J S J. Ong, and W K Liu. A consistent control of spurious singular modes in the 9-node Lagrange element for the Laplace and Mindlin plate equations. *Comput. Meths. Appl. Mech. Engrg.*, 44:269–295, 1984.

[81] T. Belytschko, C S. Tsay, and W K Liu. A stabilization matrix for the bilinear Mindlin plate element. *Comput. Meths. Appl. Mech. Engrg.*, 29:313–327, 1981.

[82] T. Belytschko and J M Kennedy. Computer models for subassembly simulation. *Nuclear Engrg. Design*, 49:17–38, 1978.

[83] S W Key. A finite element procedure for the large deformation dynamics response of axisymmetric solids. *Comput. Meths. Appl. Mech. Engrg.*, 4:195–218, 1974.

[84] G A Kosloff, D. Frazier. Treatment of hourglass patterns in low order finite element codes. *Internat. J. Numer. Anal. Meths. Geomech.*, 2:57–72, 1978.

[85] D P. Flanagan and T Belytschko. A uniform strain hexahedron and quadrilateral with orthogonal hourglass control. *Internat. J. Numer. Meths. Engrg.*, 17:679–706, 1981.

[86] M. Hori and S Nemat-Nasser. On two micromechanics theories for determining micro-macro relations in heterogeneous solids. *Mech. Mater.*, 31:667–682, 1999.

[87] J D. Clayton and D L McDowell. Meso-macro modelling of fibre-reinforced rubber-like com- posites exhibiting large elastoplastic deformations. *Int. J. Solids Struct*, 40:951–980, 2003.

[88] A. Ibrahimbegović and D Markovič. Strong coupling methods in multi-phase and multi-scale modeling of inelastic behavior of heterogeneous structures. *Comp. Meth. Appl. Mech. Engng.*, 192:3089–3107, 2003.

[89] Kazumi. Matsui, Kenjiro. Terada, and Kohei Yuge. Two-scale finite element analysis of heterogeneous solids with periodic microstructures. *Computers and Structures*, 82:593–606, 2004.

[90] V. G. Kouznetsova, M. G.D. Geers, and W. A.M. Brekelmans. Multi-scale second-order computational homogenization of multi-phase materials: A nested finite element solution strategy. *Computer Methods in Applied Mechanics and Engineering*, 193(48-51):5525–5550, 2004.

[91] D. Perić, E A. de Souza Neto, R A. Feijóo, M. Partovi, and A J Carneiro Molina. On micro-to-macro transitions for multi-scale analysis of non-linear heterogeneous materials:unified variattional basis and finite element implementation. *Int. J. Num. Meth. Engng.*, 87:149–170, 2011.

[92] E A. de Souza Neto and R A Feijóo. Variational foundations of multi-scale constitutive models of solid:small and large strain kinematical formulation. Technical Report No. 16/2006, National Laboratory for Scientific Computing (LNCC/MCT), Brazil, 2006.

[93] Maziar Partovi. Computational Strategies for Multiscale Analysis of Material Behaviour. (January), 2007.

[94] P M. Suquet. Local and global aspects in the mathematical theory of plasticity. In A. Sawczuk, editor, *Plasticity Today: Modelling Methods and Applications*. Elsevier Applied Science Publishers, Amsterdam, 1985.

[95] P M. Suquet. Elements of homogenization for inelastic solid mechanics. In E. Sanchez-Palencia and A. Zaoui, editors, *Elements of Homogenization for Inelastic Solid Mechanics.* Springer-Verlag, Berlin, 1987.

[96] H. Moulinec and P. Suquet. A numerical method for computing the overall response of nonlinear composites with complex microstructure. *Comput. Meth. Appl. Mech. Engng.*, 157:69–94, 1998.

[97] C. Miehe, J. Schröder, and J. Schotte. Computational homogenization analysis in finite plasticity. simulation of texture developtment in polycrystalline materials. *Comput. Meth. Appl. Mech. Engng.*, 171:387–418, 1999b.

[98] V. G. Kouznetsova, W. A. M. Brekelmans, and F. P. T. Baaijens. An approach to micro-macro modelling of heterogeneous materials. *Comput. Mech.*, 27:37–48, 2001.

[99] P. Ladevèze, O. Loiseau, and D. Dureisseix. A micro-macro and parallel computational strategy for highly heterogeneous structures. *Int. J. Numer. Meth. Engng.*, 52:121–138, 2001.

[100] A L Gurson. Continuum theory of ductile rupture by void nucleation and growth: Part 1 - yield criteria and flow rules for porous ductile media. *J. Eng. Mater. Technol.*, 99:2–15, 1977.

[101] A. A. Benzerga and J.-B. Leblond. Ductile fracture by void growth to coalescence. *Adv. Appl. Mech.*, 44:169–305, 2010.

[102] F. Fritzen, S. Forest, T. Böhlke, D. Kondo, and T Kanit. Computational homogenization of elasto-plastic porous metals. *Int. J. Plasticity*, 29:102–119, 2012.

[103] V. Monchiet and G Bonnet. Gurson-type model accounting for void size effects. *Int. J. Solids Struct.*, 50:320–327, 2013.

[104] C. Ling, J. Besson, S. Forest, B. Tanguy, F. Latourte, and E. Bosso. An elastoviscoplastic model for porous single crystals at finite strains and its assessment based on unit cell simulations. *Int. J. Plasticity*, 84:58–87, 2016.

[105] O. Cazacu and B. Revil-Baudard. New analytic criterion for porous solids with pressure-insensitive matrix. *Int. J. Plasticity*, 89:66–84, 2017.

[106] M. I. El Ghezal and I. Doghri. Porous plasticity: Predictive second moment homogenization models coupled with Gurson's single cavity stress-strain solution. *Int. J. Plasticity*, 108:201–221, 2018.

[107] H Y Jeong. A new yield function and a hydrostatic stress-controlled model for porous solids with pressure-sensitive matrices. *Int. J. Solids Struct.*, 39:1385–1403, 2002.

[108] T F. Guo, J. Faleskog, and C Shih. Continuum modeling of a porous solid with pressure-sensitive dilatant matrix. *J. Mech. Phys. Solids*, 56:2188–2212, 2008.

[109] D. Durban, T. Cohen, and Y Hollander. Plastic response of porous solids with pressure sensitive matrix. *Mech. Res. Commun.*, 37:636–641, 2010.

[110] J. Pastor, P. Thoré, and F Pastor. Limit analysis and numerical modeling of spherically porous solids with Coulomb and Drucker-Prager matrices. *J. Comput. Appl. Math.*, 234:2162–2174, 2010.

[111] V. Monchiet and D Kondo. Exact solution of a plastic hollow sphere with a Mises-Schleicher matrix. *Int. J. Eng. Sci.*, 51:168–178, 2012.

[112] F. Pastor, D. Kondo, and J. Pastor. 3D-FEM formulations of limit analysis methods for porous pressure-sensitive materials. *Int. J. Num. Meth. Engng.*, 95:847–870, 2013.

[113] W Q. Shen, J F. Shao, D. Kondo, and G De Saxce. A new macroscopic criterion of porous materials with a Mises-Schleicher compressible matrix. *Eur. J. Mech. A/Solids*, 49:531–538, 2015.

[114] W Q. Shen, J. Zhang, J F. Shao, and D Kondo. Approximate macroscopic yield criteria for Drucker-Prager type solids with spheroidal voids. *Int. J. Plasticity*, 99:221–247, 2017.

[115] S M. Giusti, P J. Blanco, E A. de Souza Neto, and R A Feijóo. An assessment of the Gurson yield criterion by a computational multi-scale approach. *Eng. Comput.*, 26:281–301, 2009.

[116] D D. Somer, D. Perić, E A. de Souza Neto, and W G Dettmer. Yield surfaces of heterogeneous media with debonded inclusions. *Eng. Comput.*, 32:1802–1813, 2015.

[117] Pinto Carvalho. Rodrigo, Lopes Igor A. Rodrigues, and F M Andrade Pires. Prediction of the yielding behaviour of ductile porous materials through computational homogenization. *Eng. Comput.*, 35:604–621, 2017.

[118] H. Zhang, M. Diehl, F. Roters, and D. Raabe. A virtual laboratory using high resolution crystal plasticity simulations to determine the initial yield surface for sheet metal forming operations. *Int. J. Plasticity*, 80:111–138, 2016.

[119] A. Esmaeili, S. Asadi, F. Larsson, and K. Runesson. Construction of macroscale yield surfaces for ductile composites based on a virtual testing strategy. *Eur. J. Mech. A/Solids*, 77:103786, 2019.

[120] Y. J. Cao, W. Q. Shen, J. F. Shao, and N. Burlion. Influences of micro-pores and meso-pores on elastic and plastic properties of porous materials. *Eur. J. Mech. A/Solids*, 72:407–423, 2018.

[121] A. Casagrande. The determination of the pre-consolidation load and its practical significance. In *Proceedings of the 1st International Conference on Soil Mechanics and Foundation Engineering*, volume 3, pages 60–64, Harvard University, Cambridge, 1936.

[122] A J L Crook. Parageo: A finite element model for coupled simulation of the evolution of geological structures. Technical report, Three Cliffs Geomechanical Analysis, Swansea, UK, 2013.

[123] D A. Thornton and A J L Crook. Predictive Modeling of the Evolution of Fault Structure: 3-D Modeling and Coupled Geomechanical/Flow Simulation. *Rock Mech Rock Eng*, 47:1533–1549, 2014.

[124] J. Obradors-Prats, M. Rouainia, A C. Aplin, and A J L Crook. A diagenesis model for geomechanical simulations: Formulation and implications for pore pressure and development of geological structures. *Journal of Geophysical Research: Solid Earth*, 124:4452–4472, 2019.

[125] W F Hosford. *Fundamentals of engineering plasticity.* Cambridge University Press, 2013.

[126] D D. Somer, E A. de Souza Neto, D. Perić, and W G Dettmer. A sub-stepping scheme for multi-scale analysis of solids. *Comput. Meth. Appl. Mech. Engng.*, 198:1006–1016, 2009.

[127] R Hill. A new macroscopic criterion of porous materials with a mises-schleicher compressible matrix. *J. Mech. Phys. Solids*, 13:213–22, 1965.

[128] J. Mandel. *Plasticité Classique et Viscoplasticité*. CISM Courses and Lectures No. 97. Springer-Verlag, Udine, Italy, 1971.

Appendix A

A.1 Small Strain Homogenization-Based Multi-Scale Constitutive Theory

In order to provide a complete exposition of the virtual testing approach presented in this work, next two sections briefly describe variational basis and finite element approximation of the adopted multi-scale homogenisation methodology. For more details related to variational setting and finite element implementation we refer to our earlier articles [92], [91] and [126].

It is assumed from the outset that any material point $\boldsymbol{x}$ of the (macroscopic) continuum is associated with a local Representative Volume Element (RVE) whose domain Ω_μ, with boundary $\partial\Omega_\mu$, (see Figure A.1), has a characteristic length, l_μ. Furthermore, it is assumed that the length l_μ is much smaller than the characteristic length, l, of the macro-continuum, thus ensuring the separation of scales, which is essential ingredient of the adopted family of the multi-scale methods. The domain Ω_μ of the RVE is assumed to consist in general of a solid part, Ω_μ^s, and a void part, Ω_μ^v:

$$\Omega_\mu = \Omega_\mu^s \cup \Omega_\mu^v. \tag{A.1}$$

For simplicity, in what follows, we shall consider only RVEs whose void part does not intersect the RVE boundary.

Fundamental assumption of the adopted multi-scale theory is that at any instant t, the strain tensor at an arbitrary point $\boldsymbol{x}$ of the macro-continuum is assumed to be

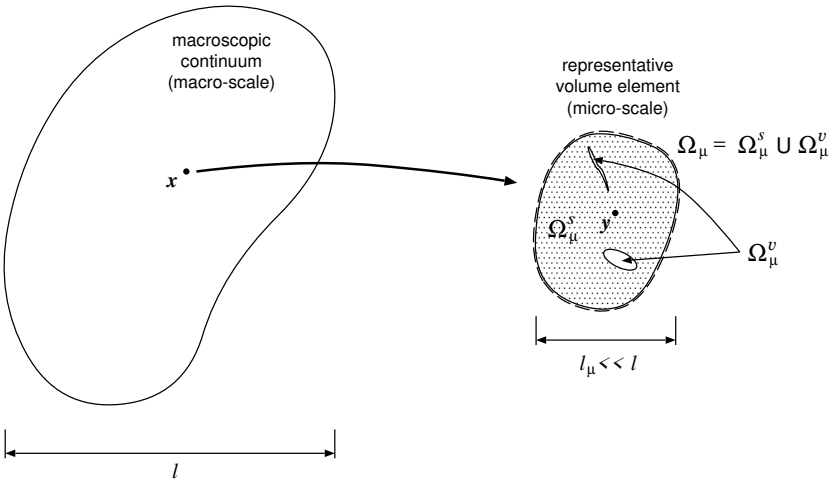

Figure A.1: Macro-continuum with a locally attached micro-structure.

the volume average of the microscopic strain tensor field, ε_μ, defined over Ω_μ :

$$\varepsilon(t) = \frac{1}{V_\mu} \int_{\Omega_\mu} \varepsilon_\mu(\boldsymbol{y}, t)\, \mathrm{d}V, \tag{A.2}$$

where V_μ is the volume of the RVE and

$$\varepsilon_\mu = \nabla^s \boldsymbol{u}_\mu\,, \tag{A.3}$$

where $\nabla^s \boldsymbol{u}_\mu$ denotes the symmetric gradient of the microscopic displacement field $\boldsymbol{u}_\mu$ of the RVE.

A.1.1 Kinematically Admissible RVE Displacement Fields

By introducing expression (A.3) into equation (A.2) and making use of Green's theorem, it can easily be shown that the averaging relation (A.2) is equivalent to the following constraint on the displacement field of the RVE [92]:

$$\int_{\partial\Omega_\mu} \boldsymbol{u}_\mu \otimes_s \boldsymbol{n}\, \mathrm{d}A = \int_{\partial\Omega_\mu} \frac{1}{2}(\boldsymbol{u}_\mu \otimes \boldsymbol{n} + \boldsymbol{n} \otimes \boldsymbol{u}_\mu)\, \mathrm{d}A = V_\mu\, \varepsilon\,, \tag{A.4}$$

where n denotes the outward unit normal field on $\partial\Omega_\mu$.

It has proved convenient to split the displacement $\boldsymbol{u}_\mu$ into a sum

$$\boldsymbol{u}_\mu(\boldsymbol{y}, t) = \varepsilon(t)\, \boldsymbol{y} + \tilde{\boldsymbol{u}}_\mu(\boldsymbol{y}, t)\,, \tag{A.5}$$

of a homogeneous strain displacement, $\boldsymbol{\varepsilon}(t)\,\boldsymbol{y}$, and a *displacement fluctuation* field, $\tilde{\boldsymbol{u}}_\mu$. The constraint (A.4) is then equivalent to requiring that the space $\tilde{\mathscr{K}}_\mu$ of kinematically admissible displacement fluctuations of the RVE be a subspace of the *minimally constrained space of kinematically admissible displacement fluctuations*, $\tilde{\mathscr{K}}_\mu^*$:

$$\tilde{\mathscr{K}}_\mu \subset \tilde{\mathscr{K}}_\mu^* \equiv \left\{ \boldsymbol{v},\ \text{sufficiently regular} \,|\, \int_{\partial\Omega_\mu} \boldsymbol{v} \otimes_s \boldsymbol{n}\, \mathrm{d}A = 0 \right\}. \tag{A.6}$$

Following the split (A.5) the microscopic strain (A.3) can be expressed as the sum

$$\boldsymbol{\varepsilon}_\mu(\boldsymbol{y}, t) = \boldsymbol{\varepsilon}(t) + \nabla^s \tilde{\boldsymbol{u}}_\mu(\boldsymbol{y}, t)\,, \tag{A.7}$$

of a homogeneous strain field (coinciding with the macroscopic, average strain) and a field $\nabla^s \tilde{\boldsymbol{u}}_\mu$ that represents a fluctuation about the average.

A.1.2 Macroscopic Stress, Hill-Mandel Principle and RVE Equilibrium

In similarity to the above macroscopic strain definition (A.3), the macroscopic stress tensor, $\boldsymbol{\sigma}$, is defined as the volume average of the microscopic stress field, $\boldsymbol{\sigma}_\mu$, over the RVE:

$$\boldsymbol{\sigma}(t) = \frac{1}{V_\mu} \int_{\Omega_\mu} \boldsymbol{\sigma}_\mu(\boldsymbol{y}, t)\, \mathrm{d}V\,. \tag{A.8}$$

An essential concept that underlies models of the present type is the Hill-Mandel Principle of Macro-homogeneity [127; 128] which requires the macroscopic stress power to equal the volume average of the microscopic stress power for any kinematically admissible motion of the RVE. This is expressed by the equation

$$\boldsymbol{\sigma} : \dot{\boldsymbol{\varepsilon}}(t) = \frac{1}{V_\mu} \int_{\Omega_\mu} \boldsymbol{\sigma}_\mu : \dot{\boldsymbol{\varepsilon}}_\mu\, \mathrm{d}V\,, \tag{A.9}$$

that must hold for any kinematically admissible microscopic strain rate field, $\dot{\boldsymbol{\varepsilon}}_\mu$. The above is equivalent to the following variational equation:

$$\int_{\partial\Omega_\mu} \boldsymbol{t} \cdot \boldsymbol{\eta}\, \mathrm{d}A = 0, \quad \int_{\Omega_\mu} \boldsymbol{b} \cdot \boldsymbol{\eta}\, \mathrm{d}V = 0 \quad \forall\, \boldsymbol{\eta} \in \tilde{\mathscr{K}}_\mu\,, \tag{A.10}$$

in terms of the RVE boundary traction and body force fields denoted, respectively, $\boldsymbol{t}$ and $\boldsymbol{b}$.

The variational equilibrium statement for the RVE is theh given by

$$\int_{\Omega_\mu} \boldsymbol{\sigma}_\mu : \nabla^s \boldsymbol{\eta} \, \mathrm{d}V = 0 \quad \forall \boldsymbol{\eta} \in \tilde{\mathscr{K}}_\mu \, . \tag{A.11}$$

Further, we assume that at any time t the stress at each point $\boldsymbol{y}$ of the RVE is delivered by a generic constitutive functional $\mathfrak{S}_{\boldsymbol{y}}$ of the strain history $\varepsilon_\mu^t(\boldsymbol{y})$ at that point up to time t:

$$\boldsymbol{\sigma}_\mu(\boldsymbol{y}, t) = \mathfrak{S}_{\boldsymbol{y}}(\varepsilon_\mu^t(\boldsymbol{y})). \tag{A.12}$$

This constitutive assumption, together with the equilibrium equation (A.11) leads to the definition of the RVE equilibrium problem which consists in finding, for a given macroscopic strain $\boldsymbol{\varepsilon}$ (a function of time), a displacement fluctuation function $\tilde{\boldsymbol{u}}_\mu \in \tilde{\mathscr{K}}_\mu$ such that

$$\int_{\Omega_\mu^s} \mathfrak{S}_{\boldsymbol{y}} \left\{ \left[\boldsymbol{\varepsilon}(t) + \nabla^s \tilde{\boldsymbol{u}}_\mu(\boldsymbol{y}, t) \right]^t \right\} : \nabla^s \boldsymbol{\eta} \, \mathrm{d}V = 0 \quad \forall \boldsymbol{\eta} \in \tilde{\mathscr{K}}_\mu \, . \tag{A.13}$$

A.1.3 Characterization of the Multi-Scale Constitutive Model

The general multi-scale constitutive model in the present context is defined as follows. For a given macroscopic strain history, we must firstly solve the RVE equilibrium problem defined by (A.13). With the solution $\tilde{\boldsymbol{u}}_\mu$ at hand, the macroscopic stress tensor is determined according to the averaging relation (A.8), i.e., we have

$$\boldsymbol{\sigma}(t) = \mathfrak{S}(\boldsymbol{\varepsilon}^t) \equiv \frac{1}{V_\mu} \int_{\Omega_\mu} \mathfrak{S}_{\boldsymbol{y}} \left\{ \left[\boldsymbol{\varepsilon} + \nabla^s \tilde{\boldsymbol{u}}_\mu \right]^t \right\} \mathrm{d}V \, , \tag{A.14}$$

where $\mathfrak{S}$ denotes the resulting (homogenised) macroscopic constitutive functional.

A.1.4 The Choice of kinematical Constraints

The characterization of a multi-scale model of the present type is completed with the choice of a suitable space of kinematically admissible displacement fluctuations, $\tilde{\mathscr{K}}_\mu \subset \tilde{\mathscr{K}}_\mu^*$. In general, different choices lead to different macroscopic response functionals. The following choices are as:

(i) *Linear boundary displacements* (or zero boundary fluctuations) model:

$$\tilde{\mathscr{K}}_\mu = \tilde{\mathscr{K}}_{\text{lin}} \equiv \{\boldsymbol{v},\ \text{sufficiently regular} \,|\, \boldsymbol{v}(\boldsymbol{y}) = 0 \,\forall\, \boldsymbol{y} \in \partial\Omega_\mu\}. \tag{A.15}$$

The displacements of the boundary of the RVE for this class of models are fully prescribed as

$$\boldsymbol{u}_\mu(\boldsymbol{y}) = \boldsymbol{\varepsilon}\,\boldsymbol{y} \quad \forall \boldsymbol{y} \in \partial\Omega_\mu. \tag{A.16}$$

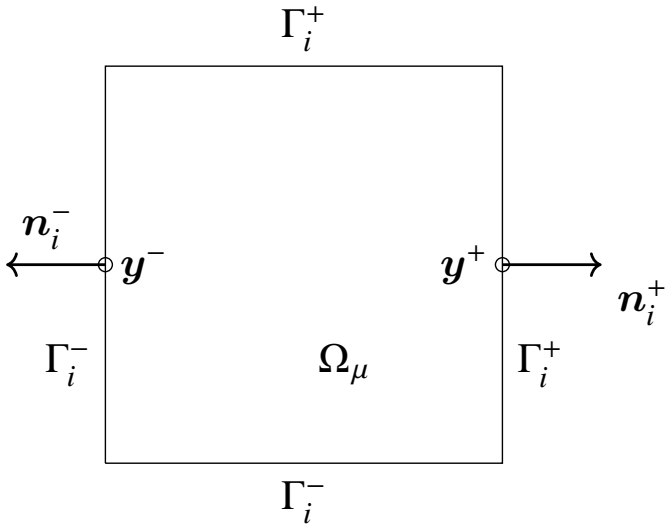

Figure A.2: Square RVE geometries for periodic media.

(ii) *Periodic boundary fluctuations*. This assumption is typically associated with the description of media with periodic microstructure. The macrostructure in this case is generated by the periodic repetition of the RVE [37]. For simplicity, we will focus the description on two-dimensional problems and we shall follow the notation adopted by [37]. Consider, for example, the square RVEs, as illustrated in Figure A.2. In this case, each pair i of sides consists of equally sized subsets

$$\Gamma_i^+ \quad \text{and} \quad \Gamma_i^- \tag{A.17}$$

of $\partial\Omega_\mu$, with respective unit normals

$$\boldsymbol{n}_i^+ \quad \text{and} \quad \boldsymbol{n}_i^- , \tag{A.18}$$

such that

$$\boldsymbol{n}_i^- \;=\; -\boldsymbol{n}_i^+ . \tag{A.19}$$

A one-to-one correspondence exists between the points of Γ_i^+ and Γ_i^-. That is, each point $\boldsymbol{y}^+ \in \Gamma_i^+$ has a corresponding pair $\boldsymbol{y}^- \in \Gamma_i^-$. The key kinematical constraint for this class of models is that the displacement fluctuation must be periodic on the boundary of the RVE. That is, for each pair $\{\boldsymbol{y}^+, \boldsymbol{y}^-\}$ of boundary material points we have

$$\tilde{\boldsymbol{u}}_\mu(\boldsymbol{y}^+, t) = \tilde{\boldsymbol{u}}_\mu(\boldsymbol{y}^-, t). \tag{A.20}$$

Accordingly, the space $\tilde{\mathscr{K}}_\mu$ is defined as

$$\tilde{\mathscr{K}}_\mu = \tilde{\mathscr{K}}_{\text{per}} \equiv \left\{ \tilde{\boldsymbol{u}}_\mu, \text{suff.reg.} \mid \tilde{\boldsymbol{u}}_\mu(\boldsymbol{y}^+, t) = \tilde{\boldsymbol{u}}_\mu(\boldsymbol{y}^-, t) \,\forall\, \text{pairs}\{\boldsymbol{y}^+, \boldsymbol{y}^-\}. \right\} \tag{A.21}$$

(iii) *The minimally constrained* (or uniform boundary traction) model:

$$\tilde{\mathscr{K}}_\mu \equiv \tilde{\mathscr{K}}_\mu^* . \tag{A.22}$$

It can be shown [92] that the distribution of stress vector on the RVE boundary, associated with the minimal kinematic constraint, satisfies

$$\boldsymbol{\sigma}_\mu(\boldsymbol{y}, t)\, \boldsymbol{n}(\boldsymbol{y}) \;=\; \boldsymbol{\sigma}(t)\, \boldsymbol{n}(\boldsymbol{y}) \quad \forall \boldsymbol{y} \in \partial\Omega_\mu . \tag{A.23}$$

Similarly to the linear boundary displacements assumption, there are no restrictions on the geometry of the RVE for this choice of the RVE constraint.

A.2 Finite Element Approximation

This section provides a brief description of the computational implementation of multi-scale constitutive methodology described in section A.1 within a non-linear finite element framework. At the outset, it is assumed that the constitutive behaviour at the RVE level is described by conventional internal variable-based dissipative constitutive laws, such as classical models of elasto-plasticity and elasto-viscoplasticity. Numerical approximations to the initial value problem defined by the constitutive equations of the model are usually obtained by Euler-type difference schemes. For a typical time (or pseudo-time) interval $[t^n, t^{n+1}]$, and given set of $\boldsymbol{\alpha}^n$ of internal variables at t^n , the stress $\boldsymbol{\sigma}_\mu^{n+1}$ at t^{n+1} is a function of the prescribed strain $\boldsymbol{\varepsilon}_\mu^{n+1}$ at t^{n+1} (see, for instance, to [54] for a detailed account of procedures of this kind in the context of plasticity and visco-plasticity). The stress update procedure can be symbolically represented as

$$\boldsymbol{\sigma}_\mu^{n+1} = \hat{\boldsymbol{\sigma}}_{\boldsymbol{y}}(\boldsymbol{\varepsilon}_\mu^{n+1}; \boldsymbol{\alpha}^n)\,, \tag{A.24}$$

where $\hat{\boldsymbol{\sigma}}_{\boldsymbol{y}}$ denotes the integration algorithm-related implicit incremental constitutive function at the point of interest, $\boldsymbol{y}$.

The homogenised constitutive function defined in (A.14), can now be expressed in its incremental form as:

$$\boldsymbol{\sigma}^{n+1} = \hat{\boldsymbol{\sigma}}(\boldsymbol{\varepsilon}^{n+1}; \bar{\boldsymbol{\alpha}}^n) \equiv \frac{1}{V_\mu}\int_{\Omega_\mu} \hat{\boldsymbol{\sigma}}_{\boldsymbol{y}}(\boldsymbol{\varepsilon}^{n+1} + \nabla^s \tilde{\boldsymbol{u}}_\mu^{n+1}; \boldsymbol{\alpha}^n)\,\mathrm{d}V\,, \tag{A.25}$$

where $\bar{\boldsymbol{\alpha}}^n$ denotes the field of internal variable sets over Ω_μ at time t_n and $\tilde{\boldsymbol{u}}_\mu^{n+1}$ is the displacement fluctuation field of the RVE at t^{n+1}, which is obtained as the solution of the time-discrete version of equilibrium problem (A.13):

$$\int_{\Omega_\mu^s} \hat{\boldsymbol{\sigma}}_{\boldsymbol{y}}(\boldsymbol{\varepsilon}^{n+1} + \nabla^s \tilde{\boldsymbol{u}}_\mu^{n+1}; \boldsymbol{\alpha}^n) : \nabla^s \boldsymbol{\eta}\,\mathrm{d}V \;=\; 0 \quad \forall \boldsymbol{\eta} \in \tilde{\mathscr{K}}_\mu\,. \tag{A.26}$$

A.2.1 Finite Element Discretization and Solution

Following a standard procedure, the finite element approximation to problem (A.26) for a given discretisation h consists in determining the unknown vector $\tilde{\boldsymbol{u}}_\mu^{n+1} \in \tilde{\mathscr{K}}_\mu^h$

of global nodal displacement fluctuations such that

$$G^h(\tilde{\boldsymbol{u}}_\mu^{n+1}) \equiv \left\{ \int_{\Omega_\mu^h} \mathbf{B}^T \hat{\boldsymbol{\sigma}}_{\boldsymbol{y}}(\boldsymbol{\varepsilon}^{n+1} + \mathbf{B}\,\tilde{\boldsymbol{u}}_\mu^{n+1})\,\mathrm{d}V \right\} \cdot \boldsymbol{\eta} \;=\; 0 \quad \forall \boldsymbol{\eta} \in \tilde{\mathscr{K}}_\mu^h\,, \tag{A.27}$$

where Ω_μ^h denotes the discretised RVE domain, $\mathbf{B}$ the global strain-displacement matrix (or discrete symmetric gradient operator), $\boldsymbol{\varepsilon}^{n+1}$ is the fixed (given) array of macroscopic engineering strains at t^{n+1} , $\hat{\boldsymbol{\sigma}}_{\boldsymbol{y}}$ is the functional that delivers the finite element array of stress components, $\boldsymbol{\eta}$ denotes global vectors of nodal virtual displacements of the RVE and $\tilde{\mathscr{K}}_\mu^h$ is the finite-dimensional space of virtual nodal displacement vectors associated with the finite element discretisation h of the domain Ω_μ.

The solution to the non-linear problem (A.27) is commonly undertaken by the Newton-Raphson iterative scheme, whose typical iteration $(k+1)$ consists in solving the linearised form,

$$\left[\mathbf{F}^{(k)} + \mathbf{K}^{(k)}\,\delta\tilde{\boldsymbol{u}}_\mu^{(k+1)} \right] \cdot \boldsymbol{\eta} \;=\; 0 \quad \forall \boldsymbol{\eta} \in \tilde{\mathscr{K}}_\mu^h\,, \tag{A.28}$$

for the unknown iterative nodal displacement fluctuations vector, $\delta\tilde{\boldsymbol{u}}_\mu^{(k)} \in \tilde{\mathscr{K}}_\mu^h$ where

$$\mathbf{F}^{(k)} \equiv \int_{\Omega_\mu^h} \mathbf{B}^T \hat{\boldsymbol{\sigma}}_{\boldsymbol{y}}(\boldsymbol{\varepsilon}^{n+1} + \mathbf{B}\,\tilde{\boldsymbol{u}}_\mu^{k})\,\mathrm{d}V\,, \tag{A.29}$$

and

$$\mathbf{K}^{(k)} \equiv \int_{\Omega_\mu^h} \mathbf{B}^T \mathbf{D}^{(k)} \mathbf{B}\,\mathrm{d}V \tag{A.30}$$

is the tangent stiffness matrix of the RVE with

$$\mathbf{D}^{(k)} \equiv \left. \frac{\mathrm{d}\hat{\boldsymbol{\sigma}}_{\boldsymbol{y}}}{\mathrm{d}\boldsymbol{\varepsilon}} \right|_{\boldsymbol{\varepsilon}=\boldsymbol{\varepsilon}^{n+1}+\mathbf{B}\tilde{\boldsymbol{u}}_\mu^{n+1}} \tag{A.31}$$

denoting the consistent constitutive tangent matrix field over the RVE domain. In the above the bracketed superscript denotes the Newton iteration number. With the solution $\delta\tilde{\boldsymbol{u}}_\mu^{(k)}$ at hand, the new guess $\tilde{\boldsymbol{u}}_\mu^{(k)}$ for the displacement fluctuation at t_{n+1} is obtained according to the Newton-Raphson update formula

$$\tilde{\boldsymbol{u}}_\mu^{(k+1)} = \tilde{\boldsymbol{u}}_\mu^{(k)} + \delta\tilde{\boldsymbol{u}}_\mu^{(k+1)}\,. \tag{A.32}$$

It should be noted that under the assumption of linear boundary displacements, the solution of problem (A.28) follows the conventional route of general linear solid mechanics problems, with the fluctuations degrees of freedom of the boundary fully prescribed as zero. For the periodic and uniform tractions boundary condition models, however, the kinematic boundary conditions of the RVE are non-conventional. For details of implementation of different boundary conditions within the described variational framework under both small and large strain conditions we refer to our earlier publications [91] and [126], respectively.

A.3 Derivation of Some Expressions Referred in the Thesis

A.3.1 Derivation for Shear Function

$$\begin{aligned}\frac{\partial^2 \Psi_{\text{shr}}}{\partial p^2} &= \frac{\partial (b\Psi_{\text{shr}})}{\partial p} = \left[\frac{\partial b}{\partial p}\Psi_{\text{shr}} + b\frac{\partial \Psi_{\text{shr}}}{\partial p}\right] \\ &= -\left[\frac{1}{(p-p_t)^2} + \frac{1}{m(p-p_c)^2}\Psi_{\text{shr}} + b\frac{\partial \Psi_{\text{shr}}}{\partial p}\right]\end{aligned} \tag{A.33}$$

$$\frac{\partial}{\partial(\Delta\varepsilon_{\text{v}}^{p})}\left(\frac{\partial \Psi_{\text{shr}}}{\partial p}\right) = \frac{1}{n}\left[\begin{array}{c} -\frac{H_t}{p-p_c} - \frac{H_c(p-p_t)}{(p-p_c)^2} \\ -\left[1 + \frac{(p-p_t)}{m(p-p_c)}\right]\left[\frac{H_c}{p-p_c} + \frac{(H_t-H_c)}{(p_t-p_c))}\right] \end{array}\right] * \tan\psi \left[\frac{p-p_c}{p_t-p_c}\right]^{\frac{1}{n}} \tag{A.34}$$

$$\frac{\partial \Phi_{\text{shr}}}{\partial(\Delta\varepsilon_{\text{v}}^{p})} = -H_t \tan\beta\left[\frac{p-p_c}{p_t-p_c}\right]^{\frac{1}{n}}$$

$$+\frac{1}{n}(p-p_t)\tan\beta\left(\frac{p-p_c}{p_t-p_c}\right)^{\frac{1}{n}}\left(\frac{p-p_c}{p_t-p_c}\right)\left(-\frac{H_c}{(p_t-p_c)}-\frac{(p-p_c)(H_t-H_c)}{(p_t-p_c)^2}\right.$$

$$=-H_t\tan\beta\left(\frac{p-p_c}{p_t-p_c}\right)^{\frac{1}{n}}-\frac{1}{n}(p-p_t)\tan\beta\left(\frac{p-p_c}{p_t-p_c}\right)\Bigg)^{\frac{1}{n}}\left(\frac{H_c}{p-p_c}+\frac{(H_t-H_c)}{(p_t-p_c)}\right)$$

$$=-\left[H_t+\frac{1}{n}(p-p_t)\left(\frac{H_c}{p-p_c}+\frac{(H_t-H_c)}{(p_t-p_c)}\right)\right]\tan\beta\left(\frac{p-p_c}{p_t-p_c}\right)^{\frac{1}{n}} \tag{A.35}$$

$$\frac{\partial \Phi_{\text{shr}}}{\partial(\Delta\gamma)} = -3Gg^2 \tag{A.36}$$

$$\frac{\partial^2 \Phi_{\text{shr}}}{\partial q^2} = 0 \tag{A.37}$$

A.3.2 Derivation for Cap Function

$$\frac{\partial \Psi_{\text{cap}}}{\partial p} = -2M_{\Psi}^2 p_{\psi\text{crit}}^2 \frac{(p_{\psi\text{crit}}-p)}{(p_{\psi\text{crit}}-p_c)^2} \tag{A.38}$$

$$\frac{\partial \Psi_{\text{cap}}}{\partial q} = -2g^2 q \tag{A.39}$$

$$\frac{\partial \Phi_{\text{cap}}}{\partial p} = -2M_{\Phi}^2 p_{\phi\text{crit}}^2 \frac{(p_{\phi\text{crit}}-p)}{(p_{\phi\text{crit}}-p_c)^2} \tag{A.40}$$

$$\frac{\partial^2 \Psi_{\text{cap}}}{\partial p^2} = \frac{2M_{\Psi}^2 p_{\Psi\text{crit}}^2}{(p_{\Psi\text{crit}}-p_c)^2} \tag{A.41}$$

$$\frac{\partial}{\partial(\Delta\varepsilon_{\mathrm{v}}^{p})}\left(\frac{\partial\Psi_{\mathrm{cap}}}{\partial p}\right) = \left[-4M_{\Psi}^{2}p_{\Psi\mathrm{crit}}\frac{(p_{\Psi\mathrm{crit}}-p)}{(p_{\Psi\mathrm{crit}}-p_{c})^{2}} - 2M_{\Psi}^{2}p_{\Psi\mathrm{crit}}^{2}\frac{1}{(p_{\Psi\mathrm{crit}}-p_{c})^{2}}\right]H_{\Psi\mathrm{crit}}$$

$$+ 4M_{\Psi}^{2}p_{\Psi\mathrm{crit}}\frac{(p_{\Psi\mathrm{crit}}-p)}{(p_{\Psi\mathrm{crit}}-p_{c})^{3}}\left(H_{\Psi\mathrm{crit}}-H_{c}\right)$$

$$= -2M_{\Psi}^{2}p_{\Psi\mathrm{crit}}^{2}\frac{(p_{\Psi\mathrm{crit}}-p)}{(p_{\Psi\mathrm{crit}}-p_{c})^{2}}\left[\frac{2}{p_{\Psi\mathrm{crit}}}+\frac{1}{(p_{\Psi\mathrm{crit}}-p)}\right]H_{\Psi\mathrm{crit}}$$

$$= -\frac{2}{(p_{\Psi\mathrm{crit}}-p_{c})}\frac{\partial\Psi_{\mathrm{cap}}}{\partial p}\left(H_{\Psi\mathrm{crit}}-H_{c}\right)$$

$$= \left[\frac{2}{p_{\Psi\mathrm{crit}}}+\frac{1}{(p_{\Psi\mathrm{crit}}-p)}\right]\frac{\partial\Psi_{\mathrm{cap}}}{\partial p}H_{\Psi\mathrm{crit}} - \frac{2}{(p_{\Psi\mathrm{crit}}-p_{c})}\frac{\partial\Psi_{\mathrm{cap}}}{\partial p}\left(H_{\Psi\mathrm{crit}}-H_{c}\right) \tag{A.42}$$

$$\frac{\partial\Phi_{\mathrm{cap}}}{\partial(\Delta\varepsilon_{\mathrm{v}}^{p})} = -2M_{\Phi}^{2}p_{\Phi\mathrm{crit}}H_{\Phi\mathrm{crit}}\left[1-\frac{(p_{\Phi\mathrm{crit}}-p)^{2}}{(p_{\Phi\mathrm{crit}}-p_{c})^{2}}\right]$$

$$- M_{\Phi}^{2}p_{\Phi\mathrm{crit}}^{2}\left[\frac{2(p_{\Phi\mathrm{crit}}-p)}{(p_{\Phi\mathrm{crit}}-p_{c})^{2}}H_{\Phi\mathrm{crit}}+\frac{2(p_{\Phi\mathrm{crit}}-p)^{2}}{(p_{\Phi\mathrm{crit}}-p_{c})^{3}}(H_{\Phi\mathrm{crit}}-H_{c})\right]$$

$$= -\frac{2}{p_{\Phi\mathrm{crit}}}H_{\Phi\mathrm{crit}}\Phi_{\mathrm{cap}}^{p}$$

$$= +2M_{\Phi}^{2}p_{\Phi\mathrm{crit}}^{2}\frac{(p_{\Phi\mathrm{crit}}-p)}{(p_{\Phi\mathrm{crit}}-p_{c})^{2}}\left[H_{\Phi\mathrm{crit}}-\frac{(p_{\Phi\mathrm{crit}}-p)}{(p_{\Phi\mathrm{crit}}-p_{c})}(H_{\Phi\mathrm{crit}}-H_{c})\right]$$

$$= -\frac{2}{p_{\Phi\mathrm{crit}}}H_{\Phi\mathrm{crit}}\Phi_{\mathrm{cap}}^{p} - \frac{\partial\Phi_{\mathrm{cap}}}{\partial p}\left[H_{\Phi\mathrm{crit}}-\frac{(p_{\Phi\mathrm{crit}}-p)}{(p_{\Phi\mathrm{crit}}-p_{c})}(H_{\Phi\mathrm{crit}}-H_{c})\right] \tag{A.43}$$

$$\frac{\partial\Phi_{\mathrm{cap}}}{\partial(\Delta\gamma)} = 0 \tag{A.44}$$

$$\frac{\partial^2 \Phi_{\text{cap}}}{\partial q^2} = 2g^2 \tag{A.45}$$